REVIEW ARTICLE

Check for updates

Ampere-level electroreduction of CO$_2$ and CO†

Qian Sun, [a] Chen Jia, [a] Haochen Lu, [a] Mengmeng Yang, [a] Ruirui Liu, [a] Dan M. Villamanca, [b] Yong Zhao *[b] and Chuan Zhao *[a]

Electroreduction of carbon dioxide (CO$_2$RR) and carbon monoxide (CORR) is promising to reduce the global carbon footprint and obtain high-value products. However, both reactions are limited by the intrinsically low activity of catalysts and mass transport of reactants at the catalyst/electrolyte interface. Recent progress has highlighted the need of rational catalyst design and mass transport engineering for improving the reaction kinetics and operating the CO$_2$RR/CORR at current densities at ampere levels (>500 mA cm^{-2}). This review introduces recent advances in the CO$_2$RR/CORR at ampere-level current densities, especially the catalytic mechanisms and the principles for catalyst design and mass transport manipulation. The strategies for catalyst design including alloying and doping, single atom effects, regulating the morphology and structure, oxidation state control, and organic molecule functionalization are reviewed together with the mass transfer manipulation through electrode engineering and electrolyzer optimization. The challenges and perspectives are discussed for further industrial development in this field.

1. Introduction

The carbon dioxide electroreduction reaction (CO$_2$RR), powered by renewable electricity, is an attractive strategy to convert CO$_2$ into valuable chemicals and fuels, thus mitigating global warming and relieving the strong dependence on traditional fossil fuels.[1–9] Multicarbon C$_{2+}$ products (*e.g.* ethylene, ethanol, acetic acid, and *n*-propanol), compared to C$_1$ products (*e.g.* CO, formate, methane, and methanol), exhibit higher energy densities and economic value and are important feedstock for developing long-chain hydrocarbon fuels.[10] Over the past decade, numerous efforts have been devoted to improving the selectivity of multi-carbon products by using highly alkaline electrolytes to suppress the hydrogen evolution and boost the yield of the target products.[11,12] However, the alkaline CO$_2$RR

^{a} *School of Chemistry, The University of New South Wales, Sydney, NSW 2052, Australia. E-mail: chuan.zhao@unsw.edu.au*

^{b} *Global Innovative Centre for Advanced Nanomaterials, School of Engineering, The University of Newcastle, Callaghan, NSW 2308, Australia. E-mail: yong.zhao@newcastle.edu.au*

† Electronic supplementary information (ESI) available. See DOI: https://doi.org/10.1039/d4cs00863d

Qian Sun obtained her PhD degree in Chemistry from the University of New South Wales (UNSW) in 2023, under the supervision of Prof. Chuan Zhao. She then did postdoctoral research in Prof. Chuan Zhao's group, focusing on single atom catalysts for electroreduction of CO$_2$ and CO (2023–2024). After that, she joined Prof. David Sinton's group as a postdoctoral fellow at the University of Toronto in Canada. Her current research is production of multi-carbon species from CO$_2$ and CO electroreduction.

Qian Sun

Chen Jia received his PhD degree in Chemistry from the University of New South Wales (UNSW), Sydney, in 2021. He is currently a postdoctoral research fellow at UNSW, working under the supervision of Prof. Chuan Zhao. His research focuses on the design and synthesis of nanomaterials and single-atom catalysts for energy conversion.

Chen Jia

This journal is © The Royal Society of Chemistry 2025

Chem. Soc. Rev., 2025, **54**, 6973–7016 | 6973

suffers from the carbonate formation issue, which results in depletion of CO_2 and OH^-, catalytic performance degradation,[13,14] and high energy penalty for CO_2 recovery from the generated carbonates.[14] An alternative route for CO_2-to-C_{2+} conversion is to reduce CO_2 initially to CO and subsequently to C_{2+}. As a carbonate-formation-free approach, the CO electroreduction reaction (CORR) operates stably in high-alkalinity electrolytes that favors C–C coupling kinetics.[14] Moreover, the CO_2RR and CORR share common reduction pathways.[15] Exploring the CORR is also beneficial for further understanding of the mechanism of the CO_2RR.

Despite recent advances in CO_2/CO upgrading to valuable fuels and feedstock, the reaction productivity is typically restricted by the poor activity of catalysts and mass transport issues. Most related studies are conducted in the lab-scale H-cells, which deliver low current densities (<50 mA cm^{-2}) due to the low gas solubilities in aqueous electrolytes (CO_2: ~ 34 mM in H_2O; CO: ~ 1 mM in H_2O),[2,16–18] whereas industrial electrolyzers typically require current densities >200 mA cm^{-2}.[19] For practical applications, CO_2/CO electrolysis must perform at ampere-level current densities (>0.5 A cm^{-2}) with high energy efficiency to minimize operating and capital costs.[20–26] This requires active catalysts for efficient CO_2/CO reduction and electrode/electrolyzer engineering for improved mass transfer of the reactants, intermediates (e.g. *CO, *COH, *CHOH, and *CHO), and electrons.

Many effective methods have been devoted to optimizing catalysts, such as developing single atom catalysts,[27] element doping,[25] alloying,[28] molecule functionalization,[12] hydrophobicity manipulation,[29] etc. Mass transport is another critical factor. Normally, the application of gas diffusion electrodes (GDEs), consisting of gas diffusion layers (GDLs), microporous layers (MPLs) and catalyst layers, affords maximization of CO_2/CO solubility and sufficient mass transport directly to the catalyst surface and further reduction at the gas–solid–liquid triple-phase boundaries.[30] Optimization of GDEs should consider the key factors of high porosity, low electrical resistance, catalyst accessibility, chemical and mechanical stability, and scalability.[31,32] Approaches proposed to facilitate mass transfer for the CO_2RR/CORR include porous micro-structured GDE construction, wettability control, polymer engineering, quasi-two-phase interface modification, optimization of flow cells and MEA (gas channels, membranes), cell-stack deployment, etc.[33–35]

Haochen Lu

Haochen Lu received his BSc and MSc degrees from Nanjing University of Science and Technology in 2017 and 2020. He is currently a PhD candidate in Prof. Chuan Zhao's group at the University of New South Wales in Sydney. His research interests focus on the electrocatalytic reduction of CO_2.

Mengmeng Yang

Mengmeng Yang received her BSc degree from Qiqihar University in 2018 and her MSc degree from Beijing University of Chemical Technology in 2021. She is currently a PhD candidate in Prof. Chuan Zhao's group at the University of New South Wales. Her research interests focus on electrocatalytic CO_2 reduction.

Yong Zhao

Yong Zhao is a Lecturer and DECRA Fellow in the School of Engineering at the University of Newcastle, Australia. His research focuses on electrochemical conversion of small molecules (e.g., CO_2, O_2, N_2, and H_2), with an emphasis on energy-efficient catalysts and systems. He recieved his PhD in Chemistry from the University of Wollongong in 2019 and conducted postdoctoral research at the University of New South Wales, the University of Sydney, and the University of Toronto until 2022. Prior to joining the University, he was a Research Scientist at the CSIRO Energy Centre from 2023 to 2025.


Chuan Zhao

Chuan Zhao is a professor at the School of Chemistry at the University of New South Wales (UNSW), Sydney. He is currently the Deputy Director of the Australian Research Council (ARC) Training Centre for the Global Hydrogen Economy, and the Deputy Research Chair and Flagship Program Director of the ARC Centre of Excellence on Green Electrochemical Transformation of Carbon Dioxide. He is interested in discovering novel electrochemical methodologies and nanomaterials for energy applications, including water splitting, hydrogen fuel cells, CO_2 and N_2 reduction, batteries, and sensors.
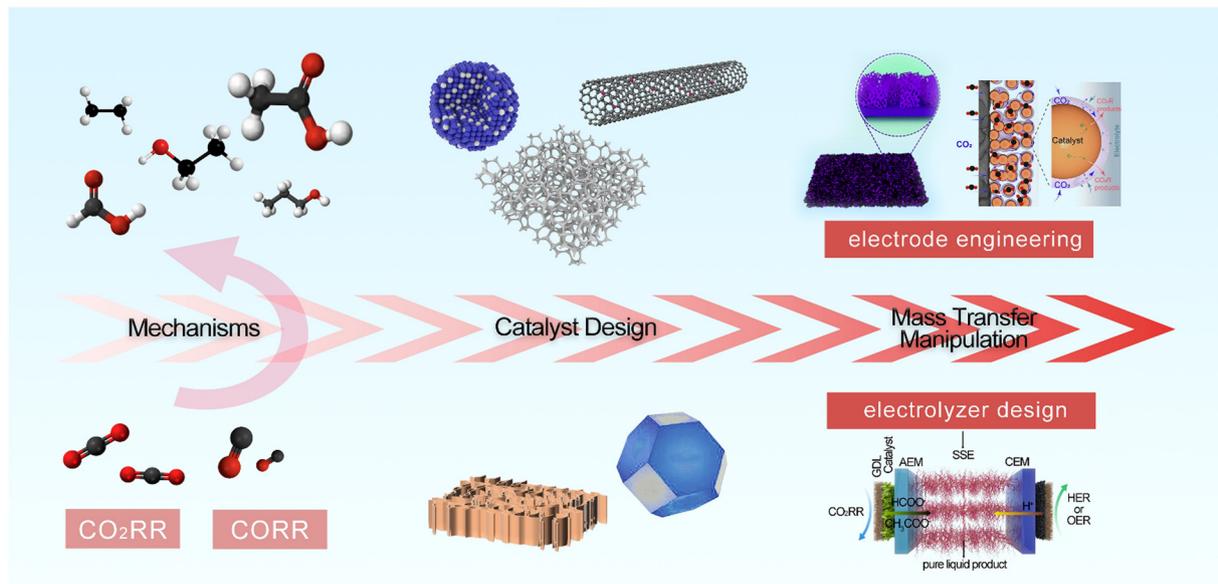
Scheme 1 Schematic diagram of the main content for CO_2RR/CORR at ampere-level current densities. Bi-ene-NW. Reproduced with permission.[45] Copyright 2021, Royal Society of Chemistry. The mode for managing the CO_2/H_2O balance at the CO_2RR reaction interface. Reproduced with permission.[46] Copyright 2024, Springer Nature.

A significant challenge and an important topic of research in the field of CO_2RR/CORR is how to enhance the current densities for the CO_2RR/CORR to an ampere level for industrial applications.[36–41] There have been many reviews focusing on catalyst design, electrolyzer design, and mechanisms in traditional H-cells and flow-cell electrolyzers, respectively.[42–44] Nevertheless, few review articles to date have focused on a holistic consideration for boht catalysts and mass transport for realizing the CO_2RR/CORR with ampere-level productivity. A review paper is therefore timely and will offer straightforward understanding and insights into the ampere-level CO_2RR/CORR.

This review focuses on CO_2/CO reduction with high selectivity in the ampere-level current density regime. First, we provide a brief overview of the CO_2RR/CORR, followed by introduction of the reaction mechanism and the status of ampere-level CO_2/CO electrolysis in terms of productivity and selectivity. Next, the key principles of designing catalysts and controlling mass transport to promote CO_2/CO reduction at ultrahigh reaction rates are summarized. Finally, we highlight the challenges for the ampere-level CO_2RR/CORR and offer our views on some important and promising research directions to address these challenges (Scheme 1).

2. CO_2RR/CORR mechanism

2.1. CO_2RR mechanism

CO_2 can be converted into various products through different multi-electron/proton transfer pathways. Fig. 1a summarizes the faradaic efficiency (FE) of the reported CO_2RR products at different production rates (current density), representing the selectivity of the reaction at ampere-level current. Notably, the state-of-the-art catalysts can facilitate C_1 products (e.g., CO and

formate) formation with >95% FE at high current density over 1 A cm^{-2},[20,47,48] while the specific C_{2+} products (e.g., C_2H_4 and C_2H_5OH) have not achieved such a high FE (>80%) so far,[49,50] although the FE of total C_{2+} products has reached over 80%.[51] This originates from the adsorption of several CO_2 molecules, stepwise conversion, and spatial positioning for C–C coupling.[52] Propelling deep research on the CO_2RR mechanisms favors designing more efficient catalysts and achieving more significant breakthroughs.

Thermodynamically, CO_2 molecules are difficult to activate due to the high dissociation energy of the C=O bond (750 kJ mol^{-1}).[53] Kinetically, the CO_2RR proceeds on practical electrodes for various products, powered by an overpotential relative to the standard potentials. According to the number of electrons transferred, CO_2 can be converted to CO/formate, methanol, methane, and ethylene/ethanol via 2, 6, 8, and 12 electron transfer, respectively. As for the generation of the most common product CO, the reduction pathway involves either three or four kinetic steps. Normally, the first step of CO_2 adsorption to form COOH* occurs via a proton-coupled electron transfer (PCET),[54] or two uncoupled steps with CO_2 conversion to COO* and further to COOH*.[55] Then, the COOH* intermediate transforms into CO* and H_2O over a H^+/e^- transfer, followed by CO desorption. Different from the traditional PCET pathway, H adsorption strength can be modulated to enable tuning of hydrogen radical (H•) formation whilst simultaneously inhibiting the HER,[56] thereby enhancing the CO_2-to-CO reaction kinetics.

The formate formation is dependent on pH, which can take place at low pH (<3) or higher values (weak alkaline).[57] The intermediate (HCOO*) is formed as CO_2 molecules gain an electron, while formate is generated by combining a proton and another electron following three pathways. Pathway 1: a radical
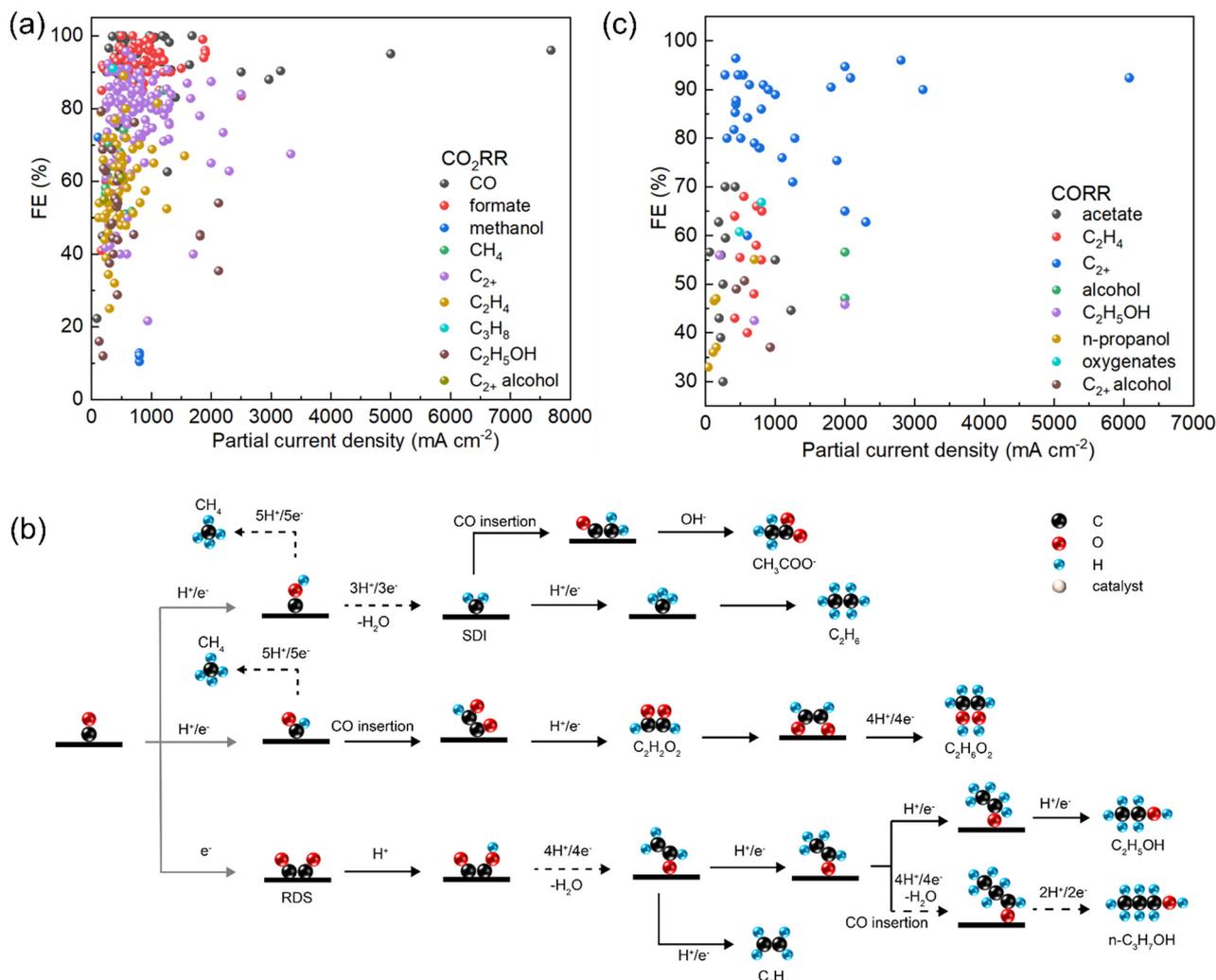
This journal is © The Royal Society of Chemistry 2025

Chem. Soc. Rev., 2025, **54**, 6973–7016 | **6975**

Fig. 1 CO$_2$RR/CORR mechanism. (a) Summary of the CO$_2$RR at ampere-level current (data from Table S1, ESI†). (b) Most possible C$_{2+}$ pathways during the CO$_2$RR. (c) Summary of the CORR at ampere-level current (data from Table S2, ESI†).

anion is formed by transferring a proton to CO$_2$, where the oxygens are connected to the electrode surface. Thus, the protonation takes place on the carbon atom to produce the intermediate (HCOO), and further conversion into formate *via* a second electron transfer. Pathway 2: the OCHO intermediate is formed after transferring an electron to HCOO, which further protonates to formic acid. Pathway 3: the carbon atom in the radical anion is bound to the electrode surface, while the oxygen atom undergoes protonation to produce a COOH intermediate, which further combines protons and electrons to formic acid. Among these three pathways, pathway 1 is more favorable in product selection, due to its lower energy and overpotential requirements. Furthermore, the OCHO intermediate generation is revealed as the rate-determining step (RDS) for CO$_2$ reduction,[58] which further protonates to formate.

Carbene species (*CH$_2$) derived from *CO is considered as the common intermediate for CH$_4$ and C$_2$H$_4$ formation.[59] *CH$_2$ transforms into CH$_4$ through double proton–electron transfer, while C$_2$H$_4$ is produced *via* the *CH$_2$ dimerization or CO

insertion in a Fischer–Tropsch-like step, which is also the pathway towards alcohols. Differently, the second C–O bond is broken at a late stage in the thermodynamically most favorable pathway to CH$_4$.[60] The methoxy intermediate (*HCO, *H$_2$CO, and *H$_3$CO) derived from *CO hydrogenation is converted to CH$_4$ and *O and finally to H$_2$O. C$_2$H$_4$ is produced by the H$_x$CO species dimerization and subsequent deoxygenation. The binding ability to OH species is considered the determining factor for methanol production over methane.[61] Specially, methanol is preferred on the catalysts with weakly bound OH which facilitates removing –OCH$_3$ from the surface (*OCH$_3$ + H$^+$ + e$^-$ → * + CH$_3$OH), while the ones with strong OH binding promote methane formation after breaking the *O–CH$_3$ bond (*OCH$_3$ + H$^+$ + e$^-$ → *O + CH$_4$).

As for the C$_{2+}$ production, the *CH$_2$ intermediate derived from *CO *via* PCET is for generating C$_2$H$_6$ and CH$_3$COO$^-$ (Fig. 1b), which is further protonated to *CH$_3$ and finally dimmerized to C$_2$H$_6$, whereas CH$_3$COO$^-$ is produced by CO insertion into *CH$_2$. Noteworthily, the RDS for C$_2$H$_4$, CH$_3$CH$_2$OH, and *n*-propanol

6976 | *Chem. Soc. Rev.*, 2025, **54**, 6973–7016

This journal is © The Royal Society of Chemistry 2025

production is the *CO dimerization step. The *CH$_2$CHO intermediate derived from the *CO–CO dimer determines the selectivity of C$_2$H$_4$ and C$_2$H$_5$OH. Besides, n-propanol is formed by CO insertion into the stabilized C$_2$ intermediates.[62]

Apart from the above intermediates, proton transfer also plays a crucial role in the CO$_2$ electrolysis process.[3] Typically, hydrogen transfer proceeds via the Eley–Rideal mechanism with proton-coupled electron transfer directly from solvent water,[63] while hydrogenation can also happen via the Langmuir–Hinshelwood mechanism using surface-adsorbed *H. These two mechanisms are responsible for C–H bond and O–H bond formation, respectively, with the former one being critical to C$_2+$ production and H$_2$ suppression and the latter one being the dominant hydrogenation route. H$^+$ reduction is negligible in neutral and alkaline electrolytes, while H$_2$O reduction is pH independent. H$^+$ serves as an additional proton source for the hydrogen evolution reaction (HER) in acid, whose reduction rate can be decided by the local pH near the cathode. Suppression of H$^+$ mass transfer benefits constructing a local high-pH environment around the catalyst and restricting the H$^+$ reduction rate. To facilitate the CO$_2$RR in acid, mass transfer and electrode reactions can be modulated by various strategies, such as introducing alkali cations in electrolytes to inhibit H$^+$ migration, suppressing H$^+$ diffusion by catalyst surface decoration, regulating the electronic structure of catalysts, and controlling the interfacial H$^+$ microenvironment via adding sulfonate-based electrolyte additives.[64]

2.2. CORR mechanism

Recently, the CORR has attracted much interest for the green synthesis of C$_2+$ species, due to its stable operation in alkaline electrolytes, circumvention of carbonate formation, and higher reaction rates than those of the CO$_2$RR.[14,40,65,66] Fig. 1c displays the FE of the reported CORR products at ampere-level current density. Obviously, most FE$_{C_2+}$ values approach 80–90%,[41,65] but the specific C$_2+$ product (acetate, C$_2$H$_4$) exhibits a FE less than 70%,[28,40] while n-propanol exhibits only <37%.[67] The CORR shares the common reduction pathways to the CO$_2$RR after CO$_2$ is converted to the absorbed *CO. The CO-to-methanol conversion is promoted by Rh$_1$Cu$_4$ alloy with homogeneous distribution of isolated Rh sites inside the Cu framework.[68] The isolated Rh active sites enriched *H coverage on the catalyst and favored *CH$_2$OH hydrogenation, resulting in efficient methanol production.[69] The lowest energy pathway for CO-to-C$_2$H$_5$OH reveals that CO is firstly reduced at 0 and −0.40 V vs. RHE, followed by the intermediate protonation via proton and electron transfer and finally the product desorption. During which, the dehydration of OH groups makes them more active than the oxygen atoms in the carbonyl group. Sharing the same pathway as C$_2$H$_5$OH, the CO reduction to C$_2$H$_4$ is formed at the sixth H$^+$/e$^-$ transfer step, which is inclined from C$_2$H$_5$OH by approximately 0.2 eV.

The pH effects on the CORR reduction pathways were studied theoretically.[70] CHO and COH are produced from the protonation of absorbed CO at acidic pH, which transforms into C$_1$ species by removing OH or the CHOH path, whereas the oxygen atoms in carbonyl are hydrogenated to C$_1$ products via CHO. In comparison, C$_2+$ species are favored at neutral and high pH. The C–C coupling is facilitated at neutral pH through a novel CO–COH pathway, while the dimerization of adsorbed CO is dominantly responsible for generating C$_2$/C$_3$ products at high pH. Thus, modulating pH and applied potential play crucial roles in boosting C$_2+$ selectivity. Protons in electrolytes also present critical effects on the surface adsorbed *H species and the production of C$_2+$ species such as ethanol. However, the selectivity of C$_2+$ oxygenates is challenged by the hindered coupling of *H and carbon-containing intermediates due to their inappropriate distributions in catalytic interfaces. Therefore, efficient water dissociation and proper *H distribution benefit the coupling with the carbon-containing species to generate C$_2+$ oxygenates.[71]

The adsorbed CO initially dimerizes at neutral pH and then transforms into *(OH)C=COH, followed by protonation to *C=COH,[72,73] which is further reduced to ethylene and alcohol via parallel pathways. Besides, a surface ketene *C=C=O derived from *(OH)C=COH at high pH is attacked by OH$^-$ to produce acetate.[74] After the dimerization of adsorbed CO, the *CO–COH intermediate is formed, which further transforms into acetate.

Currently, most works are devoted to the CO$_2$RR/CORR for liquid alcohols, due to their high energy density, transportation readiness and well-established utilization infrastructure, especially the monohydric alcohols (methanol, ethanol). Apart from this, the higher-valued diols (ethylene glycol (EG), (CH$_2$OH)$_2$) attract increasing attention. The densely arrayed Cu nanopyramids could retain two oxygen atoms for hydroxyl formation fed by CO$_2$ or CO.[75] The unique spatial-confinement structure facilitates C–C coupling by lowering the reaction barrier, leading to EG generation. This is achieved by maintaining oxygen to the *COH–CHO pathway to EG, and inhibiting C–O breaking in *CH$_2$OH–CH$_2$O to further hydrogenation to EG.

2.3. In situ/operando characterization

To clearly understand the CO$_2$RR/CORR mechanism at ampere-level current density, in situ/operando investigations are powerful to provide valuable insights.[76–78] X-ray absorption spectroscopy (XAS) can determine the electronic structure and coordination environment of the absorbed element, which is classified into the X-ray absorption near edge structure (XANES) and the extended X-ray absorption fine structure (EXAFS) regions. XANES mainly probes the oxidation states and electronic configurations of active species, while EXAFS sheds light on the interatomic distances and the coordination with neighbouring atoms. XAS demonstrates the activity–structure relationship, probes the active sites, and reveals the structural evolution of active sites during the CO$_2$RR/CORR process. Very recently, operando XAS demonstrated that the active Cu$^+$ sites are stable during the industrial-current–density CO$_2$RR for C$_2+$ species production in both acidic (77.0% at 700 mA cm^{-2}) and alkaline (82.6% at 900 mA cm^{-2}) electrolytes.[77] The dendritic morphology of copper oxide catalysts is effective in simultaneously enriching K$^+$, increasing local pH, and promoting *CO adsorption. This updated mechanism indicated that the sharp surface

This journal is © The Royal Society of Chemistry 2025

Chem. Soc. Rev., 2025, 54, 6973–7016 | 6977

microarchitecture other than the oxidation state contributes to advancing the CO_2RR industrialization. Attractively, *in situ* XAS favors detecting electron donation onto the support and reactants and proposes a transient poisoning mechanism on Ni SAC for CO production in consideration of impurities (NO_x, and CN^-).[79] Besides, *in situ* XAS discovered that the F dopant with high electronegativity,[80] among the Cu NPs supported on a series of carbon doped with a heteroatom with varying electronegativity (B < P < S < N < F), contributes to reduced electron density on Cu and facilitates C_{2+} formation, showing 82.5% $FE_{C_{2+}}$ at 400 mA cm^{-2} with 44 h stability, due to the decreased C–C coupling energy barrier by F doping.

In situ and quasi *in situ* X-ray photoelectron spectroscopy (XPS) can characterize the changes in composition and chemical and electronic states of the catalysts during the CO_2RR/CORR process. Because of the different measured depths of XPS and XAS, these techniques are normally complementary to one another for investigating the bulk material properties. For instance, quasi *in situ* XPS demonstrated the surface chemical state changes from initial Cu^{2+}/Cu^+ to Cu^+/Cu^0 at applied negative potentials and the asymmetrical sites of Cu^+/Cu^0 remaining stable during the CO_2RR,[81] while *operando* XAS indicated the gradual evolution of the initial Cu_3P particles into Cu clusters upon increased negative potential under CO_2RR conditions. This reconstructed structure exhibited abundant asymmetrical sites facilitating C–C coupling, and the Cu cluster–support interaction promoted *CHCOH hydrogenation towards ethanol at industrial current density.

In situ X-ray diffraction (XRD) sheds light on the crystal phase of catalysts in real time, benefiting the analysis of the catalyst stability and phase transition. However, *in situ* XRD can only characterize the crystalline samples, and the local sites of components are impossible to detect due to the low spatial resolution. Time-dependent, synchrotron-based XRD probed the structural evolution of SnO_2 nanospheres during long-term CO_2 electrolysis at −1.2 V *vs.* RHE,[82] with transformation of SnO_2 nanocrystals into metallic Sn (*ca.* 23 nm) and maintaining the crystallite size over 30 h. Besides, a minor residual oxide phase was detected, due to the reoxidation in air exposure between electrochemical and XRD tests. The metallic Sn worked as active sites during the long-term CO_2-to-formate conversion. Moreover, *in situ* XRD of the $CuAu_{1\%}Ag_{0.2\%}$N-based GDE demonstrated the reduction of Cu_3N to Cu^0 during the CORR,[83] evidenced by no detection of the Cu_3N signal in *in situ* XRD. This transformation was also confirmed by the *in situ* Cu K-edge XANES with shift to low energies at applied CORR potentials.

Vibrational spectroscopy (UV/visible/IR photons) helps to elucidate the electrochemical performance by testing the molecular vibrations, such as the solvent, catalyst and reactants/intermediates/products, interpreting the catalytic mechanism. In addition, *in situ* vibrational spectroscopy also detects the transient changes of catalysts (redox transformation, oxide metallization). *In situ* UV-vis absorption spectroscopy is powerful to identify the reaction intermediates, such as in the reduction of Co(II) to Co(I) during the CO_2RR,[84] and the recovery

of the molecular phthalocyanine species after the electrode washing with trifluoroethanol.[85] Similar intermediate detection ability was also demonstrated by *in situ* XPS. Compared with them, *in situ* Raman and *in situ* IR are more widely applied for probing the real-time intermediates, because of the easier conversion of traditional Raman and FTIR analyses into *in situ* characterization techniques by rational design of the *in situ* cells, and more sensitive and accurate intermediate detection based on chemical bond vibration in the molecules.

In situ Raman helps to elucidate the catalytic mechanism by monitoring the catalyst structural evolution and the intermediate adsorption. When combined with *in situ* XRD, the catalyst structure evolution ($In_2O_3 \rightarrow In \rightarrow In(OH)_3$) and variations in intermediate adsorption were discovered to be related to overpotential and selectivity changes during the CO_2RR.[86] The innovative small current pre-evolution helps to construct a stable and porous catalytic interface, resulting in 88.7% $FE_{formate}$ at 500 mA cm^{-2}. *In situ* Raman not only tracked the structural evolution of the COC-NPs,[77] including the reduction of COC-NPs with anion leaching and the incomplete reduction of Cu^{2+} in Cu dendrites, but also verified that the CuO_x-dendrites promoted CO_{atop} formation for C–C coupling towards C_{2+} species. Similarly, high *CO coverage around the partially reduced Cu^+/Cu^0 active sites at the Ag/Cu_2O interfaces was tracked by *in situ* Raman, explaining the high production of C_{2+} ($FE_{C_{2+}}$ 73.6%, $j_{C_{2+}}$ 478.4 mA cm^{-2}) and C_2H_4 ($FE_{C_2H_4}$ 66%, $j_{C_2H_4}$ 429.1 mA cm^{-2}).[87] Additionally, *in situ* Raman indicated CO_{atop} on Cu changed from static high-frequency band CO to dynamic low-frequency band CO by incorporating Pd,[88] achieving increased C_{2+} production ($FE_{C_{2+}}$ 66.2%, $j_{C_{2+}}$ 463.2 mA cm^{-2}).

In situ attenuated total reflection surface-enhanced infrared absorption spectroscopy (ATRSEIRAS) detects the adsorbed molecule–catalyst surface interactions, evaluates the existence of individual metal atoms and quantifies their percentage, *in situ* collects interfacial information, reveals the persistent alkalinity near electrode surfaces during the CO_2RR, and probes the reduction pathways.[89–91] For example, *in situ* ATR-IR demonstrated the $HCOO^-$ presence and absence of other intermediates on the InNCN catalyst during the CO_2RR, elucidating the high formate production ($FE_{formate}$ 96%, $j_{formate}$ 400 mA cm^{-2}).[92] Besides, *in situ* FTIR also detected the enhanced *OCHO coverage on Sn–C/SiO_2 for CO_2-to-foramte conversion,[93] pronounced COOH formation and CO_2 consumption on CoPc-POP-c upon increasing overpotential for CO production,[94] and showed a strong *CHO signal on Cu-BIF/NO_3 for CO_2-to-C_1 and intensified *OCCHO and *CH_3CH_2O signals on Cu-BIF/Cl for CO_2-to-C_{2+},[10] respectively. Additionally, *operando* IR confirmed that increased K^+ concentration intensified the adsorption of CO_2 and *CO on Ni-NC,[95] which changed the interfacial water structure (H_2O to H_3O^+), accelerating CO production in strong acid.

Combination of *in situ* Raman and *in situ* IR helps to probe the key intermediates, revealing the catalytic mechanism.[96,97] For example, *in situ* Raman and ATR-SEIRAS verified that the Ag–Cu–nitrogen-doped carbon tandem catalysis system effectively enhances the linear adsorption of *CO and H_2O dissociation,

6978 | *Chem. Soc. Rev.*, 2025, **54**, 6973–7016

This journal is © The Royal Society of Chemistry 2025

promotes C–C coupling, and stabilizes *OCCOH for C_{2+} species production.[98] *In situ* Raman and *in situ* IR indicated that Cu NPs supported on electron-donating amine group modified single-walled carbon nanotubes (SWCNTs) presented enhanced *CHO coverage towards C–C coupling,[99] while Cu NPs on electron-withdrawing cyano modified SWCNTs preferred producing C_1 species. Besides, *in situ* electrochemical attenuated total reflection Fourier transform infrared spectroscopy (ATR-FTIR) and *in situ* Raman confirmed the *CO stabilization and promoted C–C coupling by C–Cu_2O NPs,[100] which contributed to CO_2-to-C_{2+} conversion with a high $FE_{C_{2+}}$ (76.2% at 800 mA cm^{-2}). To understand the relationship between the surface microenvironment and the CO_2RR performance, *in situ* surface-enhanced Raman spectroscopy (SERS) and *in situ* ATRSEIRAS were deployed to detect the key intermediates and molecular structures of functional groups and reveal the underlying mechanism.[101] The results demonstrated that the *CO coverage is considerably higher on the Cu nanorod developed by isopropanol (Cu-NR_{IPA}) than that by dimethyl sulfoxide (Cu-NR_{DMSO}) and EAC (Cu-NR_{EAC}), and the enhanced C–C coupling by Cu-NR_{IPA} was confirmed by the intense IR signal of *COOH and *OCCOH intermediates. Moreover, the Nafion ionomer exhibits various aggregation behaviours in solvents with different dielectric constants (ε), and increasingly aggregates under smaller ε, posing the *CO-incompatible –SO_3H groups away from the Cu surface, alongside the aggregated hydrophobic –$(CF_2)_n$– chains. This arrangement enhances *CO adsorption and promotes the HER, suggesting that the CO_2RR product distribution can be controlled by adjusting the dispersion solvent. For example, changing low-ε DMSO into moderate-ε IPA contributed to increasing $FE_{C_{2+}}$ from 67.5% to 90.5% at 800 mA cm^{-2} on Cu nanosheets.

In situ electron spin resonance (ESR) derived from magnetic resonance mainly detects the unpaired electron transitions under an applied magnetic field, and is appropriate to identify the existence of unpaired electrons or single electrons in molecular orbitals.[102] Radicals generated on a catalyst surface can be monitored by *in situ* ESR, providing insights into the reaction pathway and catalytic mechanism.

Apart from the structural information obtained from the above-mentioned techniques, *operando* electrochemical liquid-cell scanning transmission electron microscopy (EC-STEM) demonstrated the structural evolution of Cu nanocatalysts into active metallic Cu nanograins for the CO_2RR,[103] while *operando* 4D STEM in liquids,[104] with co-existing H_2 bubbles formed during the CO_2RR to create a thin liquid layer to improve spatial resolution for nanoscale dynamic evolution of catalysts, revealed the complex structure of active polycrystalline metallic Cu nanograins at solid/liquid interfaces. *In situ* environmental TEM (ETEM) was powerful to track the formation of a Bi–N–C SAC with Bi–N_4 sites on porous carbon networks,[105] with evolution from Bi nanoparticles to single atoms during the CO_2RR.

In situ mass spectrometry (MS) can monitor the catalytic products in real time, which helps to determine the onset potential and the product species at various potentials. This strategy has been devoted to detecting gaseous hydrocarbon products of the CO_2RR,[106] with utilization of pervaporation to separate and collect products continuously. In more details, according to the potential sweep from 0 to -2 V *vs.* SHE and the intensities of the different fragments, the products of H_2, CH_4, and C_2H_4 are recorded at a mass to charge ratio of 2, 15, and 26, respectively. Their corresponding onset potential is ~ -1.12 V, -1.64 V, and -1.53 V *vs.* SHE, respectively, indicating a much lower overpotential of hydrogen evolution products than the other CO_2RR products. In this work, a combination of an electrochemical scanning flow cell with an online mass spectrometer together with a gas purging system was designed to enable analyzing the volatile reaction products to screen the electrochemical reactions, which accelerates the catalyst material research and optimal condition determination for fabricating practical devices. However, analyzing the liquid products in real time is complex due to the ion suppression by the nonvolatile salts in electrolytes. To successfully detect the liquid products, the online electrochemical mass spectrometry method (EC/MS) was deployed to investigate the CO_2 reduction in sulfuric and perchloric acid on polycrystalline Cu.[107] Apart from identifying gas (CH_4, C_2H_4) and highly volatile product (CH_3OH, HCHO) formation, EC/MS also demonstrates that the formation of methane and formaldehyde is kinetically favored than that of ethene and alcohol in both electrolytes. The absorbed anion from the electrolyte determines the potential at which HCHO generates. The CO_2RR/CORR proceeds *via* an electrocatalytic hydrogenation process. Various products (H_2, CH_4, C_2H_4, CH_3OH, and C_2H_5OH) can be detected within one minute, but there are challenges because of the difficulty of delineating all the CO_2RR products due to the ionized and broken-down samples, and the product quantification issue by the low and/or ill-defined product collection. Despite these problems, a novel flow cell was designed to extract gas and liquid through a membrane,[108] achieving quantitation of H_2, C_2H_4, and propanol. This novel differential electrochemical mass spectrometer (DEMS) cell demonstrated CO_2RR on polycrystalline copper. The real-time quantification of products is determined by the function of the applied potential during linear sweep voltammetry within 1 h. Moreover, some other applications involving MS such as online inductively coupled mass spectrometry (ICP–MS) have demonstrated significant potential in investigating the catalyst degradation, validating the atomic elemental compositions of catalysts, and elucidating the effects of impurities, while synchrotron-radiation-based vacuum ultraviolet photoionization mass spectrometry (SVUV-PIMS) plays a crucial role in resolving the dynamic interfacial species evolution during the CO_2RR on Cu. *In situ* MS not only directly tracks the generation of gas/liquid intermediates and final products in real time, but can also be used to observe and quantify the local reaction environment.

Therefore, *in situ* characterization benefits identifying the intermediates/active sites/reaction pathways, studying the reaction environment effects, and probing the catalyst evolution, which shed light on the CO_2RR/CORR mechanism. *In situ* XAS/XRD/XPS monitors the element structural information, *in situ* UV/Raman/IR identifies the intermediates/functional groups/reduction routines, *in situ* MS focuses on determining the

This journal is © The Royal Society of Chemistry 2025

Chem. Soc. Rev., 2025, **54**, 6973–7016 | **6979**

Table 1 Summary of *in situ* and *operando* characterization techniques for the CO_2RR/CORR

Techniques	Functions	Sample requirements	Measurement conditions	Advantages	Limitations	Ref.
XAS	Oxidation state; Electronic structure; Spatial distribution; Coordination environment	Gas, liquid and solid samples	X-ray beam; A custom flow cell; Electrochemical workstation; Controlled atmosphere, temperature and pressure	Element specificity; Sensitivity; Not limited by the sample state	Average information on local structures; Difficult to analyze complex systems and light elements	77 and 103
XPS	Catalyst surface composition; Chemical states	Solid samples	Ultrahigh vacuum; Controlled temperature	Surface sensitivity; Excellent quantitative accuracy; Almost all elements (except H, He).	Hard to uncover the inner structural changes; Limited spatial resolution; Limited time resolution; Pressure gap	109
XRD	Crystal structure (phase composition, lattice parameters, preferred orientation)	Solid samples	Controlled atmosphere, temperature and pressure	Direct determination of size, shape, and orientation of the unit cell; Compatible with high temperature and high pressure	Low spatial resolution; Hard to detecting amorphous/weakly crystalline samples	82
UV	Light absorption capabilities; Electronic transitions (bandgap, excitons)	Solid or liquid samples	Controlled atmosphere, temperature and pressure	Non-destructive sampling; Simplify experimental process; Controlled-temperature detection	Low accuracy; Light source impact	84
Raman	Organic species or reactive radical; Identification of surface structural changes and adsorbed intermediates	Solid or liquid samples	Electrochemical workstation; An EC-RS cell; Controlled atmosphere, temperature and pressure	Non-destructive sampling; Not interfered by water; The high-speed acquisition; Wide spectra region	Spectroscopic limits; Hard to direct quantitative analysis; Limited intensity and spatial resolution	109 and 110
IR	Functional groups; Monitor adsorption and reaction processes	Solid samples	Electrochemical workstation; Three electrodes cell; Infrared spectrophotometer with a built-in mercury cadmium telluride (MCT) detector; Controlled atmosphere, temperature and pressure	Low cost, facile optical design and operation; High sensitivity; Fast characterization.	Limited IR transmission; Electrolyte interference; Limited absorption range.	109
ESR	Detect unpaired electrons (or single electrons) in molecular orbitals	Solid samples	Controlled atmosphere, temperature and pressure	Non-destructive; Specific detection of unpaired electrons	Low resolution; Difficulty of quantitative analysis	
TEM	Morphology changes of catalyst; Distribution of single atoms	Solid samples (<100 nm)	Ultrahigh vacuum; Controlled temperature	Real-time high-resolution imaging; Atomic resolution	The electron beam may damage the sample; Strict operating environment and sample preparation	103 and 104
MS	Qualitatively and quantitatively determine the product composition	Gas or liquid samples	Controlled temperature	High sensitivity; Real-time monitoring of reaction products	Hard to detect liquid products in real-time	106–108

6980 | *Chem. Soc. Rev.*, 2025, **54**, 6973–7016

This journal is © The Royal Society of Chemistry 2025

intermediates/final products, while in situ TEM tracks the morphological evolution of catalysts and the distribution of single atoms. Each technique exhibits advantages and disadvantages (Table 1), based on which, combining multiple in situ techniques promotes understanding the CO_2RR/CORR mechanism and enriching the structure database for machine learning, guiding to design more efficient catalysts for practical applications.

3. Principles of catalyst design for the CO_2RR/CORR at ampere-level current

Some works reported remarkable CO_2RR/CORR at real ampere-level current density (>1 A cm^{-2}, Fig. 1a and c). Such high reaction rates are technically significant and promising for practical applications. Herein, in-depth investigation into CO_2RR/CORR beyond 1 A cm^{-2} is discussed. Two aspects for achieving high current density should be considered. (1) Catalyst design – the scientific principles; (2) mass transfer management – technically.

Catalyst design for CO_2-to-CO conversion beyond 1 A cm^{-2} can be achieved by modulating the d-band of a metal center for efficient *COOH adsorption and *CO desorption, especially using square-pyramidal Ni–N_5,[47] NiN_4–O sites with an axial oxygen,[111] and Hg-CoTPP combined with N-doped graphene.[112] The Ni SAC derived from Ni-doped ZIF-8 exhibits abundant defective sites and a mesoporous structure for CO_2 adsorption and mass transfer, affording 96% FE_{CO} and 1.06 A cm^{-2}.[113] While Ni dual-atom sites facilitate hydroxyl adsorption to generate electron-rich active centers,[48] resulting in a moderate reaction barrier for *COOH formation and *CO desorption. This further results in over 99% FE_{CO}, 77 500 h^{-1} turnover frequency and j_{CO} approaching $\sim$1 A cm^{-2}. Other strategies to achieve CO_2-to-CO conversion beyond 1 A cm^{-2} include applying external magnetic field to promote CO_2 adsorption at Ni sites and suppress the HER,[114] depositing CoPc crystals on carbon paper to enhance surface charge transfer,[115] and introducing Ru atoms on the $Ce_{0.8}Sm_{0.2}O_{2-\delta}$ surface to alternate the catalyst electronic structure for achieving favorable oxygen vacancy formation and improved CO_2 adsorption and activation.[116] While modifying the Cu(200) nanocube surface by Cs atoms provides an effective strategy for ampere-level CO_2-to-ethanol conversion,[117] attributed to the stabilized C–O bond in oxygenate intermediates towards ethanol.

To promote *CO intermediate and *H coupling while minimizing side reactions (C–C coupling, H–H coupling) for CO_2-to-CH_4 at high current density,[118] Cu-based catalysts comprising a Cu–N coordination polymer and a CuO component were developed which can manage the key intermediates (*CO, *H). The Cu–N coordination polymer exhibited increased Cu–Cu distance favoring *CO hydrogenation over the dimerization, while the CuO component afforded sufficient *H supply, resulting in a fast CH_4 formation rate (3.14 mmol cm^{-2} h^{-1}) and 51.7% FE_{CH_4} at 1300 mA cm^{-2}.

Doping (Rh doped Cu,[119] S–Li co-doped Sn,[120] Eu-doped CuO_x,[121] S-doped BiS,[122] F-doped Cu,[123] Pb_1Cu single atom ally (SAA),[124] Mo_1Cu SAA,[125] and SAA-Zn_1Bi[126]) and alloying (Cu_6Sn_5,[127] Cu_9Ga_4[128]) indicated high activity and selectivity

for the CO_2RR beyond 1 A cm^{-2}. Among which, the Rh dopant exhibits a stronger oxygen affinity than Cu and facilitates *CH_2CHO adsorption and weakens the C–O bond, favoring ethylene production, Au dopants with weaker oxygen affinity than Cu promoted ethanol production by the C–O bond stabilization, while Ru with too strong oxygen affinity suffers from slow *O removal from the dopant site. Li dopants incur electron localization and lattice strains on Sn, which boosted CO_2 conversion to formate with enhanced activity and selectivity. The introduced Eu to Cu, compared to other lanthanide metals, undergoes Eu^{2+} reduction from Eu^{3+}, which prevents the nanoparticle agglomeration, achieving $\sim$80% $FE_{C_{2+}}$ at 1.25 A cm^{-2}. Apart from the metal dopants, non-metal dopants such as S and F effectively modulated the electronic structure of catalysts (Bi, Cu), promoted water activation and formation of the key intermediates (HCOO*, CHO) for formate and further C–C coupling towards C_{2+} species, respectively. Different from the promoted formation of HCOO* by Pb_1Cu and the moderate *OCHO adsorption by SAA-Zn_1Bi for formate, Mo_1Cu achieved atom-scale cascade catalysis for CO_2-to-C_{2+} conversion with remarkable $FE_{C_{2+}}$ (86.4%) and maximum $j_{C_{2+}}$ (1.33 A cm^{-2}). Mo sites facilitated water dissociation to *H, the Cu sites (Cu^0) far from the Mo atom promoted CO_2 conversion to CO, while the adjacent Cu sites ($Cu^{\delta+}$) near the Mo atom captured CO and *H to enhance CO conversion and C–C coupling. As for the Cu_6Sn_5 and Cu_9Ga_4 alloys, the former one exhibits strong *OCHO affinity and weak *H binding, delivering 91% $FE_{formic\ acid}$ at 1.2 A cm^{-2} in acid, while the latter one presents an elongated Cu–Cu distance for simultaneous reduced *CO repulsion and increased *CO coverage, which promoted C–C coupling towards C_{2+} species with maximum $j_{C_{2+}}$ (1.27 A cm^{-2}) and 71% $FE_{C_{2+}}$.

Alternation of the catalyst particle size or structure resulted in CO_2RR beyond 1 A cm^{-2}. By solely controlling the Cu nanocluster size from 200 to 0.5 nm, the selectivity shifted from ethylene to methane,[129] approaching 85% FE_{CH_4} and maximum j_{CH_4} (1.2 A cm^{-2}). This originated from the dominant Cu(111) facets at such extremely small size. While other works on lattice-distorted Bi,[130] highly exposed Bi(110),[24] and tensile strain engineering on non-defective Bi sites[131] or Cu(100),[132] and 5 nm Cu quantum dots with dominant Cu(100),[133] achieved outstanding CO_2RR with partial current density over 1 A cm^{-2}, due to the structure modulation effects on the intermediates of *OCHO for formate, and the enhanced *CO coverage for C–C/C–CHO coupling towards C_{2+}/C_2H_4, respectively. Interestingly, the in situ reconstructed Bi-based catalysts[20,23,25] optimized *OCHO adsorption and further conversion to *HCOOH towards formate, resulting in remarkable $j_{formate}$ over 1 A cm^{-2}, while the reconstructed CuO regulated by carbonate shell presents Cu(0) generation with abundant grain boundaries and small particles,[134] which stabilized *CO and facilitated C–C coupling, leading to $82.8 \pm 2.2\%$ $FE_{C_{2+}}$ at 2.0 A cm^{-2}.

Tandem catalysts (Cu/Fe–N–C s-GDE, Cu/Ag s-GDE,[135] CuO/Ni SAC,[51] Cu_2O/Al_2O_3,[87] and CuO/AgIO$_3$[136]) exhibited good control over the *CO intermediate and promoted C–C coupling at ampere-level current density, where the CO-selective catalysts enriched local CO coverage and enabled rapid consumption of

This journal is © The Royal Society of Chemistry 2025

Chem. Soc. Rev., 2025, 54, 6973–7016 | 6981

the *in situ* generated CO, subsequently, C_{2+} species formation was promoted on the Cu-based catalysts.

Surface modification of catalysts/electrodes by an indigo-based polymer (Id),[137] polymeric ionic liquids (PILs),[138] alkaline ionic liquids (AILs),[139] long alkyl chain (toluene),[49] sodium citrate,[140] and tetrabutylammonium cations (TBA$^+$)[141] is highly active and selective for CO_2/CO electrolysis beyond 1 A cm^{-2}, attributed to the optimized interfacial CO_2 binding affinity and accelerated formation of $^*CO_2^-$ and $^*COOH$ by Id, the alternated H$^+$ transfer, enriched K$^+$, and promoted C–C coupling by the PIL adlayer, the multi-roles of AILs (CO_2 accumulator/activator, intermediate stabilizer, and CO dimerization promoter), the remained and enriched CO_2 but blocked water transfer by toluene, Cu$^+$ stabilization and promoted $^*CO$ hydrogenation to $^*CHO$ by citrate anion, and the enhanced CORR activity and improved ethylene production by TBA$^+$, respectively.

Efficient mass transfer is a must for the CO_2RR/CORR at ultra-high current density (>1 A cm^{-2}). This can be achieved by a catalyst:ionomer bulk heterojunction to decouple gas, ion, and electron transport,[12] a GDE with a Cu-based ultrathin superhydrophobic macroporous layer[142] and a porous organic cage additive for highly enhanced CO_2 diffusion,[143] as well as the MgAl LDH nanosheet 'house-of-cards' scaffold to disperse CuO-derived Cu,[39] and a GDE with a mesopore-rich hydrophobic copper catalyst layer for fast CO transfer.[144] Moreover, Cu/Ag/Ni/Bi/Zn-based hollow fiber penetration electrodes (HFPEs), characteristic of a unique micron-scale hollow finer structure, oriented mass transfer from the inside to outside of the HFPEs, and construction of stable tri-phase interfaces, facilitating CO_2/CO activation and favoring key intermediate formation, are effective in promoting desorption of adsorbed species at ultra-high current densities over 1 A cm^{-2}, heightening the CO_2RR/CORR and suppressing the HER simultaneously. As a result, ultra-high partial current density (>1 A cm^{-2}) was achieved, together with outstanding product selectivity[145–147] and stability (>100 h).[148]

Furthermore, K$^+$ accumulation can be achieved by Cu nanoneedles,[149,150] which enables highly efficient CO_2/CO electrolysis.

At the device/system level, the PiperION membrane with high carbonate conductance demonstrates record high activity and selectivity for industrial CO_2-to-CO conversion in a tailed MEA,[151] while the utilization of a robust and efficient catalyst, stable three-phase interface and durable membrane afforded producing formic acid over 5200 h in the CO_2RR–hydrogen oxidation coupling system.[152] Optimization of the components (oxide-derived Cu, carbon-based GDE, and their assembly) demonstrates ultra-high-rate CO_2 electrolysis.[153] Another significant factor of CO_2/CO coverage,[154,155] controlled by CO pressure, can also be tuned for ultra-high rate CO_2RR/CORR.

Therefore, the key to enable the CO_2RR/CORR at ampere-level current is to develop efficient catalysts with improved activity and selectivity,[156] which can be realized by increasing the number of active sites and the intrinsic activity of each active site.[157] Another key to ampere-level CO_2/CO electrolysis is the mass transfer manipulation. Representative principles for catalyst design are summarized in this section, including alloying and doping, single

atom effects, regulation of the morphology and structure, oxidation state control, and organic molecule modification, while mass transfer will be discussed in the next section.

3.1. Alloying and doping

Bimetallic catalysts are effective in breaking the scaling relationship during the CO_2RR/CORR process (Fig. 2a), thereby stabilizing the intermediate and decreasing the overpotential and further improving the selectivity (Fig. 2c). For comparison, the pure Cu-based catalysts for CO_2/CO electrolysis at ampere-level are summarized (Fig. 2b). With CO_2 feed, pure Cu catalysts presented a $FE_{C_{2+}}$ ranging from 40% to 90.9% with more accumulation at 70% to 80%, lower than those of the alloys or doped Cu (80% to 94%, Fig. 2b). Similar trends were detected for C_2H_4 (32% to 67% vs. 60% to 70%) and ethanol (37% to 44% vs. 45% to 79%). Both pure Cu catalysts and alloys/doped Cu contributed to high C_1 species production (CH$_4$, formate) with FE_{CH_4} at 57% to 85% and $FE_{formate}$ over 90% to unity, respectively. CO-to-C_{2+} conversion by pure Cu catalysts exhibited $FE_{C_{2+}}$ at 75% to 93%, inferior to those of the alloys/doped Cu (80% to 96%). Besides, pure Cu catalysts facilitated acetate production (43% to 68%), while the alloys/doped Cu exhibits better capability of producing alcohols (ethanol, propanol, and C_{2+} alcohols) beyond acetate. Therefore, pure Cu-based catalysts are relatively difficult to achieve high activity and selectivity to C_{2+} species, due to their low adsorption ability to the key intermediates and the non-specific selective CO_2RR/CORR pathways. This can be addressed by doping/alloying to alternate the electronic circumstance of Cu-based catalysts. Normally, the dopants include non-metal elements (C, N, O, F,[123,158] P, S) and metal elements (Na, Mg, K,[159] Sc,[160] Mn, Co,[161] Ni, Cu,[162] Zn, Ga, Nb, Ru, Pd, Ag,[110,144,163] In, Sb, Te, Cs,[117] La,[164] Sm,[121] Eu, Gd, Au, Pb). The non-metal doping plays crucial roles in manipulating the electronic structure of active metal species and thus enhancing the electrochemical performance.[165,166] For example, among a series of heteroatom-engineered Cu (X–Cu, X = N, P, S, O),[38] N–Cu demonstrated the optimal CO_2-to-C_{2+} performance with 73.7% $FE_{C_{2+}}$ and 909 mA cm^{-2} $j_{C_{2+}}$, due to its enhanced $^*CO$ coverage, favorable $^*CO$ adsorption, and much slower local H proton consumption than Cu. S doping into Bi modulates the HCOO* formation towards formate,[122] achieving $\sim$95% $FE_{formate}$ at 2000 mA cm^{-2} in both alkaline and acidic flow cells, while S doping into Cu[167] and Sn[168] enhances the $^*OCHO$ coverage and promotes CO_2-to-HCOOH at industrial reaction rates, contributing to 92% $FE_{formate}$ with 321 mA cm^{-2} $j_{formate}$ and 92.15% $FE_{formate}$ with 730 mA cm^{-2} $j_{formate}$, respectively. Non-metal (S) and metal (Na, Ag) co-doped catalysts (Bi(110)–S–Na,[24] Ag–In–S[169]) illustrated outstanding formate production, due to the co-doping induced improved Bi–Bi metallic bonds, stabilized $^*OCHO$ and promoted water dissociation to H*, as well as the decorated interface strain for stabilizing the key intermediate and accelerating charge transfer.

Incorporating metal dopants into a second metal such as Cu–Bi,[25,171] Sn–Bi,[172] Pb–Cu,[124] Zn–Bi,[126] Sb–Bi,[172] Cu–Sb/Pd,[173] CuSb,[174] Co$_1$Cu,[175] Cu–Au,[176] and Cu–Sn[127] are highly selective to CO_2-to-C_1 conversions. The interaction effects in the

6982 | *Chem. Soc. Rev.*, 2025, **54**, 6973–7016

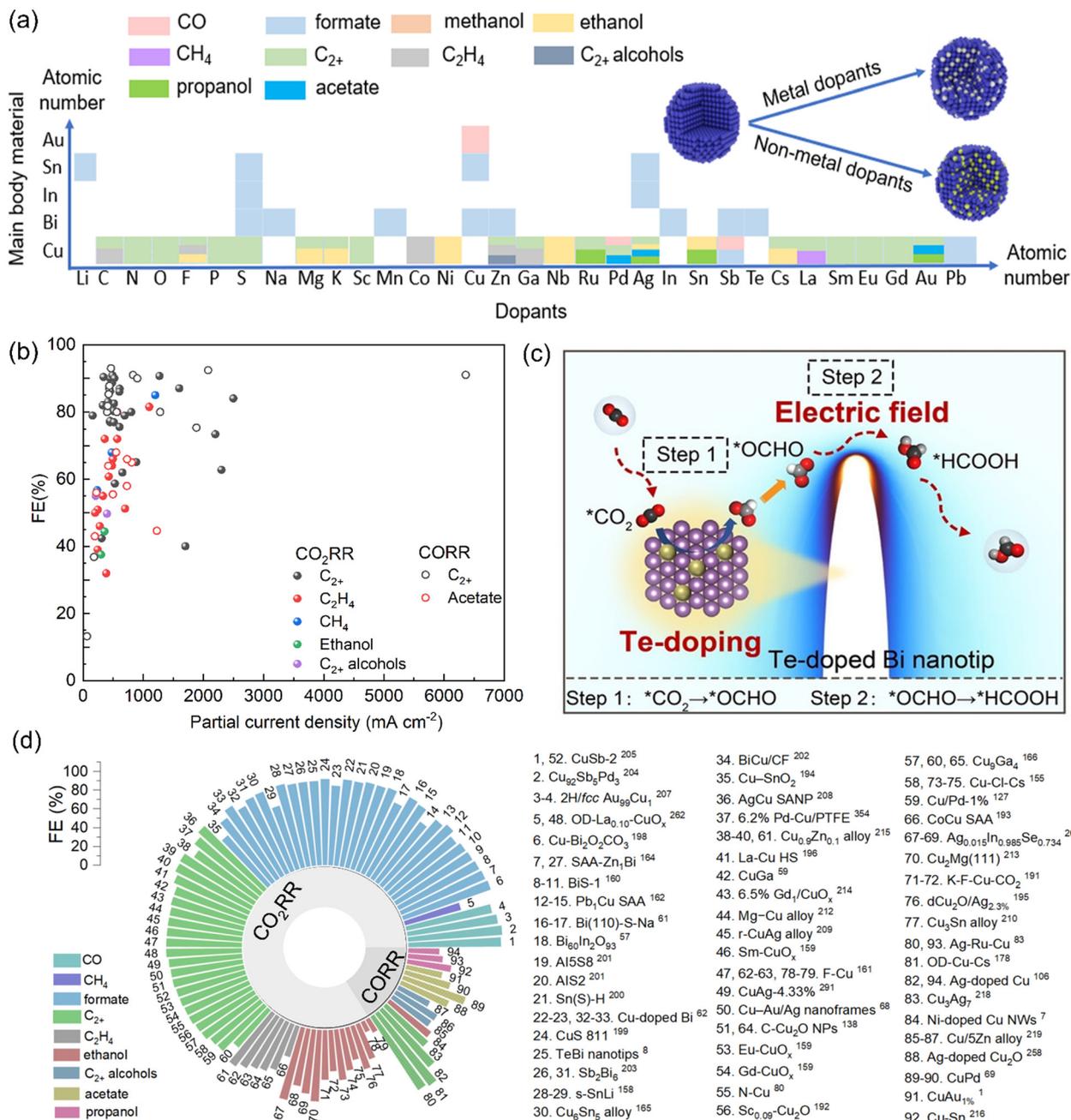This journal is © The Royal Society of Chemistry 2025

Fig. 2 Alloying and doping effects. (a) Summary of reported alloying and doping for ampere-level $CO_2RR/CORR$. (b) Summary of pure Cu-based materials for $CO_2RR/CORR$ at ampere current density (data from Tables S1 and S2, ESI†). (c) Summary of reported FE by alloying and doping (data from Tables S1 and S2, ESI†). (d) The proposed reaction mechanism for CO_2RR over TeBi NTs. The purple and brown balls represent Bi and Te, respectively. Reproduced with permission.[170] Copyright 2024, John Wiley and Sons.

alloys Cu–Bi,[25] Sn–Bi,[172] Zn–Bi,[126] and Sb–Bi[172] selectively stabilize *OCHO towards formate, while Pb–Cu[124] modulates the first protonation step of the CO_2RR and facilitates formate formation via HCOO* rather than COOH*. Apart from which, the unique high-curvature Te–Bi nanotips incur enhanced electric field to steer the *HCOOH formation (Fig. 2d),[170] thus decreasing the energy barrier for *OCHO and *HCOOH and affording high formate selectivity at low overpotential. As for CO_2-to-CH_4 conversion, the incorporated Cu single atom into

Cu enhances water activation and dissociation,[175] reducing the energy barrier for *CO hydrogenation. The modulated *CO adsorption configuration exhibited stronger bridge-binding, benefiting CH_4 production over the C–C coupling or CO desorption pathways.

The alloy effects on C_{2+} production are more complicated, either by Ag–Cu,[177,178] Cu–Pd,[88] Cu–Ag/Au,[179] Cu–Sn,[180,181] Cu–Ga,[22,128] Cu–Mg,[182,183] Gd–Cu,[184] Cu–Zn,[185] and Mo–Cu[125] from the CO_2RR, or by Cu–Sn,[186] Cu–Cd,[187] Cu–Au,[1]

This journal is © The Royal Society of Chemistry 2025

Chem. Soc. Rev., 2025, **54**, 6973–7016 | **6983**

Cu–Ag,[67,188] Cu–Zn,[189] and Cu–Pd[28] from the CORR. The introduced metals into the alloys contribute to enriching the *CO coverage and promoting C–C coupling. For instance, the Ag–Cu single atom alloy (SAA) enhances the *CO adsorption energy on Cu sites,[177] because of the compressive strain between the Cu atom and the adjacent Ag atom, and C–C coupling is promoted to produce C_{2+} species with high $FE_{C_{2+}}$ (94 ± 4%) under ~720 mA cm^{-2} at −0.65 V in an alkaline flow cell. While the introduced Mo sites promote water dissociation to *H,[125] the active Cu sites (Cu^0) far from the Mo atom activate CO_2 into CO, and the adjacent Cu sites (Cu$^{\&+}$) near the Mo atom capture CO and *H, thus promoting C–C coupling. The Mo–Cu single atom alloy demonstrated remarkable $FE_{C_{2+}}$ (86.4% at 800 mA cm^{-2}) and maximum $j_{C_{2+}}$ (1330 mA cm^{-2}).

The p–d orbital hybridization works as well in promoting C_{2+} production. The characteristic Ga–Cu interaction enhances the active site concentration and provides strong binding to the *CO intermediate and facilitates C–C coupling where a high $FE_{C_{2+}}$ (81.5%) at 900 mA cm^{-2} and −1.07 V vs. RHE were achieved.[22] This strategy can be extended to other p-block metal-doped Cu catalysts (CuAl, CuGe). Similarly, a Cu–Ga atomic alloy with both active (Cu(100), Cu(111)) and inert (Ga) *CO binding sites for locally enriched *CO coverage and reduced *CO repulsion was developed,[128] which delivered a peak $j_{C_{2+}}$ (1207 mA cm^{-2}), high $FE_{C_{2+}}$ (71%), and high-power capability (~200 W).

The product distribution of the CO_2RR can be modulated by varying the doping amount of the alien element.[88] For example, a small amount of Pd (0.25% and 0.5% Pd) doping to Cu facilitates C_{2+} production, while a higher Pd content (1–5%) leads to a 3–5-fold increase in FE_{CO}. Doping Sn atoms to Cu has been confirmed effective in compressing Cu atoms and enriching *CO on Cu sites. Low-entropy state CuSn alloy outperforms high-entropy state CuSn alloys (Cu_6Sn_5) with enhanced *CO adsorption capability and facilitates CO_2 reduction to ethanol.[180] Cu_3Sn exhibits substantially enhanced adsorption of the key intermediates (*CO and *CHCHOH) for ethanol formation, thus enabling high $FE_{ethanol}$ (>40%) at industrial current (900 mA cm^{-2}).

Stabilizing the Cu$^+$ sites by Mg modification promotes CO_2 electroreduction to C_{2+}.[182] Assisted by a fast-screening platform, Cu–Mg stands out among the 109 Cu-based bimetallic catalysts. The Mg modified Cu achieves 80% $FE_{C_{2+}}$ with 1000 mA cm^{-2} at −0.77 V vs. RHE, attributed to the stabilization of Cu$^+$ sites by Mg species for enhanced *CO coverage to facilitate C–C coupling. Different from the bimetallic alloys, copper co-alloyed with isolated Sb and Pd was designed for effective CO_2-to-CO conversion,[173] where Sb and Pd single atoms work synergistically to shift the Cu electronic structure to promote CO generation, suppress HER and enhance the catalyst stability by inhibiting atom aggregation. Almost unity CO selectivity at 402 mA cm^{-2} and high activity (1 A cm^{-2}) in neutral electrolyte, as well as ultrastability of 528 h at 100 mA cm^{-2} with over 95% FE_{CO} were achieved.

The alloy effect also applies for the CORR.[1,28] Modulating the active sites by developing atomic interfaces or grain boundary sites is able to boost n-propanol synthesis from the CORR. An asymmetric C–C coupling active site was constructed wherein the adjacent Cu atoms exhibit different electronic structures for interaction with two adsorbates to activate the asymmetric reaction.[67] Ag doping into Cu results in arising strain and ligand effects, which determine the asymmetry among the neighbors' energetics. The Ag-doped Cu provides the optimal activity to C_1–C_1 and C_1–C_2 coupling for C_2 and C_3 production, respectively. $FE_{n-propanol}$ of 33 ± 1% and a cathodic energy conversion efficiency of 21% for CO-to-n-propanol conversion are achieved.

3.2. Single atom effects

Single atom catalysts (SACs) featured by isolated metal atoms distribution on various supports are effective in catalyzing the CO_2RR/CORR,[43,83,190–198] due to their advantages of maximum metal utilization, well-defined active sites, strong atom–support interaction, suppressed HER, and outstanding catalytic activity. In this section, we mainly focus on the representative M–N–C structured SACs,[199,200] which are mostly studied both experimentally and theoretically.

Different metal elements (Al,[201] Mn, Co,[112,202–205] Ni,[111,198,206–210] Zn, Cu,[211–216] Ga,[217] Se, Rh, Ag,[218,219] Cd, In,[220] Sn, Cs,[221] Bi, Ru,[116] La, Ce, Pr, Nd, Sm, Eu, Gd, Tb, Dy, Ho, Er, Tm, Yb, Lu[196]) have been selected as metal centers (Fig. 3a), among which, the typical Ni, Co, Ag SACs are highly selective to CO production at ampere-level current density (Fig. 3c); Bi, In, Zn, Ag and Sn SACs favor generating formate; while Cu SACs are unique for hydrocarbon and multi-carbon formation. The typical Ni–N_4 sites can enhance the adsorption energy of the key intermediates (CO_2* and COOH*),[27] and afford abundant defective sites,[222] assisted by the mesoporous architecture for fast electron and mass transfer,[223] boosting the CO_2-to-CO conversion. Interestingly, the NiN$_x$ sites proceed structural evolution upon varying the thermal temperature (Fig. 3b).[224] The shortened Ni–N bonds in compressively strained NiN$_4$ sites produced at 900 °C are intrinsically active and selective to CO, while the NiN$_3$ sites activated at higher temperature (1200 °C) exhibit not only the optimal local structure but also superior CO activity and selectivity to NiN$_4$. Thus, a high FE_{CO} (>90%) and an industrial j_{CO} (726 mA cm^{-2}) are achieved in a flow cell. In comparison, the square-pyramidal Ni–N_5 site outperforms the planar Ni–N_4 site for industrial-scale CO_2-to-CO conversion,[47] because of the increased and decreased energy levels in d_{z^2} and $d_{xz/yz}$ orbitals, respectively, which facilitate CO_2 activation, lower the energy barrier and benefit CO desorption.

Apart from Ni SACs, Zn SAC[225] and Co SAC[226] also contribute to industrial-scale CO_2-to-CO conversion, due to the COOH* intermediate stabilization and HER suppression by the unsaturated Zn–N_3 site with the electron-rich environment of Zn, and the isolated CoN$_4$ sites, respectively. Introducing heteroatoms such as S, P, F into the active sites is one of the main methods to modulate the electronic structure.[227] For instance, a series of Co–S_xN_{4-x} (x = 0, 1, 2, 3) SACs were designed by a thermal replacement of coordinated N with S,[228] with Co–S_1N_3 exhibiting the balanced bindings to COOH* and CO*, thus delivering the optimal FE_{CO} (>90%). This coordination tailoring provides a rational approach to control the catalytic performance.
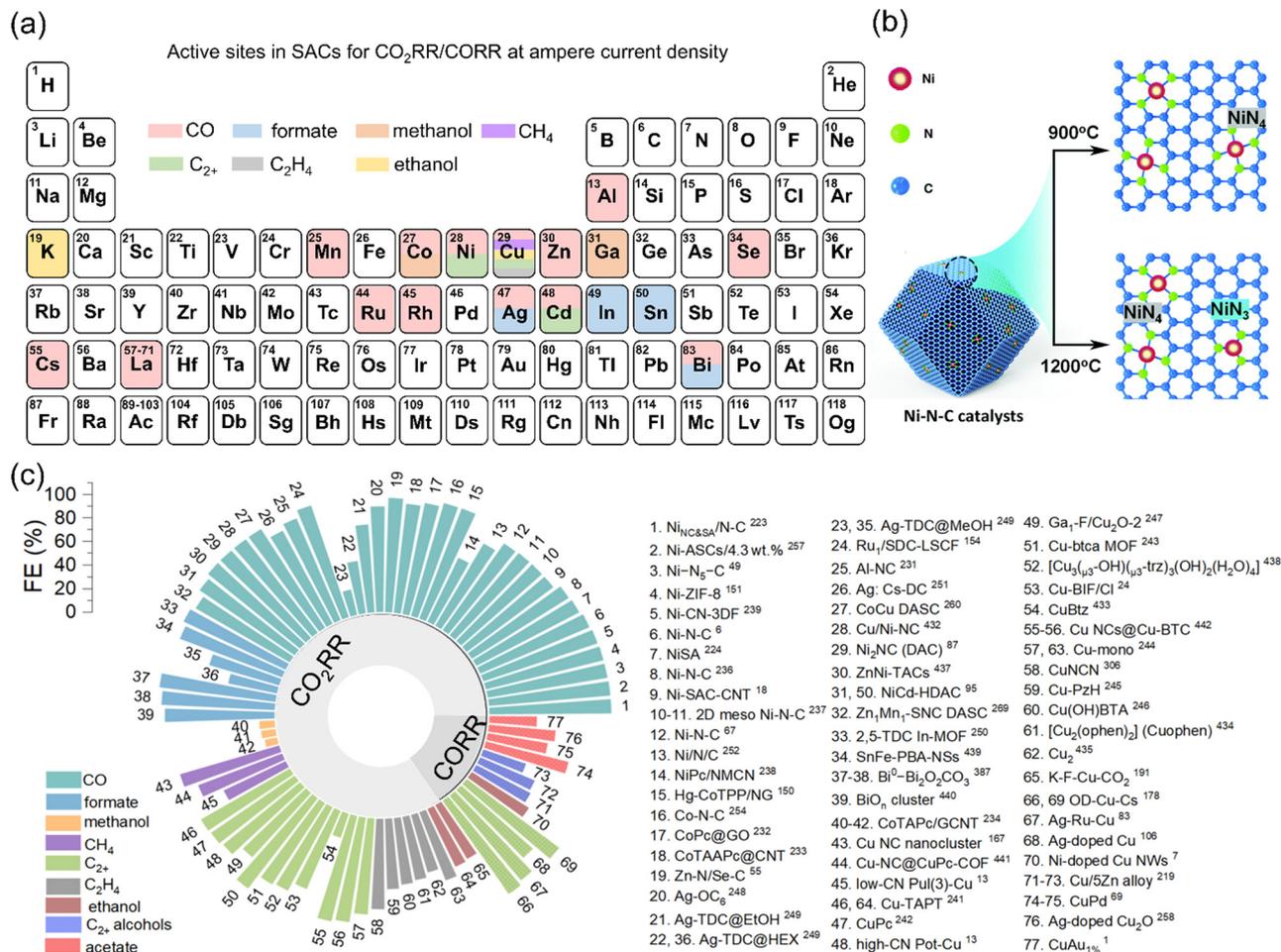
6984 | Chem. Soc. Rev., 2025, **54**, 6973–7016

This journal is © The Royal Society of Chemistry 2025

Fig. 3 Single atom effects. (a) Summary of reported active elements in SACs for CO_2RR/CORR at ampere current density. (b) Synthesis scheme of Ni–N–C. Reproduced with permission.[224] Copyright 2022, Royal Society of Chemistry. (c) Summary of reported FE by SACs (data from Tables S1 and S2, ESI†).

Increasing the metal loading in SACs is considered promising to enrich active sites, thus promoting the CO_2RR. The high loading Ni SAC (4.3 wt%) outperformed the low loading one (0.8 wt%) towards CO production at industrial-level current.[229]

A few studies are devoted to SACs for the industrial-scale CORR.[1,187] For instance, Cu atoms can be anchored on $Ti_3C_2T_x$ nanosheets for CO-to-C_{2+} conversion.[191] The atomically dispersed Cu–O_3 sites facilitate C–C coupling to form the key *CO–CHO species and further lower the energy barrier of the potential-determining step, thereby contributing to high activity and selectivity for C_{2+}. Cu can also support other single atoms (Ni,[230] Pd,[28] Ag,[231] Au[1]) for efficient CO-to-C_{2+} conversion as well.

Apart from SAC, dual atom catalysts (DACs) are also effective for CO_2-to-CO, where the atom pairs cooperate to facilitate *COOH formation and *CO desorption. For example, the hydroxyl adsorbate-induced Ni dual-atom sites (Ni_2N_6OH) afford fast CO_2RR kinetics,[48] suppress the HER, and promote hydroxyl adsorption to generate the electron-rich active centres, which favor CO_2 activation, lower the energy barrier for *COOH formation and facilitate *CO desorption.

Introducing another metal atom into SACs can effectively modify the electronic structure of the simple active sites and further improve the catalytic activity. The Ni–Fe DAC with neighboring Ni–N_4 and oversaturated Fe–N_5 moieties[232] and Co–Cu hetero-diatomic pairs[233] facilitate CO_2 activation and *COOH formation, due to the effective synergistic electronic modification of the dual atom sites, thus promoting CO production with almost unity selectivity at industrial current density.

3.3. Morphology and structure regulation

Regulating the morphology and structure is an alternative route to influence the CO_2RR/CORR performance (Fig. 4a). Different morphologies have been engineered to enhance their catalytic behaviors, such as nanoparticles,[27,100,234–236] nanotubes[97,222] or nanowires,[230] nanosheets,[237–239] needles,[149] cavities,[240,241] 3D structure,[242,243] core–shell,[244,245] hierarchical,[223] nanospheres,[47] hollow spheres,[246] accordion-like layered,[247] flower-like,[248] nanotips,[170] nanocubes,[179] multi-shell,[249] nanocages,[213] nanoribbons,[250] arrays,[251] polygon facets,[252] snowflake-like,[253] dendritic,[141,180] nanorod/nanosheet hierarchical,[254] and

This journal is © The Royal Society of Chemistry 2025

Chem. Soc. Rev., 2025, **54**, 6973–7016 | **6985**
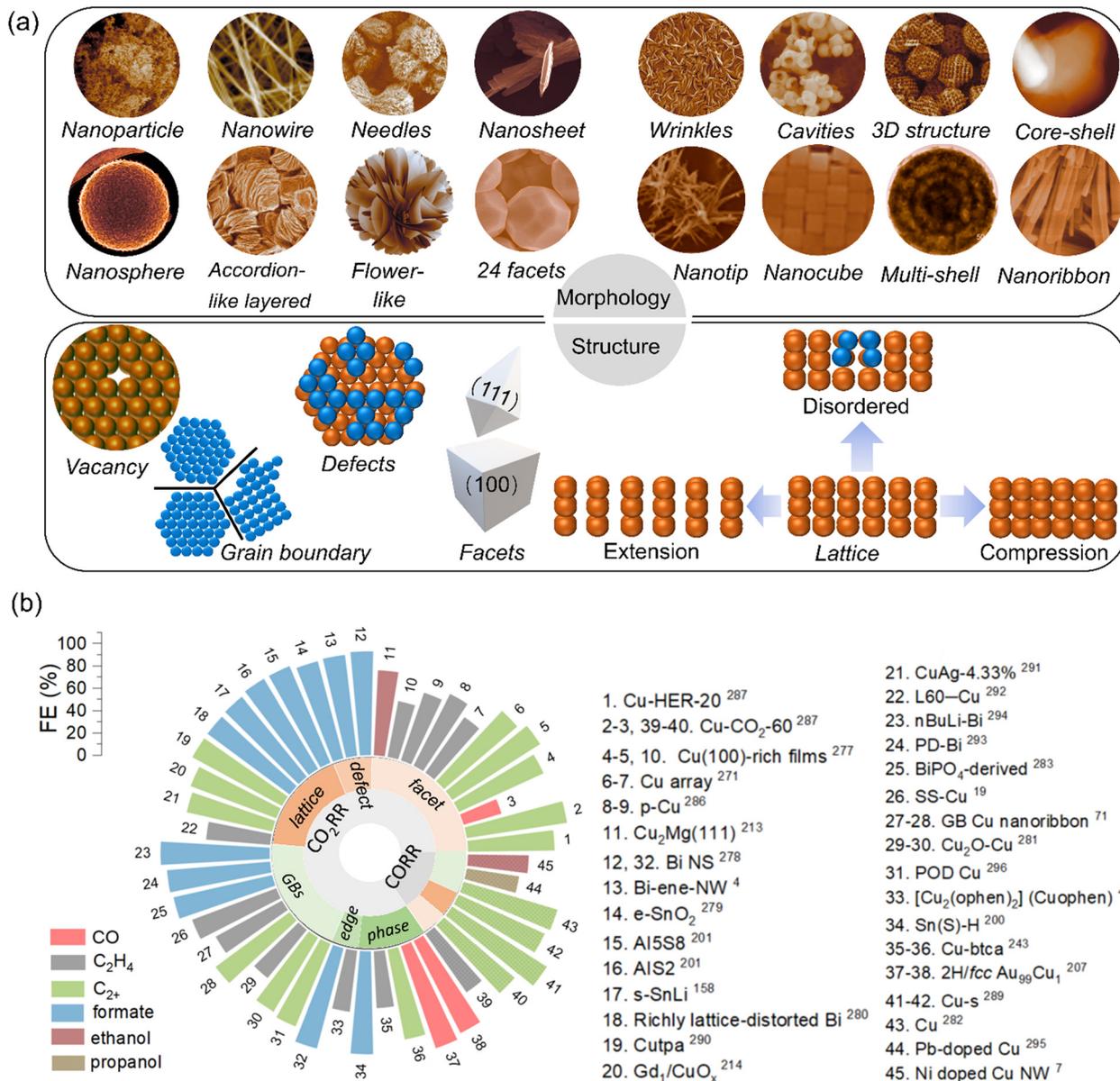
Fig. 4 Morphology and structure effects. (a) Summary of morphology and structure control over catalysts. (Nanowire, reproduced with permission.[230] Copyright 2024, John Wiley and Sons. Needles, reproduced with permission.[149] Copyright 2024, Elsevier. Wrinkles, reproduced with permission.[258] Copyright 2023, John Wiley and Sons. Cavities, reproduced with permission.[240] Copyright 2023, American Chemical Society. 3D structure, reproduced with permission.[242] Copyright 2023, John Wiley and Sons. Core–shell, reproduced with permission.[244] Copyright 2024, Springer Nature. Nanosphere, reproduced with permission.[47] Copyright 2022, John Wiley and Sons. Accordion-like layered, reproduced with permission.[247] Copyright 2025, John Wiley and Sons. Polygon facets, reproduced with permission.[252] Copyright 2024, John Wiley and Sons. Nanotip, reproduced with permission.[170] Copyright 2024, John Wiley and Sons. Nanocube, reproduced with permission.[179] Copyright 2020, John Wiley and Sons. Multi-shell, reproduced with permission.[249] Copyright 2023, John Wiley and Sons. Nanoribbon, reproduced with permission.[250] Copyright 2023, Elsevier.) (b) Summary of the reported FE by regulated structure (data from Tables S1 and S2, ESI†).

mesostructures.[255] The well-established morphology results in efficient mass and electron transfer and active site exposure.[94] For example, electron and mass transfer can be facilitated by developing a nanoporous Cu with 3D interconnected pores of 100–200 nm in diameter,[256] hydrophobic porous Cu_2O spheres with varying pore sizes,[257] and an ordered macroporous carbon skeleton with mesoporous "wall" supported P modified Bi atomic site,[243] which promoted gas transfer across the electrode–electrolyte

interface, afforded fast CO_2 transfer and trapped compressed CO_2 to construct abundant and stable triple-phase interfaces, and facilitated CO diffusion, thus contributing to exceptional production of C_{2+} ($\approx 62\%$ $FE_{C_{2+}}$, 653 mA cm^{-2} $j_{C_{2+}}$), 75.3% $FE_{C_{2+}}$, and CO ($>90\%$ FE_{CO}, 414 mA cm^{-2} j_{CO}). Especially, to enrich the concentration of the limited K^+/H_2O and facilitate water uptake *via* electro-osmosis,[149] needle-array catalysts were designed with intensified electric fields at the tips. This unique

interface overcomes the restricted K^+/H_2O migration in the catholyte-free MEA for the CORR, where no aqueous electrolyte is maintained to afford the three-phase interface formation. A large current density of 2500 mA cm^{-2} at a very low potential of 2.7 V was achieved.

By regulating the shape (confinement degree) and dimension of the confined space of the wrinkle structured Cu,[258] the CO_2RR product selectivity can be alternated without varying the intrinsic properties of Cu. The selectivity of CH_4 and EtOH was affected by the shape, with favorable production on non-folded and folded structures, respectively, while the C_2H_4 selectivity was dominantly influenced by dimension of geometry which increased upon higher depth of wrinkle. This product selectivity difference came from the changes in structure induced local pH and local intermediate confinement, where the non-folded structure favors protonation while the folded structure favors C–C coupling. For example, the Cu_2O catalyst featuring a nanosheet-stacked sphere architecture with abundant open and deep conical cavities facilitates timely refreshing of active sites in its depths[259] and the fast efflux of the product C_2H_4 with high local concentration from the elongated channels within the cavity. This design outperforms the hollow Cu_2O sphere with single cavities and solid Cu_2O spheres, exhibiting maximum $FE_{C_{2+}}$ (81.7%) with $j_{C_{2+}}$ (286 mA cm^{-2}) and over 40.0% cathode power conversion efficiency.

Apart from morphology control, regulating the catalyst structure (vacancy, grainy boundary, phase, facets, defects, lattice) also boosts the CO_2RR/CORR performances (Fig. 4a).[251,260–266] Among which, the catalysts with regulated structure are highly selective to C_1 species (CO, formate, Fig. 4b), followed by C_{2+} ones (C_2H_4, ethanol, propanol). To target the post-C–C coupling reaction intermediates other than C–C coupling,[267] a series of core–shell vacancy engineering catalysts were designed for efficient CO_2RR with sulfur atoms in the nanoparticle core and copper vacancies in the shell for propanol and ethanol production. The engineered catalysts, compared to Cu NPs, exhibited a 16-fold larger alcohol-to-ethylene ratio, directing to alcohols other than alkenes. Creating lithium vacancies (V_{Li}) in [CuO_4] sites contributed to 90.6 ± 7.6% $FE_{C_{2+}}$ with 706 ± 32 mA cm^{-2} $j_{C_{2+}}$,[50] as V_{Li} shortens the distance between adjacent [CuO_4] layers and decreases the coordination number of Li$^+$ around each Cu, thus promoting CO–CO coupling. Introducing interfacial oxygen vacancies in neighboring Cu (Ov–Cu) pair sites promoted CO_2-to-ethanol conversion,[268] realizing 48.5% $FE_{ethanol}$ and 344 mA cm^{-2} $j_{ethanol}$ in acid.

Exposing the selective crystal facets of electrocatalysts is a potential approach to generate specific CO_2RR products.[269] *In situ* electrodeposition of copper during CO_2 reduction preferentially exposed Cu(100) facets,[270] due to the strong interactions between the Cu(100) facets and CO_2RR intermediates such as CO_2*, COOH*, CO*, H*. Using the Cu(100) facet rich catalyst, high $FE_{C_{2+}}$ (90%), $j_{C_{2+}}$ (520 mA cm^{-2}), full-cell C_{2+} power conversion efficiency (37%), and stable C_2H_4 selectivity over 65 h at 350 mA cm^{-2} are obtained in MEA. Ni doping into the Cu(100) surface reduced the kinetic barrier of the ethanol path *via* facilitating *H formation,[230] achieving 86.1% $FE_{C_{2+}}$ and

60.8% $FE_{C_2H_4}$ at 700 mA cm^{-2}, and 54% $FE_{ethanol}$ and a 300-h stability, respectively. The Cu(100)/Cu(111) interfaces afford a favorable local electronic configuration to improve *CO adsorption and reduce C–C coupling energy barriers,[271] surpassing respective Cu(100) and Cu(111) surfaces. Therefore, efficient CO_2-to-C_{2+} conversion is facilitated with 74.9 ± 1.7% $FE_{C_{2+}}$ at 300 mA cm^{-2}.

Lattice engineering contributes significantly to producing hydrocarbon/multi-carbon. Introducing lattice tension enhances CO chemisorption on the Cu surface by mitigating the dipole–dipole repulsion,[272] which favors C–C coupling at high CO coverages. A spindle-shaped copper with 4% lattice tension is highly active and selective to multi-carbon olefins and oxygenates, exhibiting 1.0 A cm^{-2} current density with 84% $FE_{C_{2+}}$ at 2.4 V in MEA. Similar tensile strain engineering is obtained by electro-reducing CuO precursors with different crystallinity,[273] guiding Bi-MOF-TS catalyst reconstruction to generate continuous vacancies and activate more inert sites,[131] and introducing tension strain heteatom dopants (Gd,[184] Pd, Au, Ag,[274] Li[120]). The former strategy enables the co-adsorption of *CO and *OH in high concentrations to promote *CO dimerization and suppresses the HER, resulting in 90.9% $FE_{C_{2+}}$ and 486.1 mA cm^{-2} $j_{C_{2+}}$. The second strategy introduced weak tensile strain on the whole scale non-defective Bi sites, which enhanced *OCHO adsorption and decreased the reaction barrier, resulting in impressive $j_{formate}$ (995 ± 93 mA cm^{-2}) and $FE_{formate}$ (96 ± 0.64). Gd doping into Cu_2O promoted CO_2 activation, stabilized O*CCO and favored C–C coupling to give 81.4% $FE_{C_{2+}}$ and 444.3 mA cm^{-2} $j_{C_{2+}}$. The Ag doping into Cu outperformed Pd and Au with better ability to affect the d-band center of Cu to stabilize *CO and facilitate C–C coupling, thus delivering 77.9% $FE_{C_{2+}}$ at 300 mA cm^{-2}. In contrast, the regulated Cu(111) lattice strain with 11.4% compression exhibited reduced surface energies for lower C–C coupling reaction free energy,[275] compared to the pristine lattice and 10% compressed lattice, which promotes spontaneous *O splitting after OC–CHO coupling and the *CCH formation for C_2H_4.

Grain boundary (GB) engineering provides a powerful approach to enhance the CO_2RR/CORR performance. For example, owing to the abundant GBs on Bi-based catalysts, the CO_2 adsorption is promoted and CO_2•$^-$ intermediate is stabilized, leading to facilitated CO_2 activation and enhanced HCOOH production (91.9% FE_{HCOOH} at 600 mA cm^{-2}) in a flow cell,[276] as well as ~97% FE_{HCOOH} with ~450 mA cm^{-2} j_{HCOOH} in an all-solid-state CO_2RR system.[277] Similarly, the abundant GBs on Cu nanoribbons,[250] developed by stacking tiny nanoparticles with exposing Cu(111), Cu(200) and Cu(220) facets, enhanced CO_2 activation and promoted *CO formation and adsorption, thus promoting C–C coupling into *OCCO and *OCCOH and enhancing C_2H_4 and other C_{2+} species production. Introducing numerous atomic Pb-concentrated GBs to Cu helps to stabilize abundant low-coordinated Cu sites,[278] which improved *CO coverage, and created a structurally flexible Pb–Cu surface to adaptively stabilize the key intermediates (*COCOH, *COCOHCO, *COCCH$_2$), thus boosting CO-to-*n*-propanol conversion with 47 ± 3% $FE_{propanol}$ with 25% EE_{half} in a flow cell. Especially, CO_2/CO-assisted generation of GBs has been

This journal is © The Royal Society of Chemistry 2025

Chem. Soc. Rev., 2025, **54**, 6973–7016 | **6987**

demonstrated effective in promoting CO adsorption and C–C coupling for C_{2+} species production. The GBs in perovskite oxide-derived Cu induced by CO_2-assisted La leaching helped trapping *in situ* generated defective sites,[279] illustrating maximum $FE_{C_{2+}}$ (80.3%) with over 400 mA cm^{-2} $j_{C_{2+}}$. Very recently, the low-coordinated amorphous GB Cu defect sites exhibit strong adsorption to *OH and CH_2CHO^* which facilitates C–O breaking and producing C_2H_4,[280] while the medium-coordinated GB rich Cu presents weak *OH and CH_2CHO^*

adsorption, favouring C_2H_5OH production through the protonation on β-C of CH_2CHO^*. Therefore, high full-cell $EE_{ethanol}$ (29%) and $EE_{C_2H_4}$ (25.6%) were achieved, as well as 63.4 ± 1.5% $FE_{C_2H_4}$ at 12.5 A in a 25 cm^2 MEA.

3.4. Oxidation state alternation and oxide derived Cu modification

Manipulation of the oxidation states,[281] especially copper species (Cu^0,[282] Cu^+, $Cu^{\delta+}$ state, Cu^{2+}), as one of the major principles to tune the catalyst performance (Fig. 5a and b),
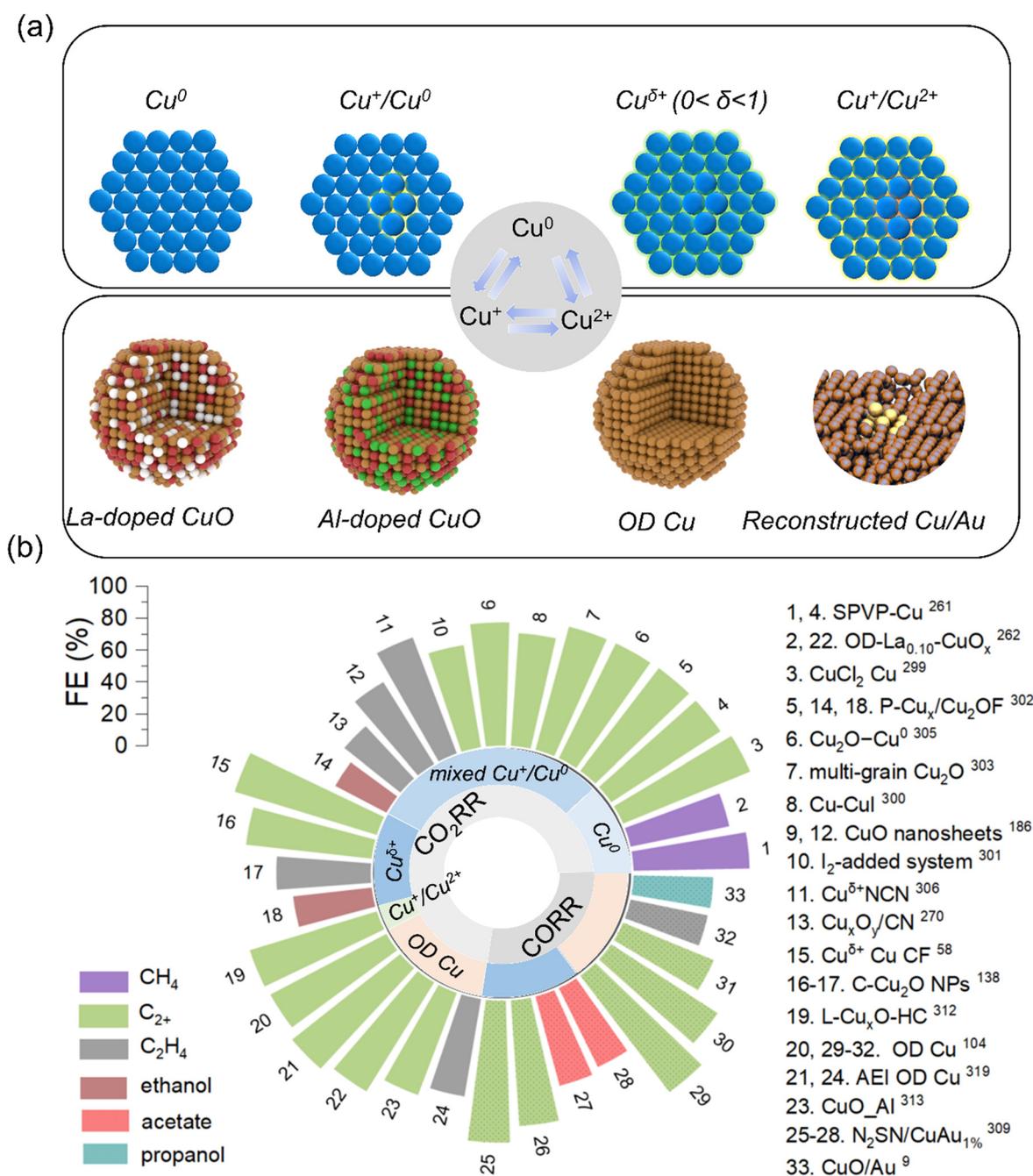

Fig. 5 Regulated oxidation state and modified OD-Cu/CuO. (a) Summary of the regulated oxidation states and modified OD-Cu/CuO. (Reconstructed Cu/Au, reproduced with permission.[283] Copyright 2024, American Chemical Society.) (b) Summary of the reported FE of the $CO_2RR/CORR$ products in this section (data from Tables S1 and S2, ESI†).

6988 | *Chem. Soc. Rev.*, 2025, **54**, 6973–7016

This journal is © The Royal Society of Chemistry 2025

has effects on the local electronic structure of materials. For instance, sufficient polyvinyl pyrrolidone (PVP) capped Cu NPs contributes to presence of complete Cu^0 species,[234] while the deficient PVP capped Cu NPs (DPVP-Cu) demonstrate an oxide structure with face-centered cubic Cu and partial Cu_2O species in the inner and outer layer, respectively. The former favors CH_4 production, displaying a 70% FE_{CH_4} at >200 mA cm^{-2}, while the latter mainly converts CO_2 into C_{2+} species (C_2H_4, C_2H_5OH, CH_3COOH, and C_3H_7OH) with $>80\%$ $FE_{C_{2+}}$ at 300 mA cm^{-2}.

The mixed Cu^+/Cu^0 states facilitate CO adsorption and benefit C–C coupling towards C_{2+} species. The Cu^+/Cu^0 interface controlled by physically mixing Cu nanoparticles and CuI powders,[284] or I_2 addition involved strategy[285] boosted CO_2-to-C_{2+} conversion with over 70% $FE_{C_{2+}}$ at industrial-scale current density. The Cu(I)/Cu(0) interfaces with an optimal electronic structure, engineered by a fluoride-assisted pulse-sequence method, play crucial roles in the CO_2-to-ethnaol conversion.[286] The close Cu(0)–Cu(I) coupling promotes COH* formation and directs the key intermediate OCCOH* toward ethanol, while the Cu(I) sites afford CO to generate ethylene on the Cu(0) sites. This coexistence of Cu^0 and Cu^+ during the CO_2RR can also be achieved by grain refining,[287] fluoride-assisted pulse-sequence method,[286] *in situ* electrochemical reduction of CuO nanosheet/graphene oxide dot hybrids,[288] co-feeding H_2O and CO_2 on the Cu_2O–Cu^0 interfaces,[289] applying nitrogen-doped carbon (CN) coating,[246] constructing a cyanamide-coordinated isolated copper framework ($Cu^{\delta+}NCN$) with both Cu^0 and Cu^+,[290] modification by pyroglutamic acid,[291] introducing Ag single atoms to stabilize Cu^+ in Cu/Cu_2O,[292] and constructing $Ag/Cu^+/Cu^0$ interfaces.[110]

The $Cu^{\delta+}$ state ($0 < \delta < 1$) can be stabilized by surface coordination *via* Cu(II) carboxylate,[21] doping with interstitial carbon atoms,[100] modification by electron-withdrawing molecule,[293] creating dynamically stable $Cu^0Cu^{0.18+}$ OCa motifs by insoluble carbonate,[294] and developing the unique Pr–O–Cu linkage in the stable oxide heterointerfaces.[295] Attributed to their roles of generating rich active sites, preserving stable triphase interface, optimizing the *CO adsorption for its dimerization, creating abundant unsaturated Cu–O bonds, alternating the Cu oxidation state to retain $Cu^{\delta+}$, reducing the C–C energy barrier, and alternating the binding strength and binding type of *CO, the CO_2/CO-to-C_{2+} conversion at industrial-scale current densities is significantly boosted. These five strategies result in 90.6% $FE_{C_{2+}}$ with 453 mA cm^{-2} $j_{C_{2+}}$, 76.9% $FE_{C_{2+}}$ with 615.2 mA cm^{-2} $j_{C_{2+}}$, 89% $FE_{C_{2+}}$ with 397 mA cm^{-2} $j_{C_{2+}}$, 83.7% $FE_{C_{2+}}$ with 393 mA cm^{-2} $j_{C_{2+}}$, and 71.3% $FE_{C_{2+} alcohols}$, respectively. In addition, higher oxidated Cu^+/Cu^{2+} interfaces demonstrated 81% $FE_{C_{2+}}$ at 900 mA cm^{-2}.[296]

Oxide-derived copper (OD-Cu) has been reported highly selective to C_{2+} production. However, various CuO_x precursors can lead to their reconstruction and product selectivity. Introducing new dopants is a favorable strategy to promote the catalytic activity of OD-Cu. Incorporation of Al dopants to OD-Cu induces CuO reconstruction into OD-Cu,[297] forming nanoflakes, which affords high hydrophobicity and high electrochemically active surface area. The doped catalyst exhibits high

$FE_{C_{2+}}$ (68.4%) and large $j_{C_{2+}}$ (478.7 mA cm^{-2}), far surpassing those of the undoped one, while La doping contributes to alternating the phase composition of OD-La–CuO_x and higher *H concentrations,[235] controlling the electron selectivity and steering the CO_2RR products. Differently, the intercalated I into OD Cu boosts CO_2 and CO adsorption,[298] during the CO_2RR process, the excess I release enhances the surface roughness, while the remaining I regulates the chemical state of the surface Cu. Therefore, the I modified OD Cu exhibited 79.5% $FE_{C_{2+}}$ and 43.5% $EE_{C_{2+}}$ at 300 mA cm^{-2}. Interestingly, when introducing Au NPs during the CORR, CuO nanosheets *in situ* transformed into undercoordinated Cu sites around Au NPs,[283] which facilitate CO binding and stabilize C_2 species to *n*-propanol. The Au directed Cu reconstruction contributes to high $FE_{n\text{-propanol}}$ ($\sim$48.6%) and $j_{n\text{-propanol}}$ (800 mA cm^{-2}).

3.5. Modification with organic molecules

Modifying the catalyst surface using small molecules contributes to significant improvement in the $CO_2RR/CORR$ performance (Fig. 6a and b).[299–301] Apart from alternating the oxidation state of surface copper,[140,234,302] molecules such as sodium citrate, AEI,[303] TBA$^+$, toluene, hexanethiol,[304] *n*-butylamine, PVDF, fluoric polymer, and hexaethynylbenzene modulate the reaction microenvironment for C_{2+} species production. Among which, toluene with long-chain alkyl helps increase the catalyst stability, block the water transport, and build a hydrophobic interface to inhibit cathode corrosion.[49] The toluene-modified Cu nanosheets presented maximum $FE_{C_{2+}}$ (78%), $j_{C_{2+}}$ (1.81 A cm^{-2}), and cathodic $EE_{C_{2+}}$ (42%), as well as a 400-h stability, substantially superior to those of pristine or stearic-acid-modified Cu. Adding a PVDF binder to catalyst ink can enhance the interfacial *CO/*H coverage to alternate the alcohol/alkene ratio from 0.69 to 1.35 with notable 37.5% $FE_{alcohol}$ at 800 mA cm^{-2}.[305] Fluoric polymers limit the water wettability,[306] increase the *CO coverage, and decrease the *COCOH formation energy induced by the electron withdrawing –CF$_3$, thereby contributing to remarkable $j_{C_{2+}}$ (355.4 mA cm^{-2}) and high $FE_{C_{2+}}$ (71.08%). Hexaethynylbenzene organic layers reduce the coordinated K·H_2O coverage and enhance the CO intermediate interaction with surface, thus facilitating efficient C–C coupling and enhancing the C_{2+} yield.[307]

The rate-determining step (RDS) of the CO-to-acetate conversion can be alternated by thiols with optimal alkyl chains (C_{18} and C_{12}).[309] The nucleophilic S-intermediate interaction facilitated the RDS (CO* to CHO*) by increasing the $CO_{(ad)}$ sp^2 hybridization. The ligands stabilized the HOOC–CH_2* intermediate, thus directing the CORR to acetate. Another interesting example focuses on Ag crystal-triazole with dynamically reversible transformation between adsorbed triazole and adsorbed triazolyl on Ag(111) during the CO_2RR,[310] included by the strong metal–ligand conjugation, presented a 98% FE_{CO} with 802.5 mA cm^{-2} j_{CO}. The dynamic metal–ligand coordination promotes CO_2 protonation and branches this rate-determining step to the C–OH breakage in adsorbed COOH.

This journal is © The Royal Society of Chemistry 2025

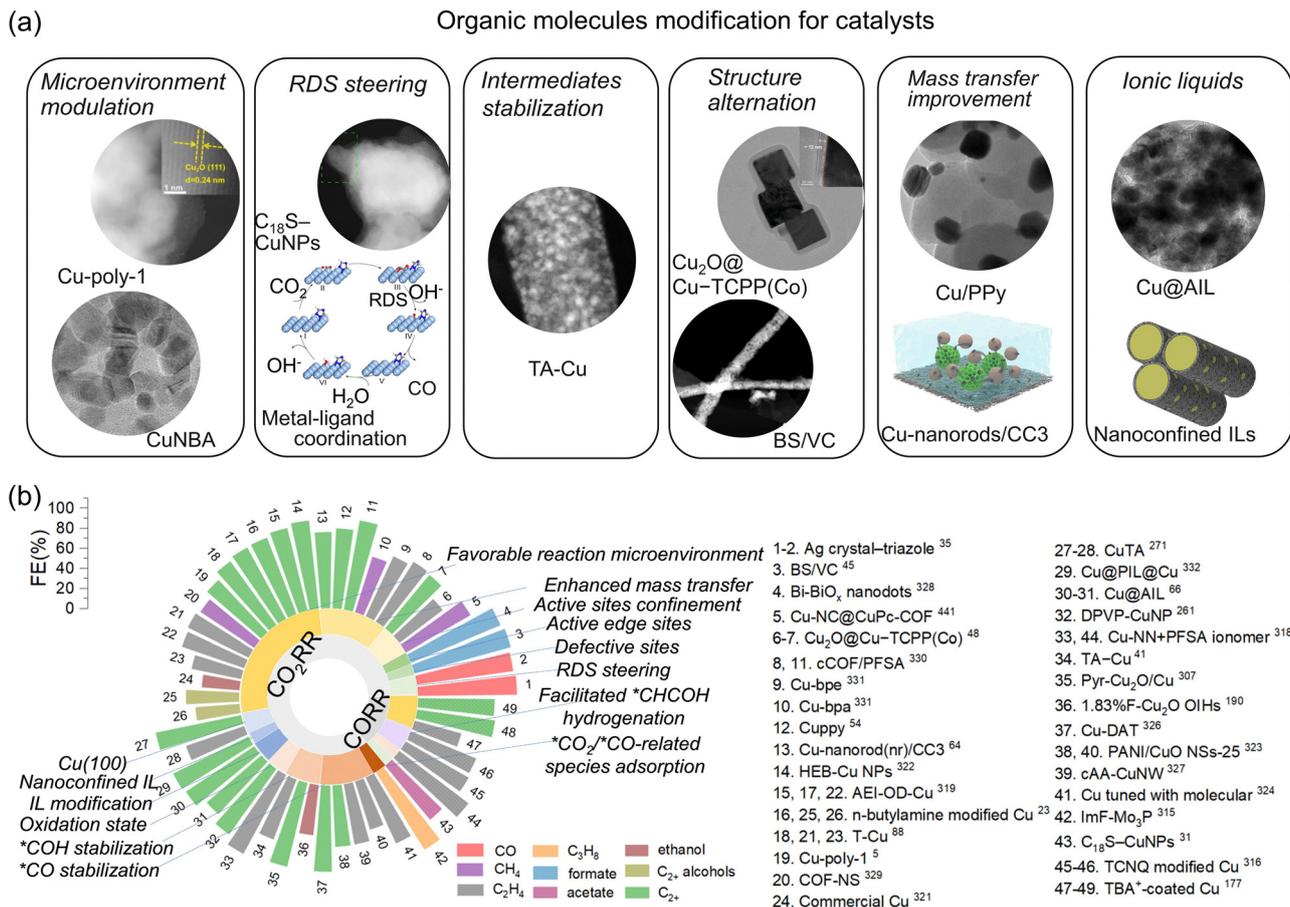Chem. Soc. Rev., 2025, **54**, 6973–7016 | **6989**

Fig. 6 Organic molecule modified catalysts. (a) Summary of the organic molecule modifications for catalysts. (Cu-poly-1, reproduced with permission.[306] Copyright 2024, Elsevier. Cu-NBA, reproduced with permission.[308] 2024, John Wiley and Sons. C₁₈S−CuNPs, reproduced with permission.[309] Copyright 2024, Springer Nature. Metal−ligand coordination, reproduced with permission.[310] Copyright 2023, American Chemical Society. TA-Cu, reproduced with permission.[311] Copyright 2023, John Wiley and Sons. BS/VC, reproduced with permission.[312] Copyright 2023, Springer Nature. Cu₂O@Cu−TCPP(Co), reproduced with permission.[313] Copyright 2024, John Wiley and Sons. Cu/PPy, reproduced with permission.[314] Copyright 2025, Royal Society of Chemistry. Cu-nanorod/CC₃, reproduced with permission.[143] Copyright 2022, John Wiley and Sons. Cu@AIL, reproduced with permission.[139] Copyright 2023, American Chemical Society.) (b) Summary of the reported FE by organic molecule modification (data from Tables S1 and S2, ESI†).

The organic molecule coating layer, such as polyaniline,[315] *N*-aryl-substituted tetrahydro-bipyridine and a related oligomeric film,[316] and poly(2-aminoazulene)[317] can stabilize the key intermediate *CO and enrich the *CO intermediates on active Cu sites, thus facilitating C–C coupling to C₂₊ species. Meanwhile *CHO stabilized by hydrogen bonding can be achieved by N–H-rich molecules (3,5-diamino-1,2,4-triazole (DAT)), pyroglutamic acid (Pyr), tannic acid, Vitamin C, and C₈F₁₈. Among which, DAT steers the CO₂RR selectivity from C₂₊ in acid to C₁.[318] The Pyr modified Cu⁺ sites are reconstruction-resistant,[291] while the unmodified regions transformed into Cu, creating stable Cu⁺/Cu⁰ interfaces to lower the C–C coupling energy barrier. Similar effects are obtained by tannic acid but with the hydroxyl species in molecules to stabilize Cu$^{\delta+}$ towards ethylene.[311] The modified Cu presented excellent FE$_{C_2H_4}$ (63.6%) and $j_{C_2H_4}$ (497.2 mA cm⁻²) in a flow cell. Vitamin C affords strong hydrogen bonding to afford favorable electron and proton transfer for *CO formation and dimerization for ethylene

production,[319] achieving 60.7% FE$_{C_2H_4}$ and 539 mA cm⁻² $j_{C_2H_4}$. The 1-ethyl-3-methylimidazolium modification[299] improved the adsorption of multi-site *CO₂/*CO-related intermediates on Mo sites, leading to C₃H₈ production at $j_{C_3H_8}$ 395 mA cm⁻² with an FE$_{C_3H_8}$ of 91% at −0.8 V *vs.* RHE.

Engineering the catalyst with organic molecules leads to structure modulation, such as defects, edge sites, and facets. By introducing an antioxidant passivation layer (oxyphilic ascorbic acid vitamin C, VC) to prevent the defective Bi sites from OH⁻ poisoning,[312] the modified Bi₂S₃ (BS) nanowires exhibited ultrastability of 120 h for CO₂-to-formate conversion and high formate production at ampere current density. This excellent performance originates from the VC molecules which isolate OH⁻ and defective Bi sites, while the VC layer traps OH⁻ to stabilize the defective sites. The poly(methacrylic acid) ligand *in situ* transformed into a carbon shell under CO₂RR conditions to confine and limit the Bi–BiOₓ nanodots growth,[320] preserving abundant active edge sites for formate production.

6990 | *Chem. Soc. Rev.*, 2025, **54**, 6973–7016

This journal is © The Royal Society of Chemistry 2025

Besides, the carboxyl group in a ligand maintained on nanodots works as oxygen donors to Bi–BiO$_x$, responsible for formate selectivity at high reaction rates up to 1 A cm^{-2}. Similar confinement effects and seeding-growth manipulation can be achieved by the MOF overlayer to encapsulate Cu$_2$O preserving the valence state and crystalline (200) for *CO–*COH coupling,[313] and leveraging the synchronous leaching of ligand tannic acid during CO$_2$RR reconstruction and exposing favorable (100) facets to enrich *CO and facilitate *CO dimerization.[251]

Mass transfer can be alternated by porous organic cages,[143] and 2D sulfonated COF nanosheet based ionomers.[321] They promoted CO$_2$ transfer, accumulated CO$_2$ and K$^+$ near the catalyst surface, enhanced *CO coverage, and facilitated H$_2$O dissociation, and incorporating an oppositely charged anionic ionomer (perfluorinated sulfonic acid, PFSA) into a cationic COF on a Cu surface to release the hidden positive charge within the COF[322] facilitated gas transfer and enhanced K$^+$ immobilization which impede both outward and inward migration of generated OH$^-$ and cations. Meanwhile a local proton-transport promoter,[314] developed by hybridizing Cu catalytic sites with proton hopping sites from dual-conductive polypyrrole, modifies the Cu surface for extraordinary CO$_2$-to-C$_{2+}$ performance (FE$_{C_{2+}}$ 80.0% at 700 mA cm^{-2}). Where the protons transfer *via* the Grotthuss mechanism, and proton conductivity is up to the formation and breakage of the hydrogen bond ("–HN^1···H N^{2}H–" to "–HN^1 H···N^{2}H–") at the hopping site. The proton availability can also be controlled by tuning molecule electrophilicity on Cu to steer the CO$_2$RR selectivity.[323] 1,2-Bis(4-pyridyl)ethane with low electrophilicity promotes proton transfer towards *CO hydrogenation and further to CH$_4$ (58.2% FE$_{CH_4}$), while trans-1,2-bis(4-pyridyl)ethylene with high electrophilicity exhibits stronger hydrogen binding to stabilize *CO and further dimerization into C$_2$H$_4$ with 65.9% FE.

Alkaline ionic liquids on Cu play multiple roles of a CO$_2$ concentrator,[139] an adsorbed CO$_2$ activator, an intermediate stabilizer, and a CO dimerization promoter for C$_{2+}$ production. High FE$_{C_{2+}}$ (81.4%) at 900 mA cm^{-2} and 47.4% half-cell EE at −0.76 V vs. RHE are achieved, as well as 71.6% FE$_{C_{2+}}$ at 1.8 A cm^{-2}. Poly(ionic liquids) (PILs) can be confined into Cu for acidic CO$_2$RR performance (83.1% FE$_{C_{2+}}$ at −700 mA cm^{-2}, 37.6% EE$_{C_{2+}}$),[324] due to the abundant semi-rigid porous structure and dense cationic–anionic network to afford a moderate local alkaline microenvironment and enrich K$^+$ at the active sites. Regulating the functionality and morphology of PILs directs the CO$_2$RR pathway *via* different C–C coupling at high reaction rates, while the PIL adlayer on the Cu surface boosts the CO$_2$-to-C$_{2+}$ conversion at ampere-level current density and low K$^+$ concentration (1 M),[138] delivering 82.2% and 75.8% FE$_{C_{2+}}$ at 1 and 1.5 A cm^{-2}, respectively. This excellent performance originated from the PIL layer for inhibited proton diffusion to the catalyst surface, enriched K$^+$, and facilitated C–C coupling. Hydrophobic ionic liquid (HIL) modification on oxide derived Cu also demonstrated prominent C$_{2+}$ production with 85.1% FE$_{C_{2+}}$ at 800 mA cm^{-2}, maximum $j_{C_{2+}}$ of 779 mA cm^{-2}, and an impressive formation rate (2512 μmol h^{-1} cm^{-2}),[96] attributed to the formation of the most stable adsorption site and CO$_{atop}$ dimerization, increased *CO coverage, and enlarged electrochemical surface charge by the HIL, thus promoting the CO$_2$RR.

3.6. Tandem catalyst design

Tandem CO$_2$ reduction, with integration of cascade CO$_2$-to-CO and CO-to-C$_{2+}$ in series on two distinct but complementary catalysts, is effective in circumventing the linear scaling relationship limitations, improves the *CO coverage for C–C coupling, thus enhancing C$_{2+}$ species production.[325,326] Tandem CO$_2$ reduction enables high current density operation. Besides, tandem catalysts, compared to traditional catalysts, are more thermodynamically and kinetically favorable, which enhanced the catalytic efficiency. Cu-based tandem catalysts contributed to improved FE and current density for the CO$_2$RR by optimizing the reduction pathway. Additionally, changes in local environments (intensified active sites, enriched local CO, retained pH, and led to synergistic effects of different elements in a tandem system) also improve the CO$_2$-to-C$_{2+}$ conversion.

The keys of catalysts/electrodes design for tandem CO$_2$ reduction should confirm efficient CO transport, balance the CO production and utilization, and match the overpotential of CO generation and C$_{2+}$ production. Ag, Au and Zn were introduced to Cu and formed a tandem catalyst, which facilitates CO$_2$-to-CO conversion, enriches CO on the Cu surface and promotes C–C coupling. Due to the high activity in CO generation, Ag is mostly used as a component in tandem catalysts from economic perspective, although its CO selectivity is lower than Au selectivity. Three kinds of Ag–Cu Janus nanostructures with (100) facets (JNS-100) are highly selective to CO$_2$-to-C$_{2+}$ conversion (Fig. 7a),[327] especially, Ag$_{65}$–Cu$_{35}$ JNS-100 produced 54% FE$_{C_2H_4}$ and 72% FE$_{C_{2+}}$, attributed to its suitable electronic structure by the optimal Ag/Cu ratio and the tandem effect by CO spillover (Fig. 7b). The tandem electrode of sputtered Ag nanoparticle layers on hydrophobic polytetrafluoroethylene (PTFE) and N-doped carbon(NC)-modified Cu nanowire arrays exhibits a hierarchical configuration,[98] where CO is generated on the Ag layer and spills over and transports to the NC-modified Cu layer, and the Cu/NC interfaces are responsible for *CO trapping and adsorption (Fig. 7c). The optimal electrode exhibited 53.5% FE$_{C_2H_4}$ and 87.5% FE$_{C_{2+}}$ at 519.0 mA cm^{-2}, respectively, as well as a high C$_{2+}$/C$_1$ ratio of 10.42 and 50-h stability. The segmented Cu/Ag s-GDE tandem catalyst also achieved well management of *CO by the Ag layer, increased CO utilization and $j_{C_{2+}}$.[135] Similar to Ag, Au attracts much interest for its high CO selectivity, which weakens CO$_2$ bonds and boosts the CO intermediate formation. Bimetallic CuAu tandem catalysts have exhibited excellent CO$_2$RR performance with Au and Cu facilitating CO production and subsequent C–C coupling, respectively. For example, the deposited Au nanoparticles on Cu foil enhanced the CO concentration on Cu and facilitated C–C coupling,[328] while the Au@Cu core–shell with different Cu shell thicknesses only produced hydrocarbons or formate,[329] indicating the effects of arrangements of the catalyst components on CO$_2$RR products. It is quite challenging to retain highly active tandem sites due to the potentiodynamic structural evolution, to mediate this issue, self-reducing ions (iodate) that leverage the dissolved iodate self-reduction were deployed to achieve directional reconstruction of the tandem catalyst.[136] The CuO/AgIO$_3$ tandem catalyst presents rapid

This journal is © The Royal Society of Chemistry 2025

Chem. Soc. Rev., 2025, **54**, 6973–7016 | **6991**
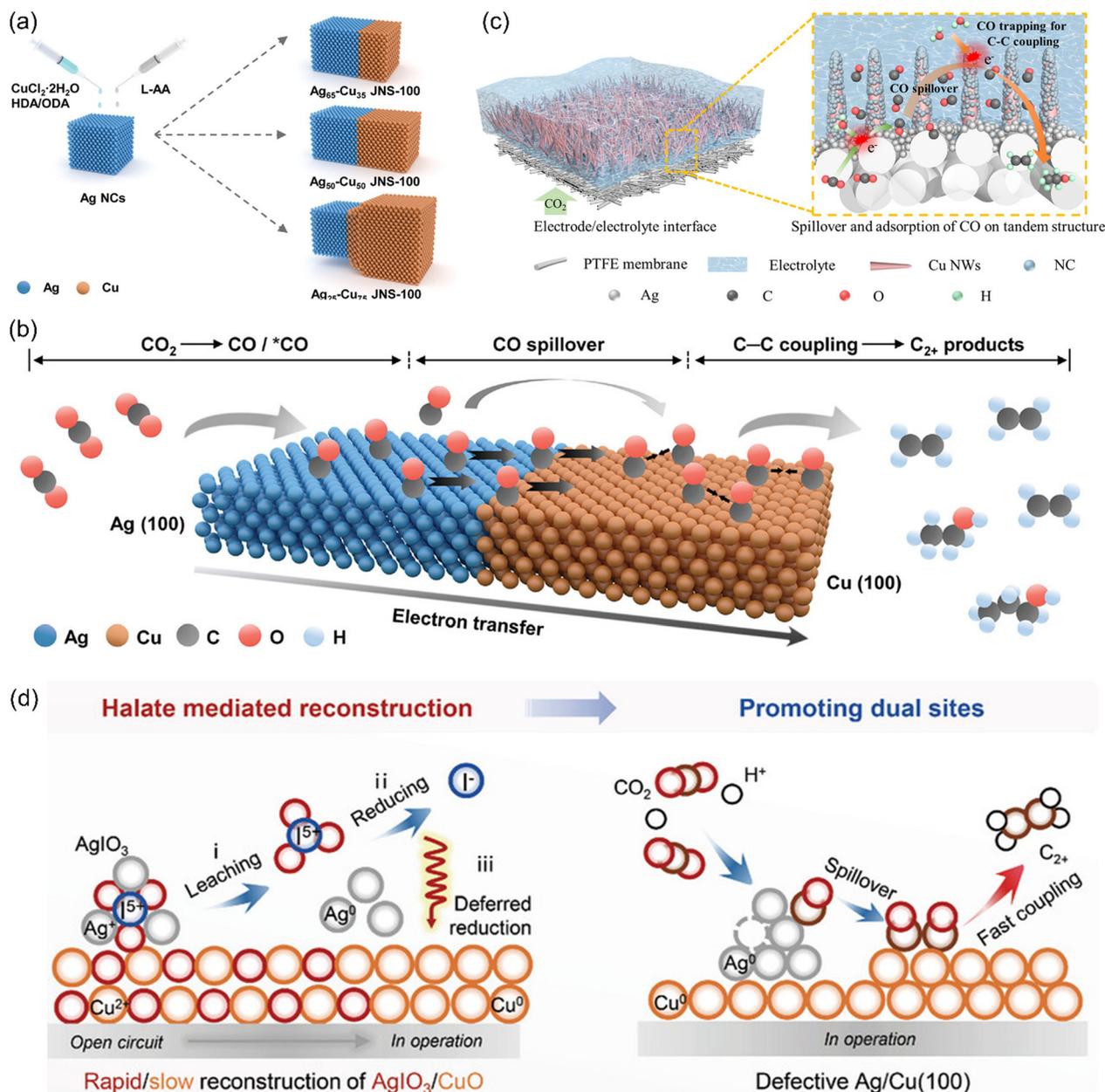
Fig. 7 Tandem catalyst design. (a) Summary of the organic molecule modifications for catalysts. Schematic illustration of the synthesis of three kinds of Ag–Cu JNS-100 *via* confined growth of Cu on one of the six equal faces of Ag NCs. (b) Schematic illustration of a plausible CO_2RR mechanism on Ag_{65}–Cu_{35} JNS-100. Reproduced with permission.[327] Copyright 2022, John Wiley and Sons. (c) Schematic illustration of the PTFE-based tandem electrocatalysis for CO_2 reduction in a flow-cell system. Reproduced with permission.[98] Copyright 2025, American Chemical Society. (d) Schematic illustration of directing reconstruction of the $CuO/AgIO_3$ tandem catalyst in the acidic CO_2RR reaction. Reproduced with permission.[136] Copyright 2024, John Wiley and Sons.

iodate ion dissolution during the CO_2RR to generate defective Ag. The dissolved iodate self-reduction drags the CuO reconstruction rate and directs transformation into Cu(100) (Fig. 7d). The defective Ag with asymmetric charge distribution promotes *COOH formation and enriches local CO for C–C coupling on Cu(100). Therefore, the reconstructed tandem catalyst demonstrates 82% $FE_{C_{2+}}$ at 1.2 A cm^{-2} and maximum $j_{C_{2+}}$ (1024 mA cm^{-2}) in strong acid.

Although bimetallic tandem systems of Cu and other metals (Ag, Au) have been extensively studied, these catalysts suffer

from the changes in the composition and morphology during the $CO_2RR/CORR$ process, altering their physical and electronic properties and further complicating the understanding of the catalytic mechanism and dragging the catalyst development. In this regard, significant efforts have been devoted to designing tandem catalysts that use CO-selective molecular catalysts[330] and SACs.[331] For example, coupling CoPc on Cu GDE enabled high *CO coverage and enriched *CO_{top}, reducing the energy barrier for OCCO formation.[332] This tandem catalyst gave a 1.8-time higher $FE_{C_{2+}}$ (82% $FE_{C_{2+}}$ at 480 mA cm^{-2}) than the Cu GDE.

6992 | *Chem. Soc. Rev.*, 2025, **54**, 6973–7016

This journal is © The Royal Society of Chemistry 2025

Similarly, the tandem catalyst consisting of CuO and Ni SACs exhibited superior $FE_{C_{2+}}$ (81.4%), $FE_{C_2H_4}$ (54.1%) and significantly high $j_{C_{2+}}$ (1220.8 mA cm^{-2}),[51] attributed to the unique co-loaded nanostructures which realizes the vicinity of the two catalyst units. The developed tandem catalyst not only achieves efficient cascade CO_2–CO–C_{2+} conversion, but also integrates the merits of Ni SAC which in situ produced CO and its fast consumption, guiding the way of tandem catalysts for large-scale synthesis of C_{2+}. Moreover, the CO-producing Fe–N–C SAC layer segment locates at the inlet to prolong the CO residence time in the C_{2+}-selective Cu catalyst layer,[135] contributing to 90% $FE_{C_{2+}}$ and $j_{C_{2+}}$ over 1 A cm^{-2}. Instead of working as the CO-formation catalyst, the Ni–N–C catalyst in the tandem system mainly modulates the local pH near the Cu catalyst, contributing to the maximum $FE_{C_{2+}}$ (68% ± 5%) and $j_{C_{2+}}$ (356 ± 18 mA cm^{-2}) in acid.[333]

4. Principles of mass transport manipulation for the CO₂RR/CORR at ampere-level current

Much effort has been devoted to constructing highly selective and active catalysts for decades. However, satisfactory performance was only observed at low current density due to the increased mass transfer of reactants and products at higher current. Although high $CO_2RR/CORR$ selectivity based on micro-design of catalysts modulates the active sites' amount for the target product, the industrial-level CO_2/CO electrolysis focuses more on mass transfer promotion. Engineering the electrode and electrolyzer presents an important principle to facilitate efficient mass transport for improving $CO_2RR/CORR$ at ampere current.[334] Significant progress has been achieved in developing novel electrodes and optimizing electrolysis systems. In this section, principles of mass transport manipulation by electrode/electrolyzer engineering will be discussed.

4.1. Electrode engineering

4.1.1. Porous micro-structured GDEs.
Beyond the efficient active sites, fast mass transfer is also crucial for catalyst/electrode design for the $CO_2RR/CORR$, which can be achieved via porous GDE design to expose abundant active sites (Fig. 8a and b). To overcome the slow CO_2 diffusion in acid, the GDE structure is optimized by deploying a copper-based ultrathin superhydrophobic macroporous layer,[142] where the CO_2 transfer is significantly enhanced and high $FE_{C_{2+}}$ (87%) with 1.6 A cm^{-2} $j_{C_{2+}}$ was achieved.

Enhanced charge transfer and intrinsic catalytic activity can be facilitated by using conductive substrates such as carbon nanotubes.[222,338] Derived from the hierarchically structured Ni-imidazolate coordination polymer,[222] the hierarchical nanostructured Ni-SACs exhibited flower-like micro-structures assembled from nanoribbons, which converted into hierarchical nanocomposites after introducing the multi-functional substrate CNTs. The substrate helps to establish nanostructured N-doped carbon with large surface pores for fast etchant diffusion to remove Ni NPs, while the high-density Ni single atom

sites within the hierarchical structures have facile access to CO_2, thereby maximizing the active site utilization at ultra-high current densities.

To reveal the mass transfer-performance relationship, our group[242] designed a Fe SAC with a highly ordered porous structure involving hierarchical micropores, mesopores, and macropores, which effectively facilitates mass transfer to Fe atom sites, thus contributing to excellent CO_2RR performance. The large mesopores afford strong CO_2 diffusion ability inside the porous structured catalyst, constructing a favorable CO_2 concentrated environment for CO production. Applying porous or 3D supports facilitates smooth CO_2 transfer, such as an interconnected mesoporous carbon nanofiber and carbon nanosheet network (IPCF@CS),[339] the hollow Br/N co-doped carbon nanocages,[335] and the unique house-of-cards structured scaffolds derived from MgAl LDH,[39] hierarchical supports,[223] mesoporous carbon,[340] poriferous 3D frameworks,[113] and 3D interconnected ligament-channel networks.[341] Among these, the IPCF@CS structure exhibited highly mesoporous IPCF to hinder CS stacking, affording additional completely exposed sites and abundant bicontinuous mesochannels of IPCF to ensure efficient CO_2 transfer. The unique configuration maximized the utilization of active sites and enriched the local CO_2 concentration.

Nanoscale management of CO transport for CO_2-to-C_{2+} conversion can be achieved via a 3D tandem catalyst electrode design such as anchoring CO-formation Ag NPs on Cu nanoneedles.[336] This configuration was effective in prolonging the CO diffusion path length to enhance CO utilization, thus leading to 70% $FE_{C_{2+}}$ and 350 mA cm^{-2} $j_{C_{2+}}$ in a flow cell.

An efficient formate-selective Bi catalyst-GDE, hierarchical Bi (HS2-Bi), was constructed,[337] characteristic of a hierarchical nanostructure with an amorphous shell and a high-curvature. The amorphous layer (8–15 nm) not only boosted the kinetics for CO_2 adsorption/activation and reduced the formation energy barrier for *OCHO, but also improved the electric-thermal field and K$^+$ adsorption, hence accelerating CO_2 reduction to formate. As a result, maximum $j_{formate}$ (677.7 mA cm^{-2}) and over 94% formate selectivity were achieved by HS2-Bi, significantly outperforming the hierarchical structured sample without the amorphous layer. Similar K$^+$ enrichment has been demonstrated by the carbon coated tip-like In_2O_3 for efficient CO_2-to-HCOOH conversion.[342]

Hollow fiber penetration electrodes (HFPEs) featuring oriented mass transfer, favorable triple phase formation, and facilitated desorption of adsorbed species contributed to CO_2/CO electrolysis at ultra-high reaction rates over 1 A cm^{-2}, such as the Ag-HFPE[145–147] and Zn HPE[343] for CO_2-to-CO conversion, Bi HFPEs,[37,344] SnO_2@Ni HF,[345] chlorine-doped SnO_2 nanoflowers on 3D Ni HFPEs[346] for CO_2-to-formate conversion, La(OH)$_3$@Cu HPE for CO_2-to-ethanol,[347] Cu HFPEs for CO_2-to-C_{2+} conversion[36,148,348,349] and CO-to-C_{2+} conversion,[40,146] respectively. Especially, the hierarchical micro/nanostructured Ag hollow fiber exhibited 90.3% FE_{CO} with 3.2 A cm^{-2} j_{CO}.[146] By optimizing the K$^+$/H$^+$ concentration and CO_2 flow rate, the tensile-strained Cu nanosheet layer-coated Cu HPE exhibited 84.5% $FE_{C_{2+}}$, 3.1 A cm^{-2} $j_{C_{2+}}$, and 240-h ultrastability in acid.[148]

This journal is © The Royal Society of Chemistry 2025
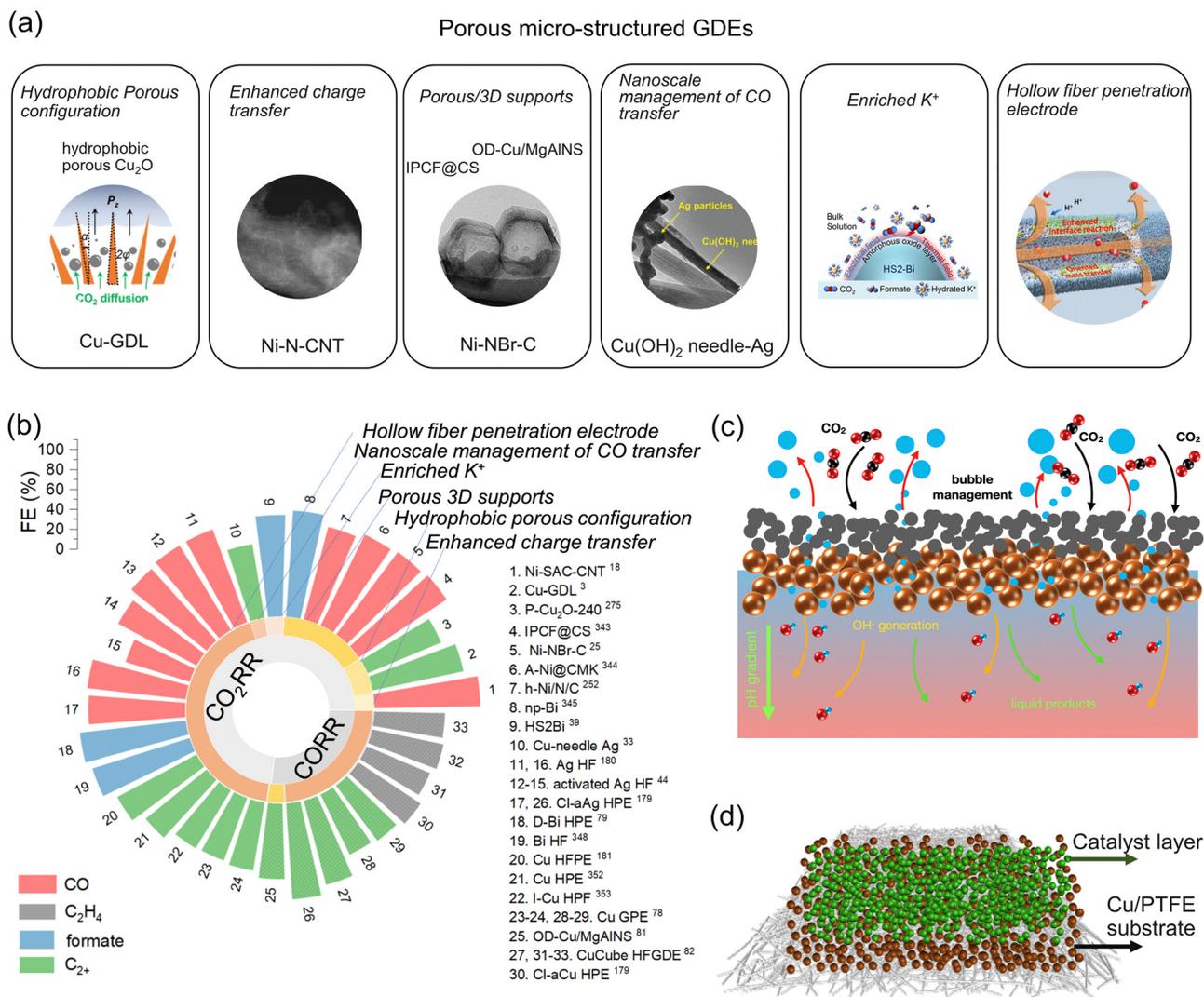
Chem. Soc. Rev., 2025, 54, 6973–7016 | 6993

Fig. 8 Porous micro-structured GDEs. (a) Summary of porous micro-structured GDEs. (Cu-GDL, reproduced with permission.[142] Copyright 2024, Springer Nature. Ni-N-CNT, reproduced with permission.[222] Copyright 2021, Elsevier. Ni-NBr-C, reproduced with permission.[335] Copyright 2024, John Wiley and Sons. Cu(OH)$_2$ needle-Ag, reproduced with permission.[336] Copyright 2023, John Wiley and Sons. K$^+$ enrichment, reproduced with permission.[337] Copyright 2024, Journal of Energy Chemistry. HFPE, reproduced with permission.[145] Copyright 2022, Springer Nature.) (b) Summary of the reported FE for CO$_2$RR/CORR products by micro-structured GDEs. (data from Tables S1 and S2, ESI†) (c) illustration of the electrode–electrolyte interface on GDL. Reproduced with permission.[256] Copyright 2018, John Wiley and Sons.

Different from the above mentioned GDL-based GDE (Fig. 8c) and HFPE, hydrophobic PTFE with sputtered Cu (Cu/PTFE) has also been used to support catalysts for CO$_2$RR/CORR (Fig. 8d), due to the construction of a favorable hydrophobic microenvironment and robust interface against flooding at high current densities. Assisted by Cu/PTFE,[350] the Pd-modified GDE exhibited a high FE$_{C_{2+}}$ (89 ± 4%) and single-pass carbon efficiency (SPCE, 60 ± 2%) at 500 mA cm^{-2} in acid. Some other Cu/PTFE based GDEs also demonstrated their potential for industrial-scale CO$_2$/CO electrolysis.[12,187,351–356]

4.1.2. GDEs with controllable thickness and porosity. Tailoring the thickness of the catalyst layer (CL) promotes the transfer of CO$_2$ and the electrolyte simultaneously to reach the catalyst surface and further participate in the CO$_2$RR.[250] The electrolyte submerges the catalyst easily when the catalyst layer is too thin, making it challenging for gas to enter, while the too thick catalyst layer blocks gas penetration to the catalyst. Therefore, modulating the proper CL thickness helps to construct a balanced gas–liquid diffusion electrode for efficient mass transfer. For instance, the CuONPs-1.7/GDE with 1.7 mg cm^{-2} catalyst loading, compared to CuNPs-0.34/GDE and CuONPs-3.1/GDE, exhibited proper three-phase interface thickness,[153] thus contributing to a record $j_{C_{2+}}$ (1.7 A cm^{-2}) in neutral electrolytes. Besides, FE$_{C_{2+}}$ increased with higher total current density below 2 A cm^{-2} with a maximum value of 76% at 1.6 A cm^{-2}. Similar CL thickness effects have been demonstrated by controlling the MOF thickness to encapsulate copper oxides for CO$_2$-to-C$_2$H$_4$ conversion,[313] and the ≈12 nm one exhibited a maximal FE$_{C_2H_4}$ of 54 ± 2% at 500 mA cm^{-2}.

6994 | *Chem. Soc. Rev.*, 2025, **54**, 6973–7016

This journal is © The Royal Society of Chemistry 2025

Alternating the porosity and thickness of the microporous layer (MPL) in GDEs is one of the major principles to control the mass transport for CO-to-acetate conversion. Our group optimized the GDE configuration to maximize the CO transfer through GDLs to the catalyst surface and further reduction at the solid–liquid–gas triple phase boundary.[1] By depositing different carbon black (CB) loadings of 1, 2, and 3 mg cm^{-2} into MPL, the 2 mg cm^{-2} CB exhibits the best activity and selectivity to acetate production, attributed to its suitable porosity and thickness, with optimal porosity and thickness favoring efficient mass transfer to boost the CORR. In addition, the 2 mg cm^{-2} CB affords a strong support for the catalyst layer, confirmed by the low penetration of the catalyst layer within the GDL but good penetration within the MPL.

Regulating the pore size distribution of the MPL and the hydrophobicity of carbon fiber substrates (CFSs) has also been confirmed as effective in promoting the mass transfer of electron transfer, CO_2, and water,[357] thus favoring the C_{2+} production. The hydrophobicity modification is effective in regulating the local CO_2 concentration and *H coverage by controlling the thickness of the localized water layer between the MPL and CL, which contributes to enhanced current density and ethylene selectivity. The optimal Cu-based GDEs presented respective 10% and 30% PTFE in CFS and MPL, and numerous 30–150 nm pores, contributing to $j_{ethylene}$ (697 mA cm^{-2}), $j_{C_{2+}}$ (885 mA cm^{-2}), and j_{total} (1.36 A cm^{-2}) at −1.44 V vs. RHE.

4.1.3. Molecule/polymer engineered GDEs. Engineering the electrode–electrolyte interface for fast mass transport benefits the CO_2RR at ultrahigh current density (Fig. 9a and b). Improved cation transfer has been demonstrated by ion-polymer[358] and cation-augmenting layer (CAL)[12] modification. The ion-polymer-modified GDE was designed to improve the proton transfer during CO_2 electrolysis.[358] GDE-cationic Nafion outperformed that with non-ionic PTFE and anionic FAA in multicarbon production, exhibiting a remarkable $FE_{C_{2+}}$ of 75.2% at 1.16 A cm^{-2}. Nafion affords proton shuttle $–SO_3^-$ to react with the local proton donors of H_3O^+ and HCO_3^-, with the latter donor working as a proton pool near the reaction environment to break the diffusion limit. The CAL, namely the cationic perfluorosulfonic acid (PFSA) ionomer with tetrafluoroethylene and sulfonyl fluoride vinyl ether,[12] affords efficient cation (H^+ and K^+) transfer from the electrolyte to catalyst surface and meanwhile reducing OH^- diffusion out, which results in higher surface pH to promote C–C coupling. The acidic–SO_3H group in the polymer tends to exchange K^+ from the bulk electrolyte with its protons, maintaining highly concentrated K^+ at the catalyst surface, which further improves CO_2 activation for efficient CO_2 reduction in acid. The CAL-modified Cu, compared to bare Cu, exhibited higher $FE_{C_2H_4}$ (13%) but much lower FE_{CH_4} (<1%) at 400 mA cm^{-2}, due to the electrostatic interactions between cation species (K^+) and the electric dipole of specific adsorbates.

Wettability control for a favorable CO_2RR/CORR microenvironment can be achieved by applying PT coating,[46] alkanethiols,[360] polymer binders,[361] and PTFE NPs.[248] The thin PT coatings on Cu GDEs alternate the local H_2O/CO_2 concentrations,[46] attributed to its hydrophobicity, low water-uptake ability, high porosity and gas permeability for efficient mass transfer. As a result, the modified GDEs presented a high $FE_{C_{2+}}$ (>87%) at 2 A cm^{-2}, $EE_{cathode}$ over 50% because of the substantially reduced cathodic potential, and long-term stability (>150 h at 200 mA cm^{-2}, 10 h at 1 A cm^{-2}) due to the robust reaction interface. Meanwhile the alkanethiol coatings with different alkyl chain lengths can block water absorption and facilitate CO_2 transfer,[360] thus alternating the H_2O/CO_2 transfer to modulate the local H_2O/CO_2 concentrations. The optimal equilibrium of kinetic-controlled *CO/*H affects the CO_2RR to ethylene and ethanol pathways. By changing the hydrophilic interface to superhydrophobic one, there exists limitations of insufficient supply of *CO to that of *H. The ethanol to ethylene ratio is alternated from 0.9 to 1.92 with remarkable $FE_{ethanol}$ (53.7%) and $FE_{C_{2+}}$ (86.1%), respectively. Additionally, a multifunctional conductive polymer, polyaniline modified by p-aminobenzenesulfonic acid (ABSA-PANI),[362] was deployed to construct an ideal microenvironment for CO_2-to-C_{2+} conversion and meanwhile improving the charge transfer and ion transport of $K^+/H^+/OH^-$. Therefore, the CO_2RR kinetics was boosted in acids, giving 81% $FE_{C_{2+}}$ at 600 mA cm^{-2}. The conductive ABSA-PANI decreased the electrode ohmic resistance, resulting in low overpotential and enhanced cathode energy efficiency.

Introducing polymer binders plays crucial roles in facilitating CO_2 mass transfer and meanwhile mitigating the competitive HER. Different hydrophilic polymers (polyacrylic acid (PAA), Nafion, and fluorinated ethylene propylene (FEP)) as binders are deployed for Cu to modulate the CO_2 accessibility relative to H_2O at the catalyst vicinity.[361] FEP with hydrophobic (aerophilic) properties prefers to decrease the local H_2O concentration and enrich the reactant (CO_2) and intermediate (CO) concentration, while the PAA binder renders a highly hydrophilic electrode surface, which hinders CO_2 access to the catalyst surface. High $FE_{C_{2+}}$ ($\approx$77%) and $j_{C_{2+}}$ (>600 mA cm^{-2}) at −0.76 V vs. RHE are obtained. Directly introducing hydrophobic PTFE NPs into the Bi-based catalyst layer (CL) can also tune the microenvironment for enhanced CO_2 electrolysis.[248] A moderate hydrophobicity facilitates the balance between the CO_2 gas and the liquid electrolyte inside the CL (Fig. 9c), accelerating CO_2 mass transfer by reducing the diffusion layer thickness. Therefore, the PTFE modified GDE approached high $j_{acetate}$ (677 mA cm^{-2}) and 35% single-pass CO_2 conversion at −0.7 V vs. RHE.

Tailoring water and hydroxide transfer at a quasi-two-phase interface of MEA helps to boost CO-to-C_{2+} conversion. The CuO–ionomer structure assembled into a MEA helps to uncover the water/hydroxide transfer-performance relationship.[33] Attractively, a remarkable $FE_{C_{2+}}$ (>90%) and low cell voltage (2.4 V) at 1000 mA cm^{-2} are achieved by using the CuO-Nafion configuration, due to the optimized H_2O and OH^- transfers. Compared with flow cells where the CORR happens at the catalyst-CO-catholyte three-phase interface and catholyte flow excludes the possible transfer of H_2O and OH^-, MEA presents limited water supply by humidified CO and membrane crossover. When the supply and consumption of H_2O approach an equilibrium with increasing current, the cathodic reductions prefer to occur at the catalysts-CO quasi-two-phase interface with water vapor existence and the polymer membrane as a solid electrolyte. Therefore,
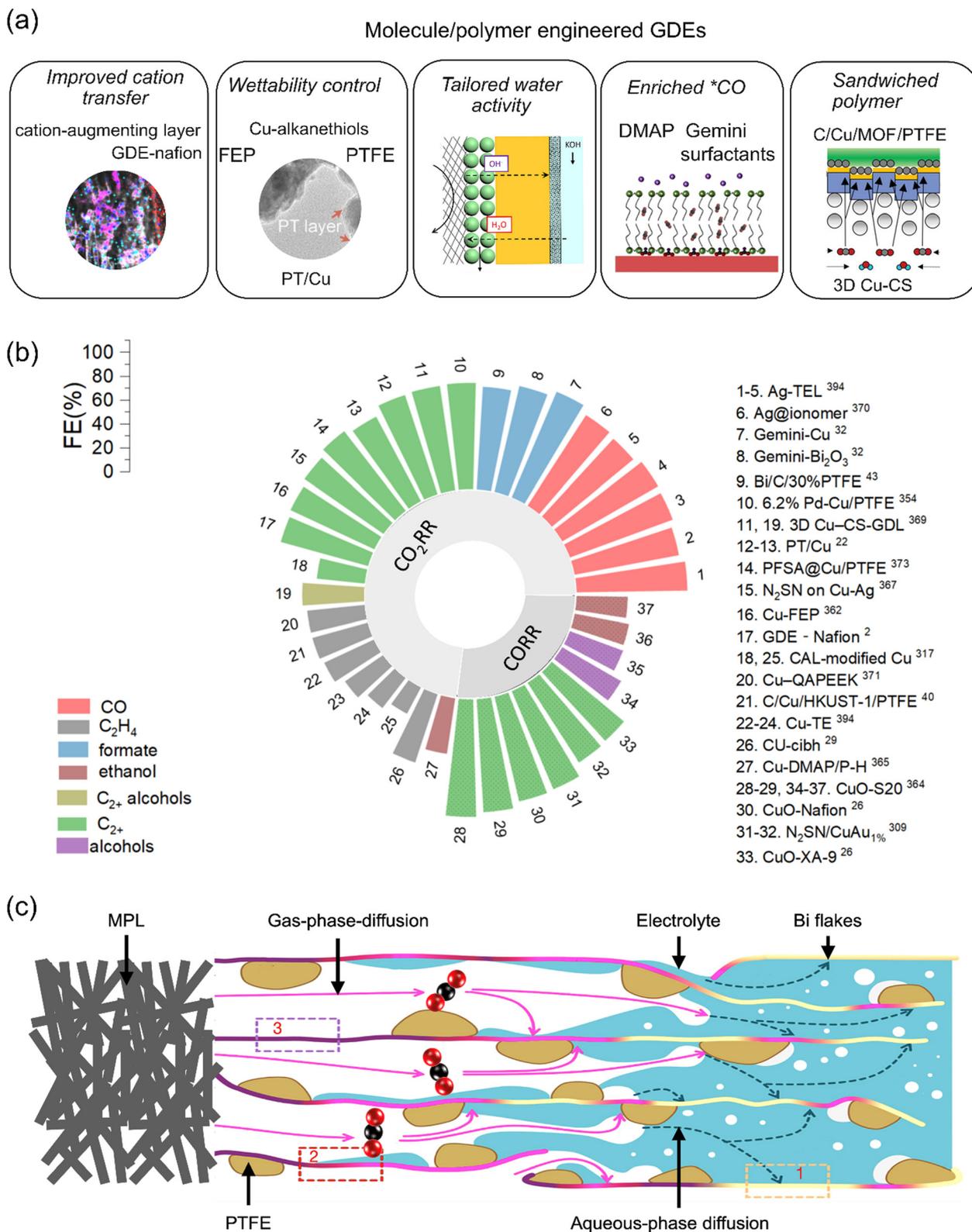
This journal is © The Royal Society of Chemistry 2025

Chem. Soc. Rev., 2025, **54**, 6973–7016 | 6995

Fig. 9 GDEs with molecule/polymer engineering. (a) Summary of molecule/polymer engineered GDEs. (GDE-Nafion, reproduced with permission.[358] Copyright 2023, John Wiley & Sons. PT/Cu, reproduced with permission.[46] Copyright 2024, Springer Nature. Tailored water and hydroxide, reproduced with permission.[33] Copyright 2023, Elsevier. Gemini surfactant, reproduced with permission.[359] Copyright 2024, John Wiley and Sons. C/Cu/MOF/PTFE, reproduced with permission.[351] Copyright 2022, John Wiley and Sons.) (b) Summary of the reported FE by molecule/polymer engineered GDEs (data from Tables S1 and S2, ESI†). (c) Schematic illustration of the CO_2 mass transport inside the catalyst layer with added PTFE, including gas–phase diffusion (solid red arrows) and aqueous–phase diffusion (dashed blue arrows). Reproduced with permission.[248] Copyright 2021, American Chemical Society.

6996 | Chem. Soc. Rev., 2025, 54, 6973–7016

This journal is © The Royal Society of Chemistry 2025

applying sufficient H_2O transport from the anolyte through the membrane to the dry cathode is vital to proton donation for CO reduction and oppositely moves the *in situ*-generated OH^-. The OH^- migration is accompanied by solvated H_2O, which leads to lower water content near the cathode, especially at high reaction rates. The interfacial water activity can be enhanced by using anion ionomers,[363] which decrease the near-electrode local concentration of K^+ (*via* Donnan exclusion), favoring ethanol production over acetate. Remarkable $FE_{ethanol}$ (42.5%) and $FE_{alcohol}$ (55.1%) at 700 mA cm^{-2} were obtained, with $j_{ethanol}$ and $j_{alcohol}$ approaching 698 and 942 mA cm^{-2} at 2000 mA cm^{-2}, respectively.

By stabilizing the key intermediates *via* the surface-intermediate interaction, cationic Gemini surfactant modification on the catalyst surface effectively boosts the CO_2RR.[359] Combination of the double quaternary ammonium cations and alkyl chains of the Gemini surfactants facilitates *CO enrichment on the surface and HCOO* stabilization and affords facile availability to CO_2, promoting CO_2 reduction. The modified Cu exhibits 96% $FE_{formate}$ and 71% energy efficiency (EE), and the modified commercial Bi_2O_3 nanosheets present a high $FE_{formate}$ up to 91% at 510 mA cm^{-2}. Similarly, 4-dimethylaminopyridine (DMAP) works as a molecular-additive to functionalize Cu GDEs for enhancing *CO on the Cu surface,[364] due to its hydrogen bonding interaction with *COOH. The *CO coverage improvement on GDEs can also be realized by applying dodecanethiol[365] and aromatic heterocycles,[293,366] due to the thiol-stabilized Cu(100) and active Cu site stabilization by the electron-withdrawing molecule, respectively, thus boosting the production of C_{2+} species, while polyethylene glycol on the Cu GDE results in Nafion relaxation,[367] which affords facile availability of active sites, enhances the *CO and *OH adsorption, and reduces the active hydrogen species, thus promoting C–C coupling and inhibiting the HER.

Sandwiched polymers contribute to high-rate CO_2/CO-to-C_{2+} conversion.[351,368] The inserted MOF-induced organic layers in GDEs with a catalyst:MOFs:hydrophobic substrate configuration enriched the local CO_2 concentration near the active Cu sites,[351] favoring ethylene production. While the sandwiched chitosan (CS) layer works as a "transition layer" between the Cu catalyst and the GDL,[368] the developed 3D Cu–CS-GDL presented a highly interconnected network to induce the 3D Cu film growth, which facilitates fast electron transfer and overcomes mass diffusion limitations during CO_2 electrolysis. As a result, 88.2% $FE_{C_{2+}}$ with 900 mA cm^{-2} current density at −0.87 V was achieved, including 51.4% $FE_{C_{2+} alcohols}$ with 462.6 mA cm^{-2} $j_{C_{2+} alcohols}$. Apart from the sandwiched polymer, a nanoconfined ionomer was deployed to develop GDEs with uniform ionomer distribution for improving the local mass transfer at the active centers,[369] boosting CO_2-to-CO conversion. This nanoconfined ionomer not only ensures the CO_2RR happening at the active sites and facilitates ion transfer within the CL, but also renders more average distributions of pores on GDEs and prevents ionomer accumulations to avoid high local mass transfer resistance. Therefore, the optimal GDE presented over 90% FE_{CO} at a wide current density range and ultrastability over 220 h.

Ionically conductive bifunctional ionomers benefit the CO_2 activation at the catalyst–electrolyte interface and promote

ethylene production while operating the pure-water fed MEA.[370] Specifically, the quaternary ammonia poly(ether ether ketone) (QAPEEK) contributed to industrial-scale $j_{ethylene}$ (420 mA cm^{-2} at 3.54 V), and j_{total} up to 1000 mA cm^{-2} at 3.73 V.

Constructing heterojunctions benefits efficient mass transfer for the CO_2RR at ampere-level current density.[371] For example, the superfine ionomer layer in the catalyst:ionomer bulk heterojunction (CIBH) architecture exhibits both hydrophobic and hydrophilic properties to extend gas and ion transport from tens of nanometers to the micrometer scale.[12] The ionomer intersperses sulfonate-lined paths for the H_2O and fluorocarbon channels for CO_2, decoupling gas, ion, and electron transport. The constructed CIBH is composed of Cu NPs blended with perfluorinated sulfonic acid, which was spray-coated on a porous PTFE/Cu/ionomer (CIPH) GDE to generate a 3D architecture with metal and ionomer percolation paths. Assisted by this CIBH, an impressive $j_{ethylene}$ (1.3 A cm^{-2}) with 45% $EE_{cathodic}$ was achieved in 7 M KOH. Another polymer/catalyst/ionomer heterojunction,[372] (perfluorosulfonic acid) PFSA@Cu/PTFE electrode, was designed by combining hydrophobic and highly charged hydrophilic domains to diminish the impurity (SO_2) mass transfer to the Cu surface and facilitate unimpeded CO_2 transport, respectively. The SO_2-tolerant electrode achieved high $FE_{C_{2+}}$ (84%), $j_{C_{2+}}$ (790 mA cm^{-2}), and $EE_{C_{2+}}$ (∼25%). The COF:PFSA heterojunction is effective in suppressing the HER and promoting CO_2-to-C_{2+} conversion in acid.[353] The imine and carbonyl-modified COF modulates the ionomer structure to generate homogeneously distributed cation-carrying and hydrophilic–hydrophobic nanochannels to confine proton transport and enrich K^+. This regulated proton flux and cation distribution constructs a favorable local environment for the CO_2RR.

4.2. Electrolyzer design and optimization

Normally, H-cells are deployed to rapidly screen the desired catalyst for CO_2RR/CORR, because of their low cost, facile assembly and operation.[30] Typically, H-cell consists of two independent cathodic and anodic chambers separated by ion-exchange membranes, using a reference electrode and an aqueous electrolyte. The disadvantages of H-cells include low CO_2/CO solubility, limited mass transfer, a restricted j_{total} (<100 mA cm^{-2}) and electrode area, which make it challenging to meet the requirements of industrial CO_2RR/CORR applications, especially at ampere-level current. These issues can be addressed by applying the GDEs with GDLs to afford gas mass transfer directly to the cathode to improve the mass transfer and reaction rates.

Flow cells with applying GDEs are widely investigated for CO_2RR/CORR at ampere-scale current (Fig. 10a). CO_2 is supplied directly to the cathode where the catholyte is circulated, leading to much faster mass diffusion and production rates than H-cells. In the anode side, the anolyte is also circulated for the oxygen evolution reaction. Circulation of electrolytes helps to balance the pH variation and attain a stable concentration. Therefore, flow cells contribute to better electrochemical performance than H-cells, due to the enhanced CO_2 transfer, suppressed HER, and the constructed local gas–electrolyte–catalyst
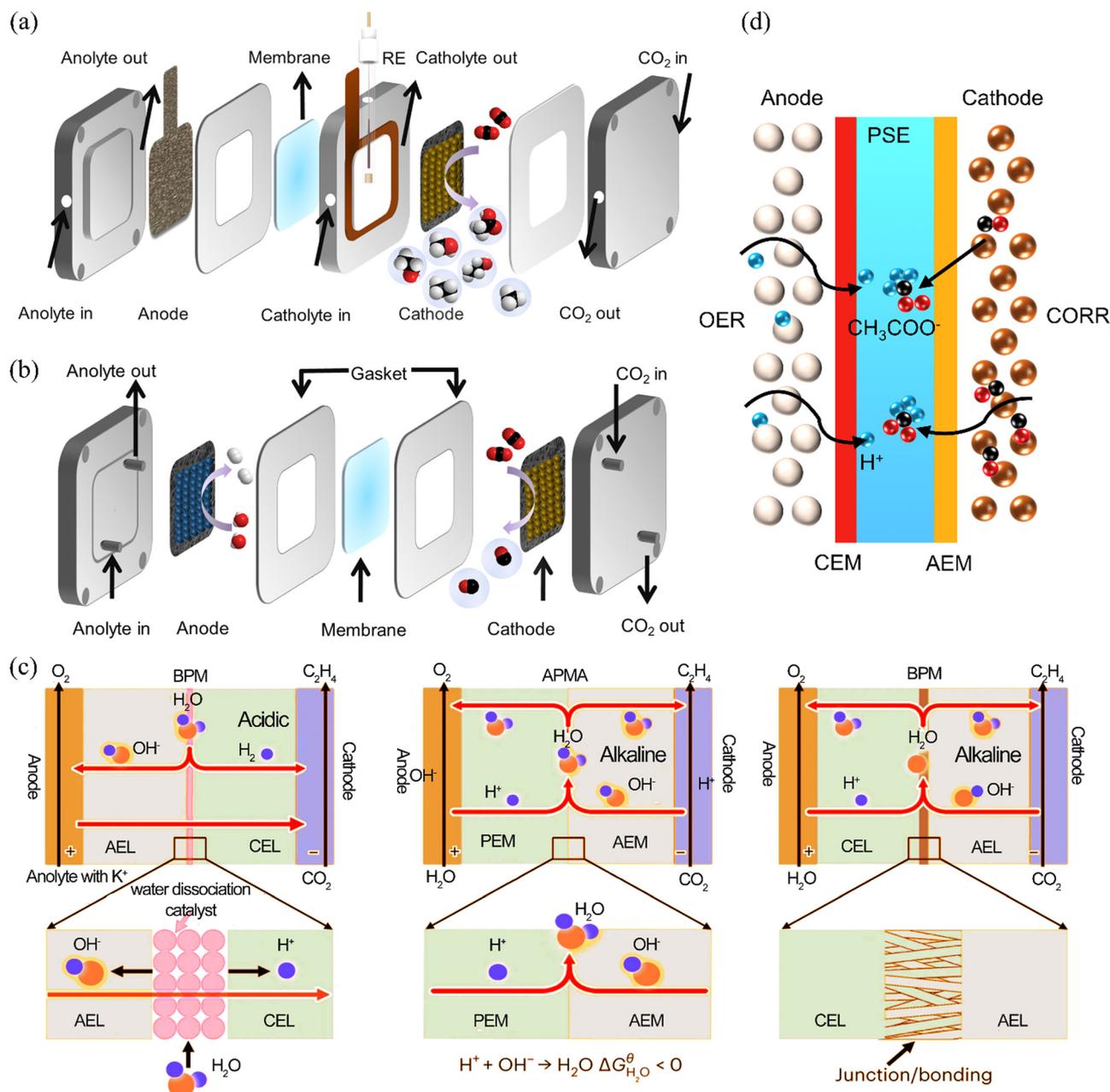
This journal is © The Royal Society of Chemistry 2025

Chem. Soc. Rev., 2025, **54**, 6973–7016 | 6997

Fig. 10 Electrolyzer engineering. (a) Schematic illustration of a flow cell. Reproduced with permission.[1] Copyright 2023, American Chemical Society. (b) Schematic illustration of MEA. (c) A comparison of different electrolysis systems for CO_2RR. Reproduced with permission.[376] Copyright 2024, Springer Nature. (d) Illustration of a solid electrolyte cell.

triple-interface.[267,373,374] Different from the traditional flow cell, a novel configuration was proposed,[375] which uses a filter press reactor in a continuous mode, with a Sustainion membrane for formate transfer from the cathodic to anodic component, and operating at 600 mA cm^{-2} on Bi-based catalysts. This reactor afforded high $FE_{formate}$ (73.7%) and production rate (22.9 mmol m^{-2} s^{-1}), demonstrating its potential for practical applications.

MEA as the zero-gap cell is another type of electrolyzer to enhance mass transfer for efficient CO_2/CO electrolysis (Fig. 10b), which eliminates the catholyte flow channel in flow cells, with two electrodes pressed together and separated by

ion-exchange membranes. Compared to flow cells, the MEA configuration exhibits significantly decreased resistance for mass transfer and electron transfer, thereby boosting the energy efficiency.[377]

Many works have been devoted to the MEA-based CO_2RR in alkaline electrolytes for efficient product formation. However, the serious carbonate formation by the CO_2 reaction with OH$^-$ is detrimental to the catalytic performance, which precipitates within the catalyst and GDLs and blocks the pores for CO_2 transfer, degrading the catalytic system and precluding the stable CO_2RR. To overcome these issues, a pure-water-fed

6998 | *Chem. Soc. Rev.*, 2025, **54**, 6973–7016

This journal is © The Royal Society of Chemistry 2025

(alkali-cation-free) MEA was designed for CO$_2$-to-ethylene conversion.[376] An anion-exchange membrane (AEM) + proton-exchange membrane (PEM) MEA (APMA) system involves an AEM at the cathode and a PEM at the anode, respectively. The APMA does not involve a water dissociation catalyst, different from the bipolar membrane (BPM) system (Fig. 10c), wherein water dissociation occurs at the cathode and anode to produce OH$^-$ and H$^+$ spontaneously, which are driven through AEM/PEM to take part in the oxygen evolution reaction/CO$_2$RR. The AEM helps to create an alkaline cathode environment, while PEM circumvents the crossover of all anions and facilitates CO$_2$ reduction at low cell voltages, meanwhile suppressing the HER and maintaining high conversion efficiencies. The BPM system exhibits the junction/bonding layer at the anion-exchange layer/cation-exchange layer (AML/CEL) interface, where H$_2$O forms, leading to delamination and further instability.

Other strategies to address carbonate formation include applying acid electrolytes,[214,352,378,379] using bipolar membranes,[380] proposing a self-cleaning CO$_2$ reduction strategy with short, periodic reductions in applied voltage,[381] dividing CO$_2$-to-C$_{2+}$ conversion in alkaline electrolytes into two steps of CO$_2$-to-CO followed by CO-to-C$_{2+}$,[1] physical washing, pulsed operation,[152] replacing K$^+$ to Cs$^+$ in the electrolyte due to the higher solubility of CsHCO$_3$ and Cs$_2$CO$_3$ than potassium salts, using solid electrolytes,[382] increasing the operating temperature (60–80 °C) to improve carbonate salt solubility, lowering the K$^+$ concentration in electrolytes,[383] performing direct CO$_2$ conversion from carbonate,[384] and applying the proton-exchange membrane system.[152]

Optimizing the flow fields in MEA contributes to developing high-current-density CO$_2$ electrolyzers.[385] The typical three flow fields of parallel, serpentine, and interdigitated exhibited weak, moderate, and excessive flow-through transport, respectively. Based on these, the CO$_2$ distribution uniformity is enhanced, no CO$_2$ starvation is ensured, CO$_2$ flow-through transport is provided, and suppressed drainage behavior is ensured. As a result, a multi-serpentine flow field, compared to the conventional parallel flow field, achieved high CO selectivity (95% at 0–350 mA cm^{-2}) and maximum j_{CO} (409 mA cm^{-2}). Meanwhile, the CO$_2$ mass transfer properties in MEA can be improved by controlling the cell compression via varying the gasket thickness,[386] which alternates the porosity and thickness of GDEs and affects the electrolyzer performance. Demonstrated by Ag-deposited GDEs, high and low compressed MEA present similar FE$_{CO}$ and j_{CO} at low voltages (<2.9 V), while the low compressed device illustrated outstanding selectivity and activity to CO and inhibited the HER.

Solid electrolyte cells have been proposed to promote ampere-level CO$_2$RR/CORR (Fig. 10d). For instance, assembled into a MEA with a porous solid electrolyte, the strongly coupled nanosheets with Ag NPs and Sn–SnO$_2$ grains (Ag/Sn–SnO$_2$ NSs) demonstrated continuous production of ∼0.12 M pure HCOOH solution at 100 mA cm^{-2} over 200 h.[26] The porous solid electrolytes (PSEs) afford direct generation of pure liquid acid solution, which efficiently delivers ions between the cathode and anode without introducing additional solutes. Humidified CO$_2$ is supplied to the cathode to generate HCOO$^-$ which is driven by electrical field to the PSE layer through AEM, while water oxidation occurs in the anode with 0.1 M H$_2$SO$_4$ circulation to produce H$^+$ which transfers through CEM to PSE. The generated HCOOH via ionic recombination is flushed out of the PSE layer by deionized (DI) water or N$_2$ vapor. The solid electrolyte cell not only avoids the carbonate formation in the alkaline CO$_2$RR in a flow cell, but also directly generates formic acid solutions (3.5 M) with 93% FE$_{formic\ acid}$ and 1.1 A partial current at 4.2 V.[387] Moreover, using solid electrolyte cells, liquid C$_2$H$_5$OH with 90% relative purity was generated on the Cu catalyst over 50 h continuous CO$_2$RR at 600 mA cm^{-2},[21] as well as >13 wt% ethanol on Cu over 80 h CO$_2$RR at 200 mA cm^{-2}.[388] Recently, a pure water fed MEA was deployed with a positively charged polyelectrolyte as an alternative to alkali cations and to modify Ag to avoid bicarbonate formation and achieve high-performance CO$_2$-to-CO conversion.[389] This enabled a 78% FE$_{CO}$ at 100 mA cm^{-2} and 55% EE at 200 mA cm^{-2} at room temperature (RT) but with much larger voltages. Increasing the temperature to mitigate the ohmic impedance from the diffusion limitation and voltage increase by using pure water resulted in larger current densities at the cell voltage, approaching 200 mA cm^{-2} at 3.5 V at 60 °C which dropped from 5 V at RT, together with 30% EE at 100 mA cm^{-2}, slightly smaller than the 35% in the acid-fed reactor. This strategy can also be applied universally for other CO-selective catalysts (Ni–N–C, CoPc).

Apart from the commercial CO$_2$RR applications, solid electrolyte cells also demonstrate continuous production of high-purity (96%) acetic acid solutions from the CORR on Cu nanocubes,[390] with a current density of 1 A cm^{-2}. Moreover, 90 mM pure acetic acid was generated over 120 h CORR around −4.45 V on Cu(25 nm)-CN-3 in a PSE device, with 55.6% FE$_{acetate}$ at 100 mA cm^{-2}.[391] Another exciting MEA-based CORR study with a solid-state electrolyte (SSE) illustrates that the highly lattice-disordered Cu$_3$N with abundant twin structures generates 17.4 vol% ethylene stream (1.45 M) and liquid C$_{2+}$ products (0.23 M) at the outlet of the cathode and SSE layer.[392] Additionally, the MEA using a SSE with a tandem catalyst,[393] a covalent organic framework and a metal–organic framework for respective CO$_2$-to-CO and CO-to-acetate, achieved 44% acetic acid selectivity at 160 mA cm^{-2} and 3.6 V, producing high-purity (95 wt%) 20 mM acetic acid solution over 200 h operation with stable FE$_{acetic\ acid}$ (43%) and current density (>150 mA cm^{-2}). All these works highlight the crucial roles of solid electrolyte cells in commercial CO$_2$RR/CORR applications.

Scaling-up of CO$_2$RR/CORR is conducted in cell-stacks based on the single MEA cells, with enlarged electrode area and more electrolyzer units. To improve the CO$_2$, electron, proton and product (CEPP) transfer at high current densities, an electrolyzer using the forced convection of the CO$_2$ saturated catholyte throughout the porous cathode (in situ electrodeposited Ag NPs on carbon fibers) was designed.[394] Induced by the CO$_2$ exsolution from dissolved CO$_2$ and bicarbonate, the CO$_2$RR device with flow-through induced dynamic triple-phase boundaries (FTDT) presented a high FE$_{CO}$ (92.0 ± 3.0% at 1.78 A cm^{-2} and

This journal is © The Royal Society of Chemistry 2025

Chem. Soc. Rev., 2025, 54, 6973–7016 | 6999

3.5 V) and maximum current density (3.37 A cm^{-2} at 4.5 V) on Ag-TEL. Differently, the GDE cells,[12] with created triple-phase boundaries involving inlets of the gas-phase CO_2 and liquid-phase alkaline catholyte, display maximum current density (j_{max}, 1.4 A cm^{-2}) but lose input CO_2 to bicarbonate/carbonate,[395] whereas the GDE cells using the humidified CO_2 inlet and MEA are effective in improving the stability,[396,397] but challenging to achieve j_{max} over 1 A cm^{-2}, due to the reduced ionic conductivity and low proton availability. When integrating a Cu-based catalyst, the FTDT cell exhibited 0.57 A cm^{-2} $j_{C_{2+}}$ at 3.1 V with stable $FE_{C_{2+}}$ (>55% at 2.7–3.1 V). Further amplification was conducted in the 4×100 cm^2 electrolyzer stack based on FTDT which produces CO with a yield of 90.6 L h^{-1} at 59.0 ± 2.6 A and 14 V. Impressively, the large-scale 140 cm^2 4-MEA cell stack using NiFe DAC[232] presents a high FE_{CO} (>97%) over 6 h continuous CO_2RR, a stable cell potential (12.2 V at 200 mA cm^{-2}) and exclusive CO yield ($\sim$45 L h^{-1}). As for C_{2+} production, the practicality is confirmed in a scaled-up CO_2 electrolyser stack consisting of six MEA cells,[376] wherein ultra-stability over 1000 h and 50% $FE_{C_2H_4}$ at 10 A are realized. Besides, the electrolyser stack of four 100 cm^2 MEA cells demonstrates the practical application of CO_2/CO electrolysis on CuO nanosheets,[154] delivering the largest formation rates of 457.5 mL min^{-1} at 150 A and 2.97 g min^{-1} at 250 A for ethylene and acetate, respectively.

Very recently, a stable and scalable electrode substrate was designed to resist flooding and operate stably over 400 h for CO_2-to-C_2H_4 conversion.[398] The enhanced stability originated from the hydrophobic PTFE percolating network in the microporous layer. Further scale tests were conducted in 800 cm^2 cell and 8000 cm^2 stack (ten 800 cm^2 MEA cells) with stability of 240 h at 100 A (125 mA cm^{-2}) and 240 h at 800 A (100 mA cm^{-2}), respectively. Impressively, a total charge transfer of 6.9×10^8 C was obtained, the largest reported CO_2RR demonstration to date. More impressively, a 1000 cm^2 CO electrolyzer at 0.71 kW and a 500 cm^2 CO^2 electrolyzer at 0.40 kW were designed successfully,[399] with the former one producing high-yield acetate (1.2 M with 96% purity at 300 A over 125 h) and ethylene.

4.3. Tandem/hybrid device systems

Most fundamental research focuses on catalyst design, overlooking the carbonate formation problem caused by the CO_2 reaction with OH$^-$ which results in huge voltage loss, significant CO_2 consumption, and deteriorated catalytic performance. This should be tackled for CO_2RR applications in real devices. To maximize the CO_2 utilization, tandem reaction systems are designed to enable two-step reduction of CO_2-to-CO and CO-to-C_{2+} in two separate devices. This tandem system is more attractive and effective in addressing the CO_2 loss issue and enhancing the stability. Tandem CO_2 electrolysis promotes $FE_{C_{2+}}$ by 25% compared to direct CO_2 electrolysis.[400] Other merits of tandem CO_2 electrolysis include affording engineered separate reaction environments (neutral conditions for CO_2-to-CO and alkaline for CO-to-C_{2+}) against carbonate formation,[401] kilowatt scale demonstration towards acetate and ethylene,[265,399] and production of

highly pure liquid products (acetate) with significantly reduced separation costs.

Beyond the above traditional CO_2/CO electrolyzers, CO_2/CO electrolyzers have been combined with other electrolyzers (cascade MEA,[402,403] second CO-to-C_2H_4 MEA,[404] tandem CO-to-C_{2+} MEA[405]) for producing C_3–C_6 acetate esters, ethylene and C_{2+} at high rates, respectively. Moreover, the hybrid systems have been developed successfully, which consist of CO_2/CO electrolyzers and subsequently a thermochemical hydroformylation device,[406] a C_2H_4 dimerizer,[407,408] a cascade C_2H_4 oxidation reactor,[409] a solid oxide water electrolyzer,[410] a syngas fermentation device,[411] a biological upgrading device,[412] a thermal catalytic device,[413] a thermochemical CO reduction device,[414] following a two-step cascade system (C_2H_4-bromoethanol-ethylene carbonate),[415] and a formaldehyde and alcohol dehydrogenase device[416] for generating respective propionaldehyde, butane, ethylene glycol, synthetic fuel, mid-chain fatty acid, butanol/hexanol, methanol, 3D-printed carbon nanocomposites, ethylene carbonate, and methanol, respectively. The tandem and hybrid strategy affords new opportunities to target products with higher value than that produced in a single-step process.

The typical two-step CO_2RR was operated in two flow cells with Ag and Cu GDEs for CO and C_{2+} production in non-alkaline and alkaline electrolytes, respectively.[417] The gas products of the first flow cell (CO, H_2) were purified to remove the unreacted CO_2 and then fed into the second flow cell for C_{2+} production. This configuration overcomes the issues of CO_2 loss and KOH consumption, delivering a cumulative $FE_{C_{2+}}$ of 62% at 300 mA cm^{-2}, 30% higher than that of a single-step electrolysis at the same current density. A similar two-flow cell structured tandem system was demonstrated by 3D Ni SAC and multi-hollow Cu_2O nanoparticles for CO and propanol production, respectively,[418] suggesting the feasibility of the tandem system, because of their unique capability of combining various catalysts and facile control over each step. Additionally, a tandem system consisting of two MEA cells exhibits significant potential for CO_2-to-C_{2+} conversion,[402,403] as well as a hybrid cascade system of an electrochemical reactor connected by thermochemical[407,408]/biological upgrading[412,419,420]/sygnas fermentation[411]/hydroformylation[406] devices in series. These systems afford renewable electricity-activated routines for slective produciton of valuable long-chain chemicals/fuels that can not be generated by a single reactor meanwhile circumventing the separaiton of unreacted CO_2 between the two reactors. However, these systems are challenged by high-concentration CO stream to the downstream CO electrolyser. The existence of unreacted CO_2 in the CO electrolyser results in carbonate generation, reducing the C_{2+} species production. The CO_2 electrolyzer must achieve highly efficient CO_2 consumption, and high gas separations costs are demanded to afford pure CO feed into the downstream. Therefore, developing robust and efficient Cu-based catalysts with high activity and selectivity, and their integration into tandem/hybrid membrane electrolyzers with avoidance of electrolyte and liquid product separation are promising to achieve green conversion of CO_2 and practical applications.

7000 | Chem. Soc. Rev., 2025, 54, 6973–7016

This journal is © The Royal Society of Chemistry 2025

5. Conclusions and perspectives

CO_2RR/CORR, powered by renewable electricity, affords a promising approach for closing the carbon cycle and producing high-value fuels. Although multi-scale research on CO_2RR/CORR at ampere current has achieved significant progress, its large-scale deployment still faces challenges. To commercialize CO_2RR/CORR, specific criteria should be considered. For instance, continuous electrolysis for 5000 h with a high energy efficiency (>60%),[421] operation at ampere current densities,[139,154] high pressure,[422] large electrode area (100 cm^2),[154] etc. Achieving these goals demands seriously addressing the crucial issues of low selectivity of specific C_{2+} products, unsatisfactory full cell energy efficiency, insufficient stability, high subsequent separation costs, etc. These challenges are in close relationship with the catalyst design, characterization of reaction mechanisms, and

mass transport control. The main challenges and perspectives for ampere-level CO_2RR/CORR are listed as follows (Scheme 2).

5.1. Challenges in achieving ampere-level CO_2RR/CORR

5.1.1. Low selectivity of specific C_{2+} products. C_1 product (CO, formate) has been achieved with a selectivity over 95% at ampere-level current. However, it is still challenging to obtain a specific C_{2+} product with high selectivity. Delving into the origins of low C_{2+} selectivity, the CO_2RR process is complicated, involving the HER, because of the inherent complexity from the sequential multi-step electron/proton transfer reaction pathways, which incur various products with the competitive HER consuming a huge amount of the produced charge, and C_{2+} species has sluggish kinetics, challenging the high C_{2+} selectivity. Besides, CO_2 is lost from either the reaction with OH^-
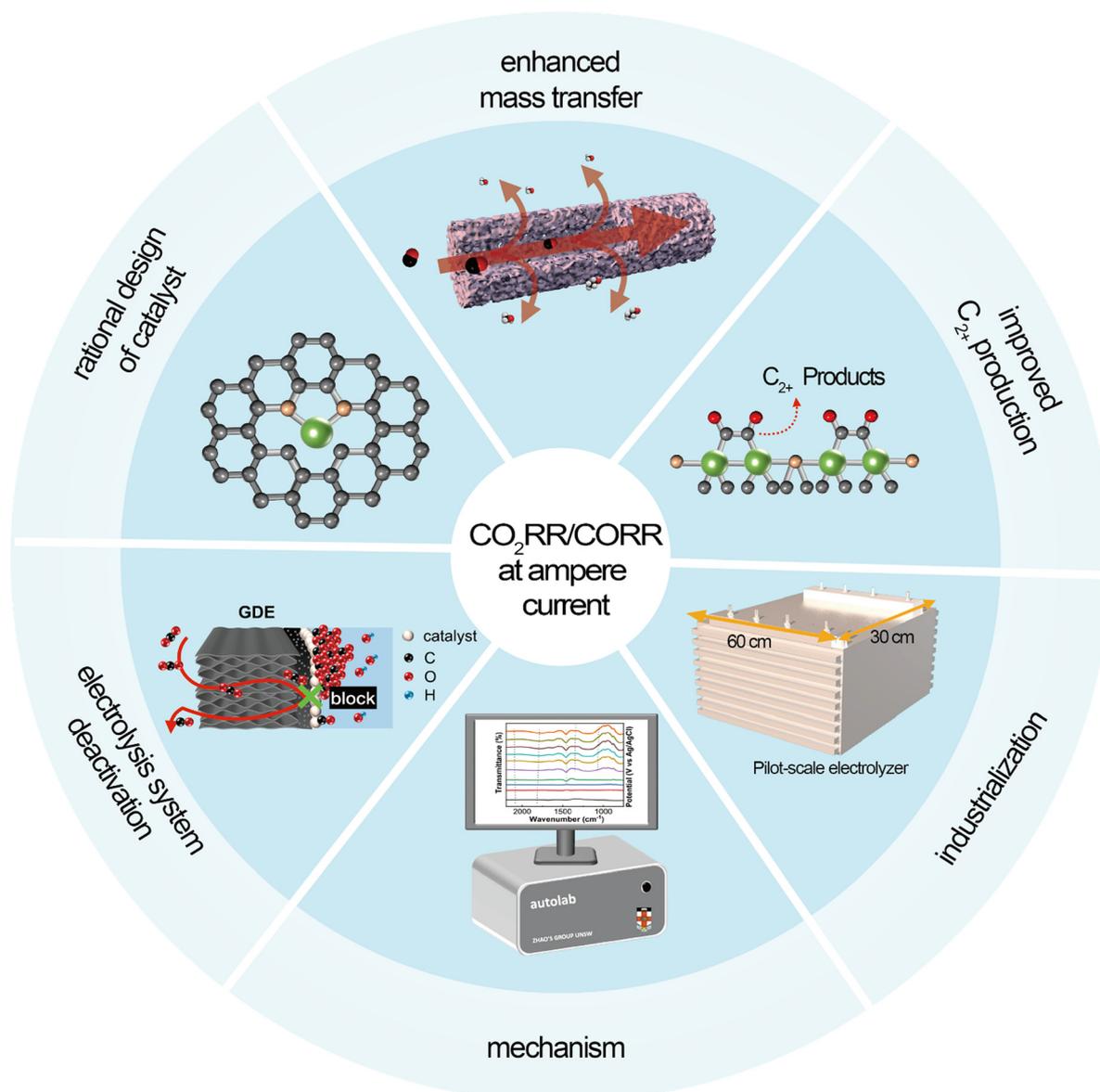
Scheme 2 Perspectives and strategies to accelerate CO_2RR/CORR at ampere-level current and the large-scale commercialization.

produced from electrochemical reduction on/near the catalyst surface or the bulk electrolyte. The high-rate OH^- production at high current densities (>200 mA cm^{-2}) constructs a highly alkaline environment at the electrode–electrolyte interface even in neutral electrolytes.[423] The building-up of surface CO coverage and utilization of the CO feed other than CO_2 are effective in elevating the C_{2+} selectivity and enriching the local CO concentration, respectively. From the CO_2RR, only ethylene exhibits 80% selectivity with 568 mA cm^{-2} $j_{C_2H_4}$,[376] followed by ethanol with 61.9% FE and 458.2 mA cm^{-2} $j_{ethanol}$.[237] From the CORR, the top two C_{2+} products are acetate and ethylene with FE of 70%[28] and 65%[424] obtained at partial current densities of 425 and 808 mA cm^{-2}, respectively. It is highly required to develop efficient catalysts for boosting the selectivity of specific C_{2+} species even higher and beyond these products.

5.1.2. Unsatisfactory energy efficiency. The full cell energy efficiency (EE) for CO_2-to-CO/formate has approached 80%,[26,232] while CO_2-to-C_{2+} typically has a EE less than 42%,[49] e.g. 26.1%[237] and 20%[316] for C_2H_5OH and C_2H_4, respectively. Besides, EE for all the CO_2RR products drops below 50% at reaction rates over 200 mA cm^{-2}.[34] As for the CORR, the EE for total C_{2+} is also less than 40%,[154] with 35–44%,[424] 27.6%,[28] and 21%[67] for C_2H_4, acetate, and n-propanol, respectively. Enhancing the full cell EE is limited by complicated factors such as catalyst degradation, electrode designs, membranes and electrolyzer assembly which incur high internal resistance. Especially, the electricity consumption of the CO_2RR accounts for a significant portion of product cost, which is more highlighted for the products beyond CO and formate, due to more electron transfer and higher energy demands, where electricity predominantly occupies the operation cost. Only a few studies reported satisfying overall EE $> 70\%$ at industrial-level current density.[425] Moreover, large proportion of the supplied electricity was consumed by the anodic reaction in the CO_2RR system, attributed to the thermodynamic and kinetic challenges of the oxygen evolution reaction (OER). Almost 90% of the input energy contribute to the OER, while only less than 10% is used for CO_2-to-CO.[426] Therefore, the anodic oxidations in the CO_2RR system should be considered with lower energy requirements than those in the OER to reduce the energy consumption and enhance the system economics. In addition, other factors also contribute to inferior EE, such as high reaction overpotentials, mass transfer limitations, ohmic loss, and interplay of the EE and current density.

5.1.3. Complicated dynamic process and mechanism. Both the CO_2RR and CORR proceed through multiple reduction pathways and intermediates. The current characterization conditions for catalysts do not match well with the actual reaction conditions. To acquire the catalyst structure during CO_2/CO electrolysis and understand the reaction mechanism, it is significant to perform in situ and operando characterization, especially at ampere-level current. Furthermore, the limitations (catalyst reconstruction, unstable testing system, undetectable intermediates) in full cells still exist from atomic to centimeter scales and time from femtoseconds to days.

5.1.4. Stability. Stability plays a crucial role in the industrial applications of CO_2RR/CORR. The reasons for instability include the materials aspects (difficulties in maintaining the size and morphology of catalysts, nanoparticle agglomeration, degradation, and limited thermodynamic/chemical/mechanical stability) and the non-materials aspects such as experimental conditions (pressure, current density, temperature, electrolyte, and reaction area) and system issues (flooding by decreased hydrophobicity of GDLs, carbonate formation, water control, high cell voltage, adherence of products on membranes and crossover to anodes leading to a destroyed membrane structure and blocked ion transfer). In more detail, the catalyst deactivation processes occur reversibly or irreversibly. Most metal-based catalysts (Cu_2O, SnO_2, Sn, Bi, Cu, Zn, and In) are challenged by the same electrochemical corrosion due to their high cathodic potentials and open-circuit potentials, and the chemical corrosion from the reaction with H^+, O_2, OH^-, and Cl^-/ClO^-.[427] This further leads to surface reconstruction (fragmentation, reshaping, agglomeration, and changes in the valence state and coordination environment). Other deactivation pathways include poisoning by intermediates/products/electrolyte impurities, steam feeding on facets, surface oxidation, detachment by electrolytes or bubbles, etc. In addition, flooding is detrimental to the stable operation of CO_2RR/CORR, which usually originates from the reduced hydrophobicity of surface carbon fibers in GDEs because of the electrochemical reactions and electrowetting.[428] Higher hydrophobicity contributes to high resistance against electrolyte penetration and flooding. Meanwhile, some other factors on flooding are pore size, porosity, electrode thickness, carbonate deposition, etc., which combine with more serious electrolyte leakage to hinder the efficient CO_2 transfer along the porous GDE channels. Moreover, the overwetting of the catalyst layers results in destroying the tri-phase boundary and decreasing the local CO_2 concentration around active sites. As a result, the HER is promoted while the CO_2RR being impeded over a long-term operation. Carbonate formation/accumulation occurs in the alkaline CO_2RR, which consumed a large amount of CO_2 and KOH, blocked the flow channels of gas chambers and porous networks of GDEs, and limited CO_2 mass transfer. Notably, the concurrence of flooding and carbonate deposition enables carbonate diffusion along the pore networks of GDEs and their growth on the back side of GDEs. Currently, all the above-mentioned factors entangled together, challenging the stable operation. Up to date, CO_2-to-C_1 conversion has exhibited stability over 1000 h but only with a small electrode area (mostly 1 cm^2).[34] The current-dependent stabilities for CO_2-to-CO, CO_2-to-formate and CO-to-formate have achieved 200 h at 2 A cm^{-2},[146] 520 h at 3 A cm^{-2},[346] and 1000 h at 1 A cm^{-2},[429] respectively, while the CO_2-to-C_{2+} and CO-to-C_{2+} conversions demonstrate a 100 h[348] and 200 h stability at 2 A cm^{-2},[146] respectively. Other outstanding stability reported for the CO_2RR and CORR has approached 1000 h at 100 mA cm^{-2},[430] 5200 h @ 600 mA cm^{-2},[152] and 500 h at 500 mA cm^{-2} (ref. 28) for formate and acetate, respectively. Nonetheless, upon increasing the electrode area and current density, the durability decreases rapidly, due to multiple factors of catalyst deactivation, carbonate accumulation and electrolyte degradation in the alkaline CO_2RR, the

7002 | Chem. Soc. Rev., 2025, **54**, 6973–7016

This journal is © The Royal Society of Chemistry 2025

application of membrane without sufficient mechanical and chemical stability, *etc.*

5.2. Perspectives

5.2.1. Rational design of catalysts. Promising catalysts should exhibit high activity and selectivity, strong mechanical stability, and robust durability to meet the requirements of practical applications. Approaches to rationally develop desired catalysts include alloying and doping,[431] preparing single-atom and multi-atom (*e.g.*, dual atom,[432–436] triple atom,[437,438] few atom or nanocluster[129,439–442]) catalysts, regulating the morphology and structure (shape, size, facets,[443] defects,[444] phases,[445,446] lattice tension, oxygen vacancy,[447,448] grain boundaries[449]), alternating the oxidation states, and introducing organic molecules to functionalize the catalysts. Among all these strategies, constructing single atom and multi-atom catalysts has been demonstrated to be effective and promising for $CO_2RR/CORR$ at ampere current density, due to the well-defined active sites, strong support–atom interactions, maximum metal utilization, outstanding activity and selectivity, and gram-scale preparation. Moreover, AI-assisted strategies also make significant contributions to developing efficient and advanced $CO_2RR/CORR$ catalysts.[450–460]

5.2.2. Multi-scale *in situ*/*operando* characterization. To understand the complicated catalytic mechanisms, it is imperative to deploy various *in situ*/*operando* characterization such as *in situ*/*operando* XAS, Raman, IR, XRD, XPS, *etc.*[76] These techniques benefit identifying the active sites/centers and intermediates, determining the electronic structure and coordination environment, tracking the dynamic changes of active sites, and elucidating the reduction pathways. These results can be further combined with theoretical calculations at the atomic or molecular level to gain insights into the electrochemical process and expand the understanding of the $CO_2RR/CORR$ mechanism at ampere-level current, thus guiding us to design more efficient catalysts for industrial CO_2/CO electrolysis deployment.

5.2.3. Enhanced mass transfer at ampere-level current. To enhance the mass transfer for boosting CO_2/CO electrolysis, effective strategies include developing porous electrodes, optimizing the electrode architecture, altering the thickness and porosity of GDL, constructing an efficient gas-solid–liquid triphase, and controlling the wettability or hydrophilicity/hydrophobicity by PTFE or other organic polymers. Electrolyzer engineering is another principle for enhancing mass transfer, including selection and optimization of the proper device (flow cells, MEA, solid state electrolyzers, cell stack), applying the pure-water-fed (alkali-cation-free) MEA, mitigating carbonate formation in the alkaline CO_2RR, and controlling the transfer of water and hydroxide at a quasi-two-phase interface to boost CO reduction. Especially, new electrolyzer architectures such as the BPM-based MEA,[461,462] low-resistance pressurized electrolyzers,[463] cascade/tandem devices,[464,465] and the electrolyzers for CO_2-to-CO using ionic liquid electrolytes[466] have shown promise to enable high conversion rates and full-cell energy efficiencies. Achieving rapid transfer using these two principles is an important prerequisite for $CO_2RR/CORR$ at ampere-level current.

5.2.4. Holistic design of $CO_2RR/CORR$ electrolysers. The design of electrolysers must be tailored to the type of catalysts, and *vice versa*. The reaction microenvironment and the electrode–electrolyser interfaces need to be understood and fine-tuned.[65,187,300,309,404,467–469] An alkaline and K^+-rich microenvironment significantly promotes the CO_2/CO-to-C_{2+} conversion with promising energy efficiency and carbon efficiency,[353,469] while normal Cu catalysts with modification of the intermediate distribution,[236] local CO availability,[424] the interfacial electric field and buffering local pH[352,470,471] demonstrate very high performance, highlighting the importance of designing the right environment for catalysts in the membrane electrode and electrolyser. On the other hand, to best promote mass transport in electrolysers for ampere-level electrolysis, the catalysts can be tuned with proper porosity, thickness, and morphologies for efficient mass transfer at ultrahigh reaction rates (ampere-level current densities), and with specific structures (facets, grain boundaries) for desirable products.

5.2.5. Improved production and cell efficiency. Only Cu-based catalysts have demonstrated reliable multi-carbon formation. To improve the C_{2+} species production, effective strategies include engineering the Cu-based catalysts by introducing a second metal into a single atom alloy, constructing an abrupt Cu interface,[11] functionalizing Cu catalysts with organic molecules for stabilization of the key intermediates, and assembling the efficient catalysts into a solid state cell for producing highly concentrated liquids such as acetate. Besides, applying efficient OER catalysts,[472–477] engineering the electrolytes (cations, anions, pH, concentration, composition) and ion-exchange membranes, developing energy-efficient electrolyzers, using pulsed electrolysis, and coupling $CO_2RR/CORR$ with the low-overpotential anodic reactions (alcohol oxidation,[478] glycerol oxidation,[426,479,480] H_2S oxidation, hydrazine oxidation, urea oxidation, methane oxidation, 5-hydroxymethylfurfural oxidization, 3-hydroxy decanoic acid oxidization,[30,481] Cl_2 evolution reaction[482]), other than the OER, are promising to reduce the energy consumption and obtain high energy efficiency, and contribute significantly to generating multi-carbon products, such as the co-product of acetate for CO_2/CO electrolysis and ethanol oxidation.[400] Furthermore, developing a cascade tandem electrocatalytic–thermocatalytic reaction system has been demonstrated to be effective in boosting the production of C_3 oxygenates[483] and butane,[408] which indicates their abilities to produce C_{2+} in practice.

5.2.6. Understanding degradation of the CO_2/CO electrolysis system. To advance $CO_2RR/CORR$ for practical applications, it is significant to explore the origins of the system deactivation. Especially for the long-term operation in MEA at ampere level electrolysis, which suffers from degradation of both catalysts[484] and electrolytes, as well as other issues such as flooding or salt accumulation and precipitation,[485] product accumulation, impurities, and bubbles.[428] Therefore, designing new technologies for real-time tracking of the electrolysis system plays crucial roles in unveiling the reasons for performance decay, including *operando* XAS for studying the evolution of chemical environments, *in situ* electrochemical electron

This journal is © The Royal Society of Chemistry 2025

Chem. Soc. Rev., 2025, **54**, 6973–7016 | 7003

microscopy with ultrahigh resolution for monitoring the atomic migration and active species in catalysts, surface-enhanced Raman, online inductively coupled mass spectrometry, and identical grain methodology for studying the electrocatalytic process, catalyst degradation, and facet-dependent reconstruction, respectively. New methods such as electrolysis optical coherence tomography,[486] distribution of relaxation times analysis,[487–489] neutron imaging,[490] interpretable machine learning,[491] and array tomography-guided systems[398] are highly desirable to precisely diagnose the attenuation of the activity and stability for electrolyzers and to identify the specific failure points to address these problems beyond those in GDEs.

5.2.7. Enhanced durability of the CO_2/CO electrolysis system. Based on diagnosing the degradation mechanism, stability should be promoted by rational design of catalysts/reactors, good control of salt precipitation to remove liquid droplets[492,493] and the salt formation prevention by quantifying cation accumulation.[494] Catalyst stability, durability and scalability of polymer-membrane-based CO_2/CO electrolysers are crucial for commercialization. At the catalyst level, apart from the remarkable stability mentioned in Section 5.1.4, with CO_2 supply, most stabilities were evaluated as 6 to 528 h and 2 to 280 h for CO and formate at 100 to 600 mA cm^{-2} (Tables S1 and S2, ESI†), respectively, the stable operation of CO_2-to-CH_4 maintained less than 20 h at 200 to 400 mA cm^{-2}, while the total C_{2+} species (C_2H_4, C_2H_5OH, C_{2+} alcohols, C_{2+} oxygenates, propanol) can be produced stably over 20–120 h at 300 to 900 mA cm^{-2}, with generally higher stability of gas products than the liquids except the 120 h propanol production at 100 mA cm^{-2}. Changing CO_2 into CO, the total C_{2+} species (acetate, C_2H_4, ethanol, oxygenates, propanol, C_{2+} alcohols) exhibited 100 to 300 h stability at 200 to 500 mA cm^{-2}, with favored acetate generation (100 to 500 h at 100 to 500 mA cm^{-2}) followed by propanol (100 to 120 h at 150 to 300 mA cm^{-2}), ethanol (30–400 h at 300 to 700 mA cm^{-2}) and C_2H_4 (8 to 100 h at 200 to 500 mA cm^{-2}). At the device level, durability at various current densities affects the production costs and profitability.[401] The year-long operation of feasible CO_2-to-CO demands 40, 85, and 45 mA cm^{-2} for AEM, PEM, and BPM, respectively, while effective formate production needs to be performed at a lower threshold (30 mA cm^{-2} for AEM, 75 mA cm^{-2} for BPM). Stability reduces almost 500 h for AEM and 1500 h for PEM for CO production at 300 mA cm^{-2}, and 300 to 750 h for formate, while operation at 300 to 500 mA cm^{-2} and 500 to 600 mA cm^{-2} decreases the stability requirements significantly with and without avoiding the diminishing returns at higher currents, respectively. Costs of membrane maintenance and catalyst replacement will further lift these thresholds. Enhancing the electrolyzer energy efficiency and applying low-cost renewable electricity help to improve economic viability for C_{2+} production with satisfying durability. Several aspects should be considered to achieve long-term operation: (1) stable bonding of catalysts with GDLs, (2) flooding and high gas transfer prevention and carbonate formation resistance, (3) selection of ion exchange membranes (IEMs) with high ion permeability and selectivity, and (4) optimization of device components. More efforts are required for developing new binders with high mechanical and electrochemical properties for achieving efficiency

and stability, designing long-term stable GDLs with high voltage resistance and precisely adjustable configuration, developing multifunctional and stable IEMs,[495] operating $CO_2RR/CORR$ at higher temperature (time–temperature equivalence principle) or a cyclic voltammetry method similar to that for the oxygen reduction reaction, and optimizing the electrolysers. Other strategies for achieving enhanced durability include alternation of the charge-transfer routes (doping, alloying, strong electronic interaction for ligand coordination), particle confinement (MOFs/COFs, CNTs, carbon shells, organic ligands), surface encapsulation (functional group, oxides, carbon shell), and reversible solid-phase transition.[427]

5.2.8. Commercialization of $CO_2RR/CORR$. By rational catalyst design and mass transfer control, ampere level $CO_2RR/CORR$ can be achieved to set a base for commercialization. To achieve this aim, firstly, catalysts with low cost, high efficiency and good stability should be synthesised from grams to kilograms,[338,496] for their large quantity applications in real devices (MEA,[497] high-throughput parallelized MEA,[498] pilot-scale CO_2/CO electrolyzers[499,500]). This requires the synthesis method to be industrially acceptable. Besides, optimization of the electrode area and architecture, device structure, reaction temperature, pressure, and huge volumes of electrolyte matter for efficient operation at ampere-level current densities is important. Moreover, directly converting CO_2 captured from air or simulated flue gas[501] makes $CO_2RR/CORR$ more attractive for practical applications. Developing modular devices integrated with air separation, CO_2 capture and conversion would benefit industrial applications and decrease the installation and maintenance cost and improve the equipment scalability. Furthermore, analysing the energy intensity of the product separation[502] and performing technoeconomic analysis including capital cost, operation cost, and product separation cost are required for assessing the economic feasibility,[503–505] paving the way for future industrialization.

Author contributions

Qian Sun: investigation, analysis, validation, and writing – review and editing. Chen Jia: writing – review and editing. Haochen Lu: writing – review and editing, Schemes 1 and 2 and TOC drawing. Mengmeng Yang: literature search, writing – review and editing, and summarizing Table 1. Ruirui Liu: literature search, writing – review and editing. Dan M. Villamanca: writing – review and editing. Yong Zhao: conception, resources, funding, writing – review and editing, and supervision. Chuan Zhao: conception, resources, funding, writing– review and editing, and supervision.

Data availability

The data supporting this article have been included as part of the ESI.†

Conflicts of interest

The authors declare no conflict of interest.

7004 | Chem. Soc. Rev., 2025, 54, 6973–7016

This journal is © The Royal Society of Chemistry 2025

Acknowledgements

References

1 Q. Sun, Y. Zhao, X. Tan, C. Jia, Z. Su, Q. Meyer, M. I. Ahmed and C. Zhao, *ACS Catal.*, 2023, **13**, 5689–5696.

2 Y. Ji, A. Guan and G. Zheng, *Cell Rep. Phys. Sci.*, 2022, **3**, 101072.

3 X. Zou and J. Gu, *Chin. J. Catal.*, 2023, **52**, 14–31.

4 Q. Sun, K. Dastafkan and C. Zhao, *Conversion of Water and CO₂ to Fuels using Solar Energy*, 2024, pp. 233–284.

5 J. Jiao, X. Kang, J. Yang, S. Jia, Y. Peng, S. Liu, C. Chen, X. Xing, M. He and H. Wu, *J. Am. Chem. Soc.*, 2024, **146**, 15917–15925.

6 A. Xu, S. F. Hung, A. Cao, Z. Wang, N. Karmodak, J. E. Huang, Y. Yan, A. Sedighian Rasouli, A. Ozden, F. Y. Wu, Z. Y. Lin, H. J. Tsai, T. J. Lee, F. Li, M. Luo, Y. Wang, X. Wang, J. Abed, Z. Wang, D. H. Nam, Y. C. Li, A. H. Ip, D. Sinton, C. Dong and E. H. Sargent, *Nat. Catal.*, 2022, **5**, 1081–1088.

7 Y. Ma, J. Wang, J. Yu, J. Zhou, X. Zhou, H. Li, Z. He, H. Long, Y. Wang and P. Lu, *Matter*, 2021, **4**, 888–926.

8 J. Yu, J. Wang, Y. Ma, J. Zhou, Y. Wang, P. Lu, J. Yin, R. Ye, Z. Zhu and Z. Fan, *Adv. Funct. Mater.*, 2021, **31**, 2102151.

9 J. Yu, J. Yin, R. Li, Y. Ma and Z. Fan, *Chem. Catal.*, 2022, **2**, 2229–2252.

10 H. Guan, Y. Zhang, W. Fan, K. Yang, G. Li, S. Chen, L. Li and J. Duan, *Small*, 2025, **21**, 2406605.

11 C. T. Dinh, T. Burdyny, M. G. Kibria, A. Seifitokaldani, C. M. Gabardo, F. P. G. De Arquer, A. Kiani, J. P. Edwards, P. De Luna and O. S. Bushuyev, *Science*, 2018, **360**, 783–787.

12 F. P. G. De Arquer, C. T. Dinh, A. Ozden, J. Wicks, C. McCallum, A. R. Kirmani, D. H. Nam, C. Gabardo, A. Seifitokaldani and X. Wang, *Science*, 2020, **367**, 661–666.

13 S. Verma, Y. Hamasaki, C. Kim, W. Huang, S. Lu, H. R. M. Jhong, A. A. Gewirth, T. Fujigaya, N. Nakashima and P. J. Kenis, *ACS Energy Lett.*, 2017, **3**, 193–198.

14 M. Jouny, G. S. Hutchings and F. Jiao, *Nat. Catal.*, 2019, **2**, 1062–1070.

15 K. Schouten, Y. Kwon, C. Van der Ham, Z. Qin and M. Koper, *Chem. Sci.*, 2011, **2**, 1902–1909.

16 Q. Sun, Y. Zhao, W. Ren and C. Zhao, *Appl. Catal., B*, 2022, **304**, 120963.

17 W. Ren, X. Tan, X. Chen, G. Zhang, K. Zhao, W. Yang, C. Jia, Y. Zhao, S. C. Smith and C. Zhao, *ACS Catal.*, 2020, **10**, 13171–13178.

18 S. Park, D. T. Wijaya, J. Na and C. W. Lee, *Catalysts*, 2021, **11**, 253.

19 J. Chen, C. Hu, Y. Liu, Y. Wei, K. Shen, L. Chen and Y. Li, *Angew. Chem., Int. Ed.*, 2024, e202422775.

20 Z. Chen, D. Zhang, Q. Li, H. Zhang, Y. Zhao, Q. Ke, Y. Yan, L. Liu, M. Liu and X. He, *Appl. Catal., B*, 2024, **341**, 123342.

21 M. Fang, M. Wang, Z. Wang, Z. Zhang, H. Zhou, L. Dai, Y. Zhu and L. Jiang, *J. Am. Chem. Soc.*, 2023, **145**, 11323–11332.

22 P. Li, J. Bi, J. Liu, Y. Wang, X. Kang, X. Sun, J. Zhang, Z. Liu, Q. Zhu and B. Han, *J. Am. Chem. Soc.*, 2023, **145**, 4675–4682.

23 X. D. Liang, Q. Z. Zheng, N. Wei, Y. Y. Lou, S. N. Hu, K. M. Zhao, H. G. Liao, N. Tian, Z. Y. Zhou and S. G. Sun, *Nano Energy*, 2023, **114**, 108638.

24 C. Peng, S. Yang, G. Luo, S. Yan, N. Chen, J. Zhang, Y. Chen, X. Wang, Z. Wang and W. Wei, *Chem*, 2023, **9**, 2830–2840.

25 H. Shen, Y. Zhao, L. Zhang, Y. He, S. Yang, T. Wang, Y. Cao, Y. Guo, Q. Zhang and H. Zhang, *Adv. Energy Mater.*, 2023, **13**, 2202818.

26 M. Zhang, A. Cao, Y. Xiang, C. Ban, G. Han, J. Ding, L. Y. Gan and X. Zhou, *Nano-Micro Lett.*, 2024, **16**, 1–15.

27 Z. Chen, X. Zhang, W. Liu, M. Jiao, K. Mou, X. Zhang and L. Liu, *Energy Environ. Sci.*, 2021, **14**, 2349–2356.

28 Y. Ji, Z. Chen, R. Wei, C. Yang, Y. Wang, J. Xu, H. Zhang, A. Guan, J. Chen and T. K. Sham, *Nat. Catal.*, 2022, **5**, 251–258.

29 Z. Xing, L. Hu, D. S. Ripatti, X. Hu and X. Feng, *Nat. Commun.*, 2021, **12**, 136.

30 Q. Sun, C. Jia and C. Zhao, *Encycl. Ionic Liq.*, 2022, 676–696.

31 Y. Wu, L. Charlesworth, I. Maglaya, M. N. Idros, M. Li, T. Burdyny, G. Wang and T. E. Rufford, *ACS Energy Lett.*, 2022, **7**, 2884–2892.

32 D. Ma, T. Jin, K. Xie and H. Huang, *J. Mater. Chem. A*, 2021, **9**, 20897–20918.

33 W. Ren, W. Ma and X. Hu, *Joule*, 2023, **7**, 2349–2360.

34 L. Lin, X. He, S. Xie and Y. Wang, *Chin. J. Catal.*, 2023, **53**, 1–7.

35 R. Shi, J. Guo, X. Zhang, G. I. Waterhouse, Z. Han, Y. Zhao, L. Shang, C. Zhou, L. Jiang and T. Zhang, *Nat. Commun.*, 2020, **11**, 3028.

36 C. Zhu, Y. Song, X. Dong, G. Li, A. Chen, W. Chen, G. Wu, S. Li, W. Wei and Y. Sun, *Energy Environ. Sci.*, 2022, **15**, 5391–5404.

37 A. Chen, C. Zhu, J. Mao, S. Li, G. Wu, Y. Wei, X. Liu, X. Dong, Y. Song and G. Li, *Appl. Catal., B*, 2024, **343**, 123493.

38 M. Zheng, P. Wang, X. Zhi, K. Yang, Y. Jiao, J. Duan, Y. Zheng and S. Z. Qiao, *J. Am. Chem. Soc.*, 2022, **144**, 14936–14944.

39 S. Kwon, J. Zhang, R. Ganganahalli, S. Verma and B. S. Yeo, *Angew. Chem., Int. Ed.*, 2023, **62**, e202217252.

40 H. Rabiee, J. K. Heffernan, L. Ge, X. Q. Zhang, P. H. Yan, E. Marcellin, S. H. Hu, Z. H. Zhu, H. Wang and Z. G. Yuan, *Appl. Catal., B*, 2023, **330**, 12258.

41 X. Wang, P. F. Ou, A. Ozden, S. F. Hung, J. Tam, C. M. Gabardo, J. Y. Howe, J. Sisler, K. Bertens, F. P. G. de Arquer, R. K. Miao, C. P. O'Brien, Z. Y. Wang, J. Abed, A. S. Rasouli, M. J. Sun, A. H. Ip, D. Sinton and E. H. Sargent, *Nat. Energy*, 2022, **7**, 170–176.

42 C. Jia, K. Dastafkan, W. Ren, W. Yang and C. Zhao, *Sustainable Energy Fuels*, 2019, **3**, 2890–2906.

43 Q. Sun, C. Jia, Y. Zhao and C. Zhao, *Chin. J. Catal.*, 2022, **43**, 1547–1597.

44 W. Yang, K. Dastafkan, C. Jia and C. Zhao, *Adv. Mater.*, 2018, **3**, 1700377.

45 M. Zhang, W. Wei, S. Zhou, D. D. Ma, A. Cao, X. T. Wu and Q. L. Zhu, *Energy Environ. Sci.*, 2021, **14**, 4998–5008.

This journal is © The Royal Society of Chemistry 2025

Chem. Soc. Rev., 2025, **54**, 6973–7016 | 7005

46 J. Chen, H. Qiu, Y. Zhao, H. Yang, L. Fan, Z. Liu, S. Xi, G. Zheng, J. Chen and L. Chen, *Nat. Commun.*, 2024, **15**, 5893.

47 J. R. Huang, X. F. Qiu, Z. H. Zhao, H. L. Zhu, Y. C. Liu, W. Shi, P. Q. Liao and X. M. Chen, *Angew. Chem., Int. Ed.*, 2022, **61**, e202210985.

48 Q. Hao, H. X. Zhong, J. Z. Wang, K. H. Liu, J. M. Yan, Z. H. Ren, N. Zhou, X. Zhao, H. Zhang and D. X. Liu, *Nat. Synth.*, 2022, **1**, 719–728.

49 Z. Liu, X. Lv, S. Kong, M. Liu, K. Liu, J. Zhang, B. Wu, Q. Zhang, Y. Tang and L. Qian, *Angew. Chem., Int. Ed.*, 2023, **62**, e202309319.

50 C. Peng, X. Zhu, Z. Xu, S. Yan, L. Y. Chang, Z. Wang, J. Zhang, M. Chen, T. K. Sham and Y. Li, *Small*, 2022, **18**, 2106433.

51 Y. Zhang, P. Li, C. Zhao, G. Zhou, F. Zhou, Q. Zhang, C. Su and Y. Wu, *Sci. Bull.*, 2022, **67**, 1679–1687.

52 O. S. Bushuyev, P. De Luna, C. T. Dinh, L. Tao, G. Saur, J. van de Lagemaat, S. O. Kelley and E. H. Sargent, *Joule*, 2018, **2**, 825–832.

53 J. Tang, E. Weiss and Z. Shao, *Carbon Neutralization*, 2022, **1**, 140–158.

54 A. Klinkova, P. De Luna, C.-T. Dinh, O. Voznyy, E. M. Larin, E. Kumacheva and E. H. Sargent, *ACS Catal.*, 2016, **6**, 8115–8120.

55 N. J. Firet and W. A. Smith, *ACS Catal.*, 2017, **7**, 606–612.

56 Z. Yao, H. Cheng, Y. Xu, X. Zhan, S. Hong, X. Tan, T. S. Wu, P. Xiong, Y. L. Soo and M. M. J. Li, *Nat. Commun.*, 2024, **15**, 9881.

57 S. Zhao, S. Li, T. Guo, S. Zhang, J. Wang, Y. Wu and Y. Chen, *Nano-Micro Lett.*, 2019, **11**, 1–19.

58 B. Zhang, Y. Chang, Y. Wu, Z. Fan, P. Zhai, C. Wang, J. Gao, L. Sun and J. Hou, *Adv. Energy Mater.*, 2022, **12**, 2200321.

59 R. Kortlever, J. Shen, K. J. P. Schouten, F. Calle-Vallejo and M. T. Koper, *J. Phys. Chem. Lett.*, 2015, **6**, 4073–4082.

60 A. A. Peterson, F. Abild-Pedersen, F. Studt, J. Rossmeisl and J. K. Nørskov, *Energy Environ. Sci.*, 2010, **3**, 1311–1315.

61 S. Back, H. Kim and Y. Jung, *ACS Catal.*, 2015, **5**, 965–971.

62 L. Fan, C. Xia, F. Yang, J. Wang, H. Wang and Y. Lu, *Sci. Adv.*, 2020, **6**, eaay3111.

63 J. Zhang, C. Zhang, M. Wang, Y. Mao, B. Wu, Q. Yang, B. Wang, Z. Mi, M. Zhang and N. Ling, *Nat. Chem.*, 2025, 1–10.

64 W. Ge, L. Dong, C. Wang, Y. Zhu, Z. Liu, H. Jiang and C. Li, *ACS Catal.*, 2024, **14**, 10529–10537.

65 M. Jouny, W. Luc and F. Jiao, *Nat. Catal.*, 2018, **1**, 748–755.

66 Q. Xu, B. Ó. Joensen, N. C. Kani, A. Sartori, T. Wilson, J. R. Varcoe, L. Riillo, A. Ramunni, J. Drnec and I. Chorkendorff, *Angew. Chem., Int. Ed.*, 2025, e202501505.

67 L. J. Richter, A. R. Kirmani, X. Wang, W. Ziyuan, D. Cao-Thang, L. Jun, N. Dae-Hyun, L. Fengwang, H. Chun-Wei and T. Chih-Shan, *Nat. Commun.*, 2019, **10**, 5186.

68 J. Zhang, P. Yu, C. Peng, X. Lv, Z. Liu, T. Cheng and G. Zheng, *ACS Catal.*, 2023, **13**, 7170–7177.

69 F. Calle-Vallejo and M. T. Koper, *Angew. Chem., Int. Ed.*, 2013, **125**, 7423–7426.

70 H. Xiao, T. Cheng, W. A. Goddard III and R. Sundararaman, *J. Am. Chem. Soc.*, 2016, **138**, 483–486.

71 C. Yang, Y. Yan, Y. Hu, Y. Chen, A. Guan, C. Hu, L. Zhang and G. Zheng, *Small Methods*, 2024, **9**, 2400393.

72 T. Cheng, H. Xiao and W. A. Goddard III, *Proc. Natl. Acad. Sci. U. S. A.*, 2017, **114**, 1795–1800.

73 Y. Lum, T. Cheng, W. A. Goddard III and J. W. Ager, *J. Am. Chem. Soc.*, 2018, **140**, 9337–9340.

74 T. Cheng, A. Fortunelli and W. A. Goddard III, *Proc. Natl. Acad. Sci. U. S. A.*, 2019, **116**, 7718–7722.

75 L. Chen, C. Tang, K. Davey, Y. Zheng, Y. Jiao and S. Z. Qiao, *Chem. Sci.*, 2021, **12**, 8079–8087.

76 A. Prajapati, C. Hahn, I. M. Weidinger, Y. Shi, Y. Lee, A. N. Alexandrova, D. Thompson, S. R. Bare, S. Chen and S. Yan, *Nat. Commun.*, 2025, **16**, 2593.

77 R. Yang, M. Wu, D. Huang, Y. Yang, Y. Liu, L. Zhang, F. Lai, B. You, J. Fang and T. Liu, *Energy Environ. Sci.*, 2024, **17**, 2897.

78 J. Wang, H. Y. Tan, C. S. Hsu, Y. C. Chu, C. W. Chan, K. H. Chen, X. R. Lin, Y. C. Lee, H. C. Chen and H. M. Chen, *J. Am. Chem. Soc.*, 2025, **147**, 13027–13038.

79 J. Leverett, G. Baghestani, T. Tran-Phu, J. A. Yuwono, P. Kumar, B. Johannessen, D. Simondson, H. Wen, S. L. Chang and A. Tricoli, *Angew. Chem., Int. Ed.*, 2025, e202424087.

80 M. Wang, Y. Li, J. Jia, T. Ghosh, P. Luo, Y.-J. Shen, S. Wang, J. Zhang, S. Xi and Z. Mi, *Sci. Adv.*, 2025, **11**, eado5000.

81 Y. Zang, S. Wang, J. Sang, P. Wei, X. Zhang, Q. Wang and G. Wang, *Nano Lett.*, 2024, **24**, 7261–7268.

82 T. D. Nguyen-Phan, L. Hu, B. H. Howard, W. Xu, E. Stavitski, D. Leshchev, A. Rothenberger, K. C. Neyerlin and D. R. Kauffman, *Sci. Rep.*, 2022, **12**, 8420.

83 H. Phong Duong, J. G. Rivera de la Cruz, D. Portehault, A. Zitolo, J. Louis, S. Zanna, Q. Arnoux, M. W. Schreiber, N. Menguy and N.-H. Tran, *Nat. Mater.*, 2025, 1–7.

84 S. Lin, C. S. Diercks, Y.-B. Zhang, N. Kornienko, E. M. Nichols, Y. Zhao, A. R. Paris, D. Kim, P. Yang and O. M. Yaghi, *Science*, 2015, **349**, 1208–1213.

85 N. Morlanes, K. Takanabe and V. Rodionov, *ACS Catal.*, 2016, **6**, 3092–3095.

86 L. Ma, D. Geng, M. Tan, J. Li, R. Guo, Z. Zhai, X. Liu, J. Chen and Q. Li, *Appl. Catal., B*, 2025, **369**, 125153.

87 Z. Wei, W. Wang, T. Shao, S. Yang, C. Liu, D. Si, R. Cao and M. Cao, *Angew. Chem., Int. Ed.*, 2024, **6**, e202417066.

88 X. Li, M. Qin, X. Wu, X. Lv, J. Wang, Y. Wang and H. B. Wu, *Small*, 2023, **19**, 2302530.

89 Y. Chang, Z. Tan, J. Han, C. Ji, Q. Gao, J. Zhang and C. Pan, available at SSRN 5168331, http://dx.doi.org/10.2139/ssrn.5168331.

90 L. Li, S. Yao, Y. Feng, Z. Gao, J. Wang, P. Yin, H. Liu and Z. Zhang, *Appl. Catal., B*, 2025, **372**, 125302.

91 K. Yang, R. Kas and W. A. Smith, *J. Am. Chem. Soc.*, 2019, **141**, 15891–15900.

92 B. Jia, Z. Chen, C. Li, Z. Li, X. Zhou, T. Wang, W. Yang, L. Sun and B. Zhang, *J. Am. Chem. Soc.*, 2023, **145**, 14101–14111.

7006 | *Chem. Soc. Rev.*, 2025, **54**, 6973–7016

This journal is © The Royal Society of Chemistry 2025

93 Z. Wang, H. Li, T. Dong, Y. Geng, X. Tian, R. Chang, J. Lai, S. Feng and L. Wang, *Chem. Eng. J.*, 2024, **489**, 151238.

94 W. Ji, B. Liu, J. Zhang, J. Zhu, W. Zhou, T. Guo, L. Guo, X. Jiang, M. Ya and Z. Zhang, *Green Chem.*, 2025, **27**, 4679–4687.

95 H. Yun, S. Yoo, J. Son, J. H. Kim, J. Wu, K. Jiang, H. Shin and Y. J. Hwang, *Chem*, 2025, 102461.

96 R. Chen, Q. Wu, J. Zhu, S. Wang, Z. Hu, J. Hu, J. Zhu, H. Zhang, B. Ye and Y. Sun, *J. Am. Chem. Soc.*, 2025, **147**, 7921–7931.

97 Q. Huang, Z. Qian, N. Ye, Y. Tan, M. Li, M. Luo and S. Guo, *Adv. Mater.*, 2024, **37**, 2415639.

98 L. Bian, Y. Bai, J. Y. Chen, H. K. Guo, S. Liu, H. Tian, N. Tian and Z. L. Wang, *ACS Nano*, 2025, **19**, 9304–9316.

99 K. Wang, K. Huang, Z. Wang, G. An, M. Zhang, W. Liu, S. Fu, H. Guo, B. Zhang and C. Lian, *Small*, 2025, 2502733.

100 H. Wang, R. Sun, P. Liu, H. Hu, C. Ling, X. Han, Y. Shi, X. Zheng, G. Wu and X. Hong, *Nano Res.*, 2024, **17**, 7013–7019.

101 Y. Yin, Z. Ling, S. Liu, J. Jiao, M. Zhou, P. Zhang, X. Tong, Y. Fan, J. Yang and H. Liu, *The Innovation*, 2025, 100882.

102 X. Li, S. Wang, L. Li, Y. Sun and Y. Xie, *J. Am. Chem. Soc.*, 2020, **142**, 9567–9581.

103 Y. Yang, S. Louisia, S. Yu, J. Jin, I. Roh, C. Chen, M. V. Fonseca Guzman, J. Feijóo, P.-C. Chen and H. Wang, *Nature*, 2023, **614**, 262–269.

104 Y. Yang, Y.-T. Shao, J. Jin, J. Feijóo, I. Roh, S. Louisia, S. Yu, M. V. Fonseca Guzman, C. Chen and D. A. Muller, *ACS Sustainable Chem. Eng.*, 2023, **11**, 4119–4124.

105 E. Zhang, T. Wang, K. Yu, J. Liu, W. Chen, A. Li, H. Rong, R. Lin, S. Ji and X. Zheng, *J. Am. Chem. Soc.*, 2019, **141**, 16569–16573.

106 J. P. Grote, A. R. Zeradjanin, S. Cherevko and K. J. J. Mayrhofer, *Rev. Sci. Instrum.*, 2014, **85**, 104101.

107 P. Dubé and G. M. Brisard, *J. Electroanal. Chem.*, 2005, **582**, 230–240.

108 E. L. Clark, M. R. Singh, Y. Kwon and A. T. Bell, *Anal. Chem.*, 2015, **87**, 8013–8020.

109 Z. Li, L. Wang, L. Sun and W. Yang, *J. Am. Chem. Soc.*, 2024, **146**, 23901–23908.

110 Y. Jiang, C. Lv, B. Lu, Y. Song, T. Liu, X. Zhang, D. Gao, K. Ye and G. Wang, *ACS Nano*, 2025, **19**, 11263–11272.

111 Y. Sun, X. Liu, J. Tian, Z. Zhang, Y. Li, Y. Xie, M. Hao, Z. Chen, H. Yang and G. I. Waterhouse, *ACS Nano*, 2025, **19**, 4528–4540.

112 M. Fang, L. Xu, H. Zhang, Y. Zhu and W.-Y. Wong, *J. Am. Chem. Soc.*, 2022, **144**, 15143–15154.

113 M. Wen, N. N. Sun, L. Jiao, S. Q. Zang and H. L. Jiang, *Angew. Chem., Int. Ed.*, 2024, **63**, e202318338.

114 J. Song, D. He, X. Ma, P. Liu, W. Guo, R. Sun, F. Li, Z. Zhong, H. Zhou and J. Tang, *J. Am. Chem. Soc.*, 2025, **147**, 16198–16206.

115 T. Liu, D. Zhang, Y. Hirai, K. Ito, K. Ishibashi, N. Todoroki, Y. Matsuo, J. Yoshida, S. Ono and H. Li, *Adv. Sci.*, 2025, 2501459.

116 Y. Song, J. Min, Y. Guo, R. Li, G. Zou, M. Li, Y. Zang, W. Feng, X. Yao and T. Liu, *Angew. Chem., Int. Ed.*, 2024, **63**, e202313361.

117 C. Peng, S. Yang, G. Luo, S. Yan, M. Shakouri, J. Zhang, Y. Chen, Z. Wang, W. Wei and T. K. Sham, *Small*, 2023, **19**, 2207374.

118 S. Hu, Y. Chen, Z. Zhang, H. Liu, X. Kang, J. Liu, S. Li, Y. Luo and B. Liu, *Angew. Chem., Int. Ed.*, 2025, **64**, e202423915.

119 Z. Li, P. Wang, X. Lyu, V. K. R. Kondapalli, S. Xiang, J. D. Jimenez, L. Ma, T. Ito, T. Zhang and J. Raj, *Nat. Chem. Eng.*, 2024, **1**, 159–169.

120 S. Yan, C. Peng, C. Yang, Y. S. Chen, J. B. Zhang, A. X. Guan, X. M. Lv, H. Z. Wang, Z. Q. Wang, T. K. Sham, Q. Han and G. F. Zheng, *Angew. Chem., Int. Ed.*, 2021, **133**, 25945–25949.

121 Y. Shen, Z. Wang, Y. Wang and C. Wang, *Artif. Intell. Chem.*, 2024, **2**, 100056.

122 Z. Jiang, S. Ren, X. Cao, Q. Fan, R. Yu, J. Yang and J. Mao, *Angew. Chem., Int. Ed.*, 2024, **136**, e202408412.

123 W. Ma, S. Xie, T. Liu, Q. Fan, J. Ye, F. Sun, Z. Jiang, Q. Zhang, J. Cheng and Y. Wang, *Nat. Catal.*, 2020, **3**, 478–487.

124 T. Zheng, C. Liu, C. Guo, M. Zhang, X. Li, Q. Jiang, W. Xue, H. Li, A. Li and C.-W. Pao, *Nat. Nanotechnol.*, 2021, **16**, 1386–1393.

125 C. Jin, Y. Lin, Y. Wang, J. Shi, R. Li, Y. Liu, Z. Yue, K. Leng, Y. Zhao and Y. Wang, *Adv. Mater.*, 2025, 2412658.

126 H. Shen, T. Wang, H. Jiang, P. Zhao, Z. Chen, Y. Feng, Y. Cao, Y. Guo, Q. Zhang and H. Zhang, *Appl. Catal., B*, 2023, **339**, 123140.

127 X. Yu, Y. Xu, L. Li, M. Zhang, W. Qin, F. Che and M. Zhong, *Nat. Commun.*, 2024, **15**, 1711.

128 S. Yan, Z. Chen, Y. Chen, C. Peng, X. Ma, X. Lv, Z. Qiu, Y. Yang, Y. Yang and M. Kuang, *J. Am. Chem. Soc.*, 2023, **145**, 26374–26382.

129 M. Salehi, H. Al-Mahayni, A. Farzi, M. McKee, S. Kaviani, E. Pajootan, R. Lin, N. Kornienko and A. Seifitokaldani, *Appl. Catal., B*, 2024, **353**, 124061.

130 C. Zhang, X. Hao, J. Wang, X. Ding, Y. Zhong, Y. Jiang, M. C. Wu, R. Long, W. Gong and C. Liang, *Angew. Chem., Int. Ed.*, 2024, **136**, e202317628.

131 X. Chen, R. Lu, C. Li, W. Luo, R. Yu, J. Zhu, L. Lv, Y. Dai, S. Gong, Y. Zhou, W. Xiong, J. Wu, H. Cai, X. Wu, Z. Deng, B. Xing, L. Su, F. Wang, F. Chao, W. Chen, C. Xia, Z. Wang and L. Mai, *Nat. Commun.*, 2025, **16**, 1927.

132 Q. Liu, Y. Tan, Q. Chen, X. Zi, Z. Mei, Q. Wang, K. Liu, J. Fu, C. Ma and L. Chai, *Nano Lett.*, 2024, **24**, 13741–13746.

133 Y. Wang, J. Wang, R. Cai, J. Zhang, S. Xia, Z. Li, C. Yu, J. Wu, P. Wang and Y. Wu, *Adv. Funct. Mater.*, 2024, **35**, 2417764.

134 X. Ma, T. Yang, D. He, X. Gao, W. Jiang, D. Li, Y. Sun, X. Lin, J. Xu and H. Wang, *Nat. Synth.*, 2025, **4**, 53–66.

135 T. Zhang, J. C. Bui, Z. Li, A. T. Bell, A. Z. Weber and J. Wu, *Nat. Catal.*, 2022, **5**, 202–211.

136 R. Yang, Q. Wen, Y. Yang, Y. Liu, Y. Yang, M. Wu, Y. Wei, B. Mei, Y. Liu and H. Li, *Adv. Mater.*, 2025, **37**, 2414642.

137 Z. Li, X. Li, R. Wang, A. Campos Mata, C. S. Gerke, S. Xiang, A. Mathur, L. Zhang, D. Z. Lin and T. Li, *Nat. Commun.*, 2025, **16**, 3206.

This journal is © The Royal Society of Chemistry 2025

Chem. Soc. Rev., 2025, **54**, 6973–7016 | 7007

138 Z. Tan, J. Zhang, Y. Yang, J. Zhong, Y. Zhao, Y. Teng, B. Han and Z. Chen, *Nat. Commun.*, 2025, **16**, 1843.

139 Z. H. Tan, J. L. Zhang, Y. S. Yang, J. J. Zhong, Y. Z. Zhao, J. Y. Hu, B. X. Han and Z. J. Chen, *J. Am. Chem. Soc.*, 2023, **145**, 21983–21990.

140 J. Q. Feng, Y. L. Wang, G. L. Li, Q. Z. Xue, M. Wang, X. F. Sun, S. J. Zeng and X. P. Zhang, *Appl. Catal., B*, 2025, **366**, 125014.

141 M. P. L. Kang, H. Ma, R. Ganganahalli and B. S. Yeo, *ACS Catal.*, 2023, **14**, 116–123.

142 M. Sun, J. Cheng and M. Yamauchi, *Nat. Commun.*, 2024, **15**, 491.

143 C. J. Chen, X. P. Yan, Y. H. Wu, S. J. Liu, X. D. Zhang, X. F. Sun, Q. G. Zhu, H. H. Wu and B. X. Han, *Angew. Chem., Int. Ed.*, 2022, **61**, e202202607.

144 S. Chen, B. Rowley, R. Ganganahalli and B. S. Yeo, *Adv. Sci.*, 2024, **11**, 2405938.

145 S. Li, W. Chen, X. Dong, C. Zhu, A. Chen, Y. Song, G. Li, W. Wei and Y. Sun, *Nat. Commun.*, 2022, **13**, 3080.

146 X. Dong, S. J. Li, C. Zhu, J. N. Mao, G. F. Wu, G. H. Li, G. H. Feng, A. H. Chen, Y. H. Wei, X. H. Liu, J. J. Wang, Y. F. Song, W. Chen and W. Wei, *Appl. Catal., B*, 2023, **336**, 122929.

147 S. J. Li, X. Dong, Y. H. Zhao, J. N. Mao, W. Chen, A. H. Chen, Y. F. Song, G. H. Li, Z. Jiang, W. Wei and Y. H. Sun, *Angew. Chem., Int. Ed.*, 2022, **61**, e202210432.

148 S. Li, G. Wu, J. Mao, A. Chen, X. Liu, J. Zeng, Y. Wei, J. Wang, H. Zhu, J. Xia, X. Wang, G. Li, Y. Song, X. Dong, W. Wei and W. Chen, *Angew. Chem., Int. Ed.*, 2024, **63**, e202407612.

149 W. Ren, H. Zhang, M. Chang, N. Chen, W. Ma, J. Gu, M. Lin and X. Hu, *Chem*, 2024, **11**, 102352.

150 X. Zi, Y. Zhou, L. Zhu, Q. Chen, Y. Tan, X. Wang, M. Sayed, E. Pensa, R. A. Geioushy and K. Liu, *Angew. Chem., Int. Ed.*, 2023, **62**, e202309351.

151 B. Endrődi, E. Kecsenovity, A. Samu, T. Halmágyi, S. Rojas-Carbonell, L. Wang, Y. Yan and C. Janáky, *Energy Environ. Sci.*, 2020, **13**, 4098–4105.

152 W. S. Fang, W. Guo, R. H. Lu, Y. Yan, X. K. Liu, D. Wu, F. M. Li, Y. S. Zhou, C. H. He, C. F. Xia, H. T. Niu, S. C. Wang, Y. W. Liu, Y. Mao, C. Y. Zhang, B. You, Y. J. Pang, L. L. Duan, X. Yang, F. Song, T. Y. Zhai, G. X. Wang, X. P. Guo, B. Tan, T. Yao, Z. Y. Wang and B. Y. Xia, *Nature*, 2024, **626**, 86–91.

153 A. Inoue, T. Harada, S. Nakanishi and K. Kamiya, *EES. Catal.*, 2023, **1**, 9–16.

154 P. F. Wei, D. F. Gao, T. F. Liu, H. F. Li, J. Q. Sang, C. Wang, R. Cai, G. X. Wang and X. H. Bao, *Nat. Nanotechnol.*, 2023, **18**, 299–306.

155 X. Lu, T. Shinagawa and K. Takanabe, *ACS Catal.*, 2023, **13**, 1791–1803.

156 Y. Chen, R. K. Miao, C. Yu, D. Sinton, K. Xie and E. H. Sargent, *Matter*, 2024, **7**, 25–37.

157 Z. W. Seh, J. Kibsgaard, C. F. Dickens, I. Chorkendorff, J. K. Nørskov and T. F. Jaramillo, *Science*, 2017, **355**, eaad4998.

158 J. Zhou, B. He, P. Huang, D. Wang, Z. Zhuang, J. Xu, C. Pan, Y. Dong, D. Wang and Y. Wang, *Angew. Chem., Int. Ed.*, 2024, **137**, e202418459.

159 C. Peng, S. Yang, G. Luo, S. Yan, M. Shakouri, J. Zhang, Y. Chen, W. Li, Z. Wang and T. K. Sham, *Adv. Mater.*, 2022, **34**, 2204476.

160 R. Chen, Y. Jiang, Y. Zhu, L. Zhang, Y. Li and C. Li, *Adv. Funct. Mater.*, 2024, 2415940.

161 B. Kim, Y. C. Tan, Y. Ryu, K. Jang, H. G. Abbas, T. Kang, H. Choi, K. S. Lee, S. Park and W. Kim, *ACS Energy Lett.*, 2023, **8**, 3356–3364.

162 Y. Jiang, J. Shan, P. Wang, L. Huang, Y. Zheng and S. Z. Qiao, *ACS Catal.*, 2023, **13**, 3101–3108.

163 P. Wang, H. Yang, C. Tang, Y. Wu, Y. Zheng, T. Cheng, K. Davey, X. Huang and S. Z. Qiao, *Nat. Commun.*, 2022, **13**, 3754.

164 J. Feng, L. Wu, X. Song, L. Zhang, S. Jia, X. Ma, X. Tan, X. Kang, Q. Zhu and X. Sun, *Nat. Commun.*, 2024, **15**, 4821.

165 C. Jia, X. Tan, Q. Sun, R. Liu, R. K. Hocking, S. Wang, L. Zhong, Z. Shi, S. Smith and C. Zhao, *Adv. Mater.*, 2025, 2417443.

166 J. Lu, Y. Ren, J. Liang, L. Zou, Y. Gao, F. Li, J. Gao and J. Liu, *Small*, 2024, **20**, 2402879.

167 Y. Wang, H. Xu, Y. Liu, J. Jang, X. Qiu, E. P. Delmo, Q. Zhao, P. Gao and M. Shao, *Angew. Chem., Int. Ed.*, 2024, **63**, e202313858.

168 H. Shen, H. Jin, H. Li, H. Wang, J. Duan, Y. Jiao and S. Z. Qiao, *Nat. Commun.*, 2023, **14**, 2843.

169 J. Zhang, T. Fan, P. Huang, X. Lian, Y. Guo, Z. Chen and X. Yi, *Adv. Funct. Mater.*, 2022, **32**, 2113075.

170 Y. Li, J. Li, W. Ai, J. Chen, T. Lu, X. Liao, W. Wang, R. Huang, Z. Chen and J. Wu, *Angew. Chem., Int. Ed.*, 2024, **63**, e202407772.

171 B. Liu, Y. Xie, X. Wang, C. Gao, Z. Chen, J. Wu, H. Meng, Z. Song, S. Du and Z. Ren, *Appl. Catal., B*, 2022, **301**, 120781.

172 W. Yang, C. Si, Y. Zhao, Q. Wei, G. Jia, G. Cheng, J. Qin and Z. Zhang, *Appl. Catal., B*, 2022, **316**, 121619.

173 J. Xue, X. Dong, C. Liu, J. Li, Y. Dai, W. Xue, L. Luo, Y. Ji, X. Zhang and X. Li, *Nat. Commun.*, 2024, **15**, 5998.

174 P. Li, J. Liu, Y. Wang, X. D. Zhang, Y. Hou, Y. Zhang, X. Sun, X. Kang, Q. Zhu and B. Han, *J. Am. Chem. Soc.*, 2024, **146**, 26525–26533.

175 J. Li, M. Wei, B. Ji, S. Hu, J. Xue, D. Zhao, H. Wang, C. Liu, Y. Ye and J. Xu, *Angew. Chem., Int. Ed.*, 2025, e202417008.

176 X. Zhou, A. Zhang, B. Chen, S. Zhu, Y. Cui, L. Bai, J. Yu, Y. Ge, Q. Yun and L. Li, *Adv. Mater.*, 2023, **35**, 2304414.

177 C. Du, J. P. Mills, A. G. Yohannes, W. Wei, L. Wang, S. Lu, J.-X. Lian, M. Wang, T. Guo and X. Wang, *Nat. Commun.*, 2023, **14**, 6142.

178 Y. Yang, J. Zhang, Z. Tan, J. Yang, S. Wang, M. Li and Z. Su, *Angew. Chem., Int. Ed.*, 2024, **136**, e202408873.

179 L. K. Xiong, X. Zhang, H. Yuan, J. Wang, X. Z. Yuan, Y. B. Lian, H. D. Jin, H. Sun, Z. Deng, D. Wang, J. P. Hu, H. M. Hu, J. Choi, J. Li, Y. F. Chen, J. Zhong, J. Guo, M. H. Rummerli, L. Xu and Y. Peng, *Angew. Chem., Int. Ed.*, 2021, **60**, 2508–2518.

180 L. Shang, X. Lv, L. Zhong, S. Li and G. Zheng, *Small Methods*, 2022, **6**, 2101334.

181 Y. Liu, Z. Yue, C. Jin, L. Zheng, J. Shi, D. Li, Y. Wang, J. Bai, K. Leng and W. Wang, *Small*, 2025, 2409259.

7008 | *Chem. Soc. Rev.*, 2025, **54**, 6973–7016

This journal is © The Royal Society of Chemistry 2025

182 M. Xie, Y. Shen, W. Ma, D. Wei, B. Zhang, Z. Wang, Y. Wang, Q. Zhang, S. Xie and C. Wang, *Angew. Chem., Int. Ed.*, 2022, **61**, e202213423.

183 C. Peng, J. Ma, G. Luo, S. Yan, J. Zhang, Y. Chen, N. Chen, Z. Wang, W. Wei and T. K. Sham, *Angew. Chem., Int. Ed.*, 2024, **63**, e202316907.

184 J. Feng, L. Wu, S. Liu, L. Xu, X. Song, L. Zhang, Q. Zhu, X. Kang, X. Sun and B. Han, *J. Am. Chem. Soc.*, 2023, **145**, 9857–9866.

185 J. Zhang, C. Guo, S. Fang, X. Zhao, L. Li, H. Jiang, Z. Liu, Z. Fan, W. Xu, J. Xiao and M. Zhong, *Nat. Commun.*, 2023, **14**, 1298.

186 Y. J. Chen, X. Y. Wang, X. Y. Li, R. K. Miao, J. C. Dong, Z. L. Zhao, C. H. Liu, H. Z. Liu, J. E. Huang, J. H. Wu, S. Chu, C. Yu, J. Yu, W. Y. Ni, P. Y. Wang, R. Xia, P. F. Ou, K. Xie, B. J. Xu, Y. Hou, D. Sinton and E. H. Sargent, *Nat. Catal.*, 2025, 1–9.

187 X. Wang, Y. Chen, F. Li, R. K. Miao, J. E. Huang, Z. Zhao, X.-Y. Li, R. Dorakhan, S. Chu and J. Wu, *Nat. Commun.*, 2024, **15**, 616.

188 D. Wang, H. D. Jung, S. Liu, J. Chen, H. Yang, Q. He, S. Xi, S. Back and L. Wang, *Nat. Commun.*, 2024, **15**, 4692.

189 Z. Wu, N. Meng, R. Yang, M. Chen, J. Pan, S. Chi, C. Wu, S. Xi, Y. Liu and Y. Ou, *Angew. Chem., Int. Ed.*, 2025, **64**, e202420283.

190 W. Ren, X. Tan, C. Jia, A. Krammer, Q. Sun, J. Qu, S. C. Smith, A. Schueler, X. Hu and C. Zhao, *Angew. Chem., Int. Ed.*, 2022, **134**, e202203335.

191 H. Bao, Y. Qiu, X. Peng, J.-A. Wang, Y. Mi, S. Zhao, X. Liu, Y. Liu, R. Cao and L. Zhuo, *Nat. Commun.*, 2021, **12**, 238.

192 Y. Zhao, Z. Shi, F. Li, C. Jia, Q. Sun, Z. Su and C. Zhao, *ACS Catal.*, 2024, **14**, 3926–3932.

193 Y. Li, X. Cao, Q. Chen, R. Pan, J. Zhang, G. Meng, Y. Yang, Y. Li, J. Mao and W. Chen, *Small*, 2024, **20**, 2405367.

194 T. Zheng, K. Jiang, N. Ta, Y. Hu, J. Zeng, J. Liu and H. Wang, *Joule*, 2019, **3**, 265–278.

195 Y. Zhang, F. Chen, X. Y. Yang, Y. R. Guo, X. H. Zhang, H. Dong, W. H. Wang, F. Lu, Z. M. Lu, H. Liu, Y. Xiao and Y. H. Cheng, *Nat. Commun.*, 2025, **16**, 1956.

196 Q. Wang, T. Luo, X. Cao, Y. Gong, Y. Liu, Y. Xiao, H. Li, F. Gröbmeyer, Y. R. Lu and T. S. Chan, *Nat. Commun.*, 2025, **16**, 2985.

197 X. P. Yang, Z. Z. Wu, Y. C. Li, S. P. Sun, Y. C. Zhang, J. W. Duanmu, P. G. Lu, X. L. Zhang, F. Y. Gao and Y. Yang, *Nat. Commun.*, 2025, **16**, 2811.

198 W. Sun, S. Liu, H. Sun, H. Hu, J. Li, L. Wei, Z. Tian, Q. Chen, J. Su and L. Chen, *Adv. Energy Mater.*, 2025, 2500283.

199 X. Wang, W. Ju, L. Liang, M. Riyaz, A. Bagger, M. Filippi, J. Rossmeisl and P. Strasser, *Angew. Chem., Int. Ed.*, 2024, **63**, e202401821.

200 Y. Zang, Y. Liu, R. Lu, Q. Yang, B. Wang, M. Zhang, Y. Mao, Z. Wang and Y. Lum, *Adv. Mater.*, 2025, 2417034.

201 Z. Ma, B. Wang, X. Yang, C. Ma, W. Wang, C. Chen, F. Liang, N. Zhang, H. Zhang and Y. Chu, *J. Am. Chem. Soc.*, 2024, **146**, 29140–29149.

202 X. Lv, Q. Liu, H. Yang, J. Wang, X. Wu, X. Li, Z. Qi, J. Yan, A. Wu and T. Cheng, *Adv. Funct. Mater.*, 2023, **33**, 2301334.

203 Q. Zhang, C. B. Musgrave III, Y. Song, J. Su, L. Huang, L. Cheng, G. Li, Y. Liu, Y. Xin and Q. Hu, *Nat. Synth.*, 2024, **3**, 1231–1242.

204 H. Yang, N. Guo, S. Xi, Y. Wu, B. Yao, Q. He, C. Zhang and L. Wang, *Nat. Commun.*, 2024, **15**, 7703.

205 N. Han, X. Xiong, M. Noufal, B. Weng and A. R. Puente-Santiago, *Chem*, 2025, **11**, 102458.

206 H. Li, H. Li, P. Wei, Y. Wang, Y. Zang, D. Gao, G. Wang and X. Bao, *Energy Environ. Sci.*, 2023, **16**, 1502–1510.

207 Y. Ma, T. Xiao, K. Zhu, W. Zhang, Z. Yin, A. Dong, Z. Sun, D. Zhao and W. Li, *Angew. Chem., Int. Ed.*, 2025, **64**, e202416629.

208 H. Zheng, H. Wu, L. Qiu, M. Yu, J. Zhou, H. Xu, C. Lv, P. Tian, J. Wang and L. Ling, *ACS Appl. Nano Mater.*, 2024, **7**, 27275–27286.

209 F. Wu, S. Q. Wang, S. Kunze, X. P. Gao, P. Q. Yin and Y.-E. Wu, *Rare Met.*, 2024, 1–8.

210 C. Wang, B. Chen, H. Ren, X. Wang, W. Li, H. Hu, X. Chen, Y. Liu, Q. Guan and W. Li, *Appl. Catal., B*, 2025, 125151.

211 X. Chen, S. Jia, J. Zhai, J. Jiao, M. Dong, C. Xue, T. Deng, H. Cheng, Z. Xia and C. Chen, *Nat. Commun.*, 2024, **15**, 7691.

212 Y. Rong, T. Liu, J. Sang, R. Li, P. Wei, H. Li, A. Dong, L. Che, Q. Fu and D. Gao, *Angew. Chem., Int. Ed.*, 2023, **135**, e202309893.

213 J. Yu, J. Xiao, L. Guo, Z. Xie, K. Wang, Y. Wang, F. Hao, Y. Ma, J. Zhou and P. Lu, *ACS Nano*, 2024, **18**, 33602–33613.

214 D. Kim, S. Park, J. Lee, Y. Chen, F. Li, J. Kim, Y. Bai, J. E. Huang, S. Liu and E. D. Jung, *J. Am. Chem. Soc.*, 2024, **146**, 27701–27712.

215 R. Wang, J. Liu, Q. Huang, L. Z. Dong, S. L. Li and Y. Q. Lan, *Angew. Chem., Int. Ed.*, 2021, **60**, 19829–19835.

216 Y. Liang, J. Zhao, Y. Yang, S.-F. Hung, J. Li, S. Zhang, Y. Zhao, A. Zhang, C. Wang and D. Appadoo, *Nat. Commun.*, 2023, **14**, 474.

217 J. Wang, Q. Ji, H. Zang, Y. Zhang, C. Liu, N. Yu and B. Geng, *Adv. Funct. Mater.*, 2024, **34**, 2404274.

218 K. Pellumbi, D. Krisch, C. Rettenmaier, H. Awada, H. Sun, L. Song, S. A. Sanden, L. Hoof, L. Messing and K. Junge Puring, *Cell Rep. Phys. Sci.*, 2023, **4**, 101746.

219 H. Chen, Q. Huang, K. Yang, S. Chen, H. Feng, C. Jia, Q. Li, C. Zhao and J. Duan, *Nano Energy*, 2024, **131**, 110265.

220 M. Li, K. Yang, Y. Sun, T. Gao, Z. Nie, S. Chen, Q. Li and J. Duan, *Adv. Energy Mater.*, 2024, **14**, 2303073.

221 Y. Sun, J. Chen, X. Du, J. Cui, X. Chen, C. Wu, X. Yang, L. Liu and J. Ye, *Angew. Chem., Int. Ed.*, 2024, **136**, e202410802.

222 G. H. Jeong, Y. C. Tan, J. T. Song, G. Y. Lee, H. J. Lee, J. Lim, H. Y. Jeong, S. Won, J. Oh and S. O. Kim, *Chem. Eng. J.*, 2021, **426**, 131063.

223 Y. Chen, J. Zhang, J. Tian, Y. Guo, F. Xu, Y. Zhang, X. Wang, L. Yang, Q. Wu and Z. Hu, *Adv. Funct. Mater.*, 2023, **33**, 2214658.

224 Y. Li, N. M. Adli, W. Shan, M. Wang, M. J. Zachman, S. Hwang, H. Tabassum, S. Karakalos, Z. Feng and G. Wang, *Energy Environ. Sci.*, 2022, **15**, 2108–2119.

225 S. Li, S. Zhao, X. Lu, M. Ceccato, X. M. Hu, A. Roldan, J. Catalano, M. Liu, T. Skrydstrup and K. Daasbjerg, *Angew. Chem., Int. Ed.*, 2021, **60**, 22826–22832.

This journal is © The Royal Society of Chemistry 2025

Chem. Soc. Rev., 2025, **54**, 6973–7016 | 7009

226 C. Wang, Y. Liu, H. Ren, Q. Guan, S. Chou and W. Li, *ACS Catal.*, 2022, **12**, 2513–2521.

227 C. Jia, X. Tan, Y. Zhao, W. Ren, Y. Li, Z. Su, S. C. Smith and C. Zhao, *Angew. Chem., Int. Ed.*, 2021, **60**, 23342–23348.

228 J. Pei, H. Shang, J. Mao, Z. Chen, R. Sui, X. Zhang, D. Zhou, Y. Wang, F. Zhang and W. Zhu, *Nat. Commun.*, 2024, **15**, 416.

229 S. Wang, Z. Qian, Q. Huang, Y. Tan, F. Lv, L. Zeng, C. Shang, K. Wang, G. Wang and Y. Mao, *Adv. Energy Mater.*, 2022, **12**, 2201278.

230 X. Zhang, C. Ling, S. Ren, H. Xi, L. Ji, J. Wang and J. Zhu, *Adv. Mater.*, 2025, **37**, 2413111.

231 T.-U. Wi, Y. Xie, Z. H. Levell, D. Feng, J. Y. T. Kim, P. Zhu, A. Elgazzar, T. H. Jeon, M. Shakouri and S. Hao, *Nat. Synth.*, 2024, **3**, 1392–1403.

232 H. Han, S. Lee, J. Im, M. Lee, T. Lee, S. T. Hyun, J. Hong, T. Seok and D. Choo, *Chem. Eng. J.*, 2024, **479**, 147603.

233 J. d Yi, X. Gao, H. Zhou, W. Chen and Y. Wu, *Angew. Chem., Int. Ed.*, 2022, **61**, e202212329.

234 Q. Fan, X. Zhang, X. Ge, L. Bai, D. He, Y. Qu, C. Kong, J. Bi, D. Ding and Y. Cao, *Adv. Energy Mater.*, 2021, **11**, 2101424.

235 Z. Guo, H. Zhu, Z. Yan, L. Lei, D. Wang, Z. Xi, Y. Lian, J. Yu, K. L. Fow and H. Do, *Appl. Catal., B*, 2025, **364**, 124839.

236 W. Yang, Y. Zhao, Y. Chen, H. Ren, J. Sun, Z. Shi, X. Jin, Z. Zhang and X. Wang, *Angew. Chem., Int. Ed.*, 2025, e202422082.

237 X. Wang, Z. Jiang, P. Wang, Z. Chen, T. Sheng, Z. Wu and Y. Xiong, *Angew. Chem., Int. Ed.*, 2023, **62**, e202313646.

238 H. Zhao, Y. Xie, B. Lv, G. Jing and Y. Li, *Appl. Catal., B*, 2025, 125234.

239 D. Wang, Y. Li, S. Geng, R. Li and K. Chen, *Adv. Funct. Mater.*, 2025, 2503497.

240 L. X. Liu, Y. Cai, H. Du, X. Lu, X. Li, F. Liu, J. Fu and J. J. Zhu, *ACS Appl. Mater.*, 2023, **15**, 16673–16679.

241 H. Zang, Y. Zhao, C. Liu, H. Lu, N. Yu and B. Geng, *Adv. Funct. Mater.*, 2025, 2504400.

242 C. Jia, Y. Zhao, S. Song, Q. Sun, Q. Meyer, S. Liu, Y. Shen and C. Zhao, *Adv. Energy Mater.*, 2023, **13**, 2302007.

243 D. Chen, F. Wang, Y. Liu, W. Lyu, X. Zhao, R. Fang, L. Chen and Y. Li, *Angew. Chem., Int. Ed.*, 2025, e202421149.

244 Y. Shi, J. Li, Z. Min, X. Wang, M. Hou, H. Ma, Z. Zhuang, Y. Qin, Y. Sun and D. Wang, *Sci. China Mater.*, 2025, **68**, 173–179.

245 J. Pei, L. Yang, J. Lin, Z. Zhang, Z. Sun, D. Wang and W. Chen, *Angew. Chem., Int. Ed.*, 2024, **136**, e202316123.

246 N. Zhang and Y. Zhang, *J. Mater. Chem. A*, 2025, **13**, 2902–2910.

247 J. Chen, C. Hu, Y. Liu, Y. Wei, K. Shen, L. Chen and Y. Li, *Angew. Chem., Int. Ed.*, 2025, **64**, e202422775.

248 Z. Xing, X. Hu and X. Feng, *ACS Energy Lett.*, 2021, **6**, 1694–1702.

249 Y. K. Xiao, M. Wang, H. Z. Yang, H. R. Qiu, H. T. Lu, Y. Da, G. W. Chen, T. Y. Jiang, W. W. Fu, B. H. Hu, J. M. Chen, L. Chen, Y. S. Ding, B. H. Cui, C. L. Jiang, Z. J. Sun, Y. Long, H. T. Yang, Z. L. Tian, L. Wang and W. Chen, *Adv. Energy Mater.*, 2024, **14**, 2302556.

250 L. Bian, Z. Y. Zhang, H. Tian, N. N. Tian, Z. Ma and Z. L. Wang, *Chin. J. Catal.*, 2023, **54**, 199–211.

251 M. Wu, D. Huang, F. Lai, R. Yang, Y. Liu, J. Fang, T. Zhai and Y. Liu, *Proc. Natl. Acad. Sci. U. S. A.*, 2023, **120**, e2302851120.

252 W. S. Fang, R. H. Lu, F. M. Li, C. H. He, D. Wu, K. H. Yue, Y. Mao, W. Guo, B. You, F. Song, T. Yao, Z. Y. Wang and B. Y. Xia, *Angew. Chem., Int. Ed.*, 2024, **63**, e202319936.

253 Z. Wei, W. Wang, T. Shao, S. Yang, C. Liu, D. Si, R. Cao and M. Cao, *Angew. Chem., Int. Ed.*, 2024, **6**, e202417066.

254 X. Zheng, Y. Hu, X. Wang, J. Zhu, X. Zhang, T. Sheng and Z. Wu, *Angew. Chem., Int. Ed.*, 2025, **64**, e202415273.

255 Z. Li, B. Sun, D. Xiao, H. Liu, Z. Wang, Y. Liu, Z. Zheng, P. Wang, Y. Dai and B. Huang, *Angew. Chem., Int. Ed.*, 2025, **137**, e202413832.

256 J. J. Lv, M. Jouny, W. Luc, W. Zhu, J. J. Zhu and F. Jiao, *Adv. Mater.*, 2018, **30**, 1803111.

257 Q. Geng, L. Fan, H. Chen, C. Zhang, Z. Xu, Y. Tian, C. Yu, L. Kang, Y. Yamauchi and C. Li, *J. Am. Chem. Soc.*, 2024, **146**, 10599–10607.

258 Y. Kim, G. T. Yun, M. Kim, A. Jamal, I. Gereige, J. W. Ager, W. B. Jung and H. T. Jung, *Angew. Chem., Int. Ed.*, 2024, **63**, e202316264.

259 C. Li, T. Zhang, H. Liu, Z. Guo, Z. Liu, H. Shi, J. Cui, H. Li, H. Li and C. Li, *Adv. Mater.*, 2024, **36**, 2312204.

260 G. Zhang, Z. J. Zhao, D. F. Cheng, H. M. Li, J. Yu, Q. Z. Wang, H. Gao, J. Y. Guo, H. Y. Wang, G. A. Ozin, T. Wang and J. L. Gong, *Nat. Commun.*, 2021, **12**, 5745.

261 J. Q. Xu, S. H. Yang, L. Ji, J. W. Mao, W. Zhang, X. L. Zheng, H. Y. Fu, M. L. Yuan, C. K. Yang, H. Chen and R. X. Li, *Nano Res.*, 2023, **16**, 53–61.

262 Y. P. Zang, T. F. Liu, H. F. Li, P. F. Wei, Y. P. Song, C. F. Cheng, D. F. Gao, Y. F. Song, G. X. Wang and X. H. Bao, *Chem. Eng. J.*, 2022, **446**, 137444.

263 Z. Q. Wang, X. L. Zu, X. D. Li, L. Li, Y. Wu, S. M. Wang, P. Q. Ling, Y. Zhao, Y. F. Sun and Y. Xie, *Nano Res.*, 2022, **15**, 6999–7007.

264 Q. Q. Wu, R. A. Du, P. Wang, G. I. N. Waterhouse, J. Li, Y. C. Qiu, K. Y. Yan, Y. Zhao, W. W. Zhao, H. J. Tsai, M. C. Chen, S. F. Hung, X. Wang and G. X. Chen, *ACS Nano*, 2023, **17**, 12884–12894.

265 H. F. Li, P. F. Wei, T. F. Liu, M. R. Li, C. Wang, R. T. Li, J. Y. Ye, Z. Y. Zhou, S. G. Sun, Q. Fu, D. F. Gao, G. X. Wang and X. H. Bao, *Nat. Commun.*, 2024, **15**, 4603.

266 S. H. Ruan, B. Zhang, J. H. Zou, W. F. Zhong, X. Y. He, J. H. Lu, Q. H. Zhang, Y. Wang and S. J. Xie, *Chin. J. Catal.*, 2022, **43**, 3161–3169.

267 T. T. Zhuang, Z. Q. Liang, A. Seifitokaldani, Y. Li, P. De Luna, T. Burdyny, F. L. Che, F. Meng, Y. M. Min, R. Quintero-Bermudez, C. T. Dinh, Y. J. Pang, M. Zhong, B. Zhang, J. Li, P. N. Chen, H. Y. Liang, W. N. Ge, B. J. Ye, D. Sinton, S. H. Yu and E. H. Sargent, *Nat. Catal.*, 2018, **1**, 421–428.

268 Y. Qiao, S. Shen, C. Mao, Y. Xiao, W. Lai, Y. Wang, X. Zhong, Y. Lu, J. Li and J. Ge, *Angew. Chem., Int. Ed.*, 2024, e202424248.

269 Y.-C. Zhang, X.-L. Zhang, Z.-Z. Wu, Z.-Z. Niu, L.-P. Chi, F.-Y. Gao, P.-P. Yang, Y.-H. Wang, P.-C. Yu and J.-W. Duanmu, *Proc. Natl. Acad. Sci. U. S. A.*, 2024, **121**, e2400546121.

7010 | *Chem. Soc. Rev.*, 2025, **54**, 6973–7016

This journal is © The Royal Society of Chemistry 2025

270 Y. H. Wang, Z. Y. Wang, C. T. Dinh, J. Li, A. Ozden, M. G. Kibria, A. Seifitokaldani, C. S. Tan, C. M. Gabardo, M. C. Luo, H. Zhou, F. W. Li, Y. Lum, C. McCallum, Y. Xu, M. X. Liu, A. Proppe, A. Johnston, P. Todorovic, T. T. Zhuang, D. Sinton, S. O. Kelley and E. H. Sargent, Nat. Catal., 2020, 3, 98–106.

271 Z. Z. Wu, X. L. Zhang, Z. Z. Niu, F. Y. Gao, P. P. Yang, L. P. Chi, L. Shi, W. S. Wei, R. Liu, Z. Chen, S. J. Hu, X. Zheng and M. R. Gao, J. Am. Chem. Soc., 2022, 144, 259–269.

272 W. Ma, S. Xie, B. Zhang, X. He, X. Liu, B. Mei, F. Sun, Z. Jiang, L. Lin and Q. Zhang, Chem, 2023, 9, 2161–2177.

273 J. P. Jiao, X. C. Kang, J. H. Yang, S. Q. Jia, X. Chen, Y. G. Peng, C. J. Chen, X. Q. Xing, Z. J. Chen, M. Y. He, H. H. Wu and B. X. Han, Angew. Chem., Int. Ed., 2024, 63, e202409563.

274 Z. Y. Zhai, D. L. Li, X. Lu, H. Z. Cai, Q. Hu, H. P. Yang and C. X. He, Carbon Energy, 2024, 6, e648.

275 Z. Li, W. Wei, X. Hu, Z. Zhang, Y. Hu, Y. Wu, Y. Wang, J. Xu and M. Ding, Adv. Funct. Mater., 2024, 2422898.

276 Y. L. Xing, H. H. Chen, Y. Liu, Y. L. Sheng, J. Zeng, Z. G. Geng and J. Bao, Chem. Commun., 2021, 57, 1502–1505.

277 L. Fan, C. Xia, P. Zhu, Y. Y. Lu and H. T. Wang, Nat. Commun., 2020, 11, 3633.

278 W. Z. Niu, Z. Chen, W. Guo, W. Mao, Y. Liu, Y. N. Guo, J. Z. Chen, R. Huang, L. Kang, Y. W. Ma, Q. S. Yan, J. Y. Ye, C. Y. Cui, L. Q. Zhang, P. Wang, X. Xu and B. Zhang, Nat. Commun., 2023, 14, 4882.

279 Z.-Z. Niu, L.-P. Chi, Z.-Z. Wu, P.-P. Yang, M.-H. Fan and M.-R. Gao, Natl. Sci. Open, 2023, 2, 20220044.

280 D. Zhong, Q. Fang, R. Du, Y. Jin, C. Peng, D. Cheng, T. Li, T. Zhao, S. Zhang and Y. Zheng, Angew. Chem., Int. Ed., 2025, e202501773.

281 Z. Wang, L. Xu, Y. Zhou, Y. Liang, J. Yang, D. Wu, S. Zhang, X. Han, X. Shi and J. Li, Chem. Soc. Rev., 2024, 53, 6295–6321.

282 M. G. Kibria, C. T. Dinh, A. Seifitokaldani, P. De Luna, T. Burdyny, R. Quintero-Bermudez, M. B. Ross, O. S. Bushuyev, F. P. G. de Arguer, P. D. Yang, D. Sinton and E. H. Sargen, Adv. Mater., 2018, 30, 1804867.

283 C. Long, K. Wan, Y. Chen, L. Li, Y. Jiang, C. Yang, Q. Wu, G. Wu, P. Xu and J. Li, J. Am. Chem. Soc., 2024, 146, 4632–4641.

284 H. Li, T. Liu, P. Wei, L. Lin, D. Gao, G. Wang and X. Bao, Angew. Chem., Int. Ed., 2021, 60, 14329–14333.

285 Y. L. Jiang, H. B. Li, C. J. Chen, Y. Zheng and S. Z. Qiao, ACS Catal., 2024, 14, 8310–8316.

286 R. M. Cai, M. Z. Sun, F. Yang, D. Y. Gu, M. Ju, Y. P. Chen, M. D. Gu, B. L. Huang and S. H. Yang, Chem, 2024, 10, 211–233.

287 X. Z. Lv, Q. Liu, J. H. Wang, X. J. Wu, X. T. Li, Y. Yang, J. H. Yan, A. J. Wu and H. B. Wu, Appl. Catal., B, 2023, 324, 122272.

288 R. A. Du, Q. Q. Wu, S. Y. Zhang, P. Wang, Z. J. Li, Y. C. Qiu, K. Y. Yan, G. I. N. Waterhouse, P. Wang, J. Li, Y. Zhao, W. W. Zhao, X. Wang and G. X. Chen, Small, 2023, 19, 2301289.

289 X. Y. He, L. Lin, X. Y. Li, M. Z. Zhu, Q. H. Zhang, S. J. Xie, B. B. Mei, F. F. Sun, Z. Jiang, J. Cheng and Y. Wang, Nat. Commun., 2024, 15, 9923.

290 K. H. Yue, Y. Y. Qin, H. H. Huang, Z. R. Lv, M. Z. Cai, Y. Q. Su, F. Q. Huang and Y. Yan, Nat. Commun., 2024, 15, 7820.

291 H. Y. Jing, K. R. Lu, J. X. Li, Z. D. Wu, X. F. Xia, M. Z. Xia, B. Y. Liu, C. Su, C. Liu, J. Lei, W. Lei and Q. L. Hao, Appl. Catal., B, 2025, 365, 124977.

292 Z. N. Zhang, Q. Fang, X. Yang, S. W. Zuo, T. Cheng, Y. Yamauchi and J. Tang, Adv. Mater., 2025, 2411498.

293 Q. Sun, X. Tan, C. Jia, C. L. Rong, S. H. Wang, C. Han, Y. Xiao, H. Q. Qi, S. C. Smith and C. Zhao, Adv. Funct. Mater., 2024, 34, 2406281.

294 R. R. Zhang, H. B. Ma, S. H. Han, Z. T. Wu, X. Zhou, Z. X. Chen, J. Liu, Y. K. Xiao, W. Chen and K. P. Loh, Angew. Chem., Int. Ed., 2025, e202421860.

295 J. Liu, P. Li, S. Jia, Y. Wang, L. Jing, Z. Liu, J. Zhang, Q. Qian, X. Kang and X. Sun, Nat. Synth., 2025, 1–14.

296 W. H. Guo, S. W. Zhang, J. J. Zhang, H. R. Wu, Y. B. Ma, Y. Song, L. Cheng, L. Chang, G. Li, Y. Liu, G. D. Wei, L. Gan, M. H. Zhu, S. B. Xi, X. Wang, B. I. Yakobson, B. Z. Tang and R. Q. Ye, Nat. Commun., 2023, 14, 7383.

297 J. Jang, K. Lee, H. Shin, H. S. Lee, B. H. Lee, J. Jeong, J. Kim, W. Hwang, S. Park, M. S. Bootharaju, S. Back, J. Shim, J. H. Kim, T. Hyeon and Y. E. Sung, J. Mater. Chem. A, 2023, 11, 19066–19073.

298 Z. J. Yan, M. Liu, Z. Y. Guo, Q. H. Chen, Z. Y. Xi, X. Z. Sun, J. H. Yu and T. Wu, Adv. Funct. Mater., 2025, 2420493.

299 M. Esmaeilirad, Z. Jiang, A. M. Harzandi, A. Kondori, M. T. Saray, C. U. Segre, R. Shahbazian-Yassar, A. M. Rappe and M. Asadi, Nat. Energy, 2023, 8, 891–900.

300 B. S. Crandall, M. Naughton, S. Park, J. Yu, C. Y. Zhang, S. Mahtabian, K. Y. Wang, X. H. Liang, K. Fu and F. Jiao, Nat. Commun., 2024, 15, 1–9.

301 J. E. Huang, F. W. Li, A. Ozden, A. S. Rasouli, F. P. G. de Arquer, S. J. Liu, S. Z. Zhang, M. C. Luo, X. Wang, Y. W. Lum, Y. Xu, K. Bertens, R. K. Miao, C. T. Dinh, D. Sinton and E. H. Sargent, Science, 2021, 372, 1074–1078.

302 H. Wu, L. Huang, J. Timoshenko, K. Qi, W. Wang, J. Liu, Y. Zhang, S. Yang, E. Petit and V. Flaud, Nat. Energy, 2024, 9, 422–433.

303 Y. Zhao, X. L. Zu, R. H. Chen, X. D. Li, Y. W. Jiang, Z. Q. Wang, S. M. Wang, Y. Wu, Y. F. Sun and Y. Xie, J. Am. Chem. Soc., 2022, 144, 10446–10454.

304 H. Cai, H. Yang, D. Li, S. He, X. Zhang, Q. Hu and C. He, Angew. Chem., Int. Ed., 2025, e202425325.

305 C. J. Chen, L. S. Huang, Y. L. Jiang, Y. Zheng and S. Z. Qiao, Nano Energy, 2024, 126, 109656.

306 T. Zhao, X. Zong, J. Liu, J. Chen, K. Xu, X. Wang, X. Chen, W. Yang, F. Liu and M. Yu, Appl. Catal., B, 2024, 340, 123281.

307 S. Ren, X. Cao, Q. K. Fan, Z. M. Yang, F. Wang, X. Wang, L. C. Bai and J. Yang, Nano-Micro Lett., 2024, 16, 262.

308 Y. Wu, C. Chen, S. Liu, Q. Qian, Q. Zhu, R. Feng, L. Jing, X. Kang, X. Sun and B. Han, Angew. Chem., Int. Ed., 2024, 63, e202410659.

This journal is © The Royal Society of Chemistry 2025

Chem. Soc. Rev., 2025, 54, 6973–7016 | 7011

309 E. Shirzadi, Q. Jin, A. S. Zeraati, R. Dorakhan, T. J. Goncalves, J. Abed, B. H. Lee, A. S. Rasouli, J. Wicks and J. Zhang, *Nat. Commun.*, 2024, **15**, 2995.

310 X. Kong, J. Zhao, Z. Xu, Z. Wang, Y. Wu, Y. Shi, H. Li, C. Ma, J. Zeng and Z. Geng, *J. Am. Chem. Soc.*, 2023, **145**, 14903–14911.

311 S. Chen, C. Ye, Z. Wang, P. Li, W. Jiang, Z. Zhuang, J. Zhu, X. Zheng, S. Zaman and H. Ou, *Angew. Chem., Int. Ed.*, 2023, **135**, e202315621.

312 J. Zhu, J. Li, R. Lu, R. Yu, S. Zhao, C. Li, L. Lv, L. Xia, X. Chen and W. Cai, *Nat. Commun.*, 2023, **14**, 4670.

313 M. Ma, L. Xiong, Y. Dong, Q. Bai, W. Hua, Z. Zheng, F. Lyu, Y. Lian, Z. Wei and H. Yuan, *Adv. Funct. Mater.*, 2024, **34**, 2315667.

314 H. Guo, Q. Huang, D. Li, S. Dai, K. Yang, S. Chen, W. Ma, Q. Li and J. Duan, *J. Mater. Chem. A*, 2025, **13**, 348–355.

315 L. Ma, Q. H. Geng, L. L. Fan, J. X. Li, D. W. Du, J. L. Bai and C. L. Li, *Nano Res.*, 2023, **16**, 9065–9072.

316 F. W. Li, A. Thevenon, A. Rosas-Hernandez, Z. Y. Wang, Y. L. Li, C. M. Gabardo, A. Ozden, C. T. Dinh, J. Li, Y. H. Wang, J. P. Edwards, Y. Xu, C. McCallum, L. Z. Tao, Z. Q. Liang, M. C. Luo, X. Wang, H. H. Li, C. P. O'Brien, C. S. Tan, D. H. Nam, R. Quintero-Bermudez, T. T. Zhuang, Y. G. C. Li, Z. J. Han, R. D. Britt, D. Sinton, T. Agapie, J. C. Peters and E. H. Sargent, *Nature*, 2020, **577**, 509–513.

317 C. Lu, Q. He, S. Huang, P. Shi, C. Yang, J. Zhang, J. Zhu, J. Zhang, T. Wang and X. Zhuang, *Adv. Mater.*, 2024, **9**, 2415092.

318 Z. Y. Du, S. B. Li, G. H. Liang, Y. M. Xie, Y. L. A, Y. Zhang, H. Zhang, J. H. Tian, S. S. Zheng, Q. N. Zheng, Z. Chen, W. F. Ip, J. X. Liu and J. F. Li, *J. Am. Chem. Soc.*, 2024, **146**, 32870–32879.

319 J. Kim, T. Lee, H. D. Jung, M. Kim, J. Eo, B. Kang, H. Jung, J. Park, D. Bae, Y. Lee, S. Park, W. Kim, S. Back, Y. Lee and D. H. Nam, *Nat. Commun.*, 2024, **15**, 192.

320 Y. H. Li, R. Z. Chen, J. Z. Liu, L. Cheng, J. W. Zhao, Y. Lu, J. Q. Feng, Z. M. Gong and C. Z. Li, *Chem. Eng. Sci.*, 2023, **267**, 118354.

321 Z. J. J. Zhu, Y. H. Zhu, Z. X. Ren, D. Liu, F. Y. Yue, D. F. Sheng, P. P. Shao, X. Y. Huang, X. Feng, A. X. Yin, J. Xie and B. Wang, *J. Am. Chem. Soc.*, 2024, **146**, 1572–1579.

322 M. W. Fang, X. Miao, Z. H. Huang, M. L. Wang, X. C. Feng, Z. W. Wang, Y. Zhu, L. M. Dai and L. Jiang, *J. Am. Chem. Soc.*, 2024, **146**, 27060–27069.

323 X. L. Zhou, J. Q. Shan, M. Zheng, H. Li, B. Y. Xia and Y. Zheng, *Sci. China Mater.*, 2024, **67**, 1858–1865.

324 Y. Pan, X. Q. Li, G. Y. Duan, J. Fang and B. H. Xu, *Appl. Catal., B*, 2025, **361**, 124681.

325 T. Zhang, Z. Li, A. K. Ummireddi and J. Wu, *Trends Chem.*, 2023, **5**, 252–266.

326 Q. Qin, H. Suo, L. Chen, Y. X. Wang, J. Z. Wang, H. K. Liu, S. X. Dou, M. Lao and W. H. Lai, *Adv. Mater. Interfaces*, 2024, **11**, 2301049.

327 Y. Ma, J. Yu, M. Sun, B. Chen, X. Zhou, C. Ye, Z. Guan, W. Guo, G. Wang and S. Lu, *Adv. Mater.*, 2022, **34**, 2110607.

328 C. Morales-Guio, K. P. Kuhl, A. Jackson, N. C. Johnson, D. N. Abram, T. Hatsukade, C. Hahn and T. F. Jaramillo, *Nat. Catal.*, 2018, **1**, 764–771.

329 J. Monzó, Y. Malewski, R. Kortlever, F. J. Vidal-Iglesias, J. Solla-Gullón, M. Koper and P. Rodriguez, *J. Mater. Chem. A*, 2015, **3**, 23690–23698.

330 Y. Chen, X.-Y. Li, Z. Chen, A. Ozden, J. E. Huang, P. Ou, J. Dong, J. Zhang, C. Tian and B.-H. Lee, *Nat. Nanotechnol.*, 2024, **19**, 311–318.

331 M. Liu, Q. Wang, T. Luo, M. Herran, X. Cao, W. Liao, L. Zhu, H. Li, A. Stefancu and Y.-R. Lu, *J. Am. Chem. Soc.*, 2023, **146**, 468–475.

332 X. Kong, J. Zhao, J. Ke, C. Wang, S. Li, R. Si, B. Liu, J. Zeng and Z. Geng, *Nano Lett.*, 2022, **22**, 3801–3808.

333 F.-Z. Li, H.-G. Qin, H.-L. Zhang, X. Yue, L.-K. Fu, B. Xu, M. Lin and J. Gu, *Joule*, 2024, **8**, 1772–1789.

334 M. Alfath and C. W. Lee, *Catalysts*, 2020, **10**, 859.

335 Y. Lin, C. Xia, Z. Zhu, J. Wang, H. Niu, S. Gong, Z. Li, N. Yang, J. Song Chen and R. Wu, *Angew. Chem., Int. Ed.*, 2024, **137**, e202414569.

336 C. Wei, Y. Yang, H. Ma, G. Sun, X. Wang, Y. Cheng, C. Zhang, B. S. Yeo, C. He and A. B. Wong, *Adv. Funct. Mater.*, 2023, **33**, 2214992.

337 B. Yang, J. Zeng, Z. Zhang, L. Meng, D. Shi, L. Chen and Y. Huang, *J. Energy Chem.*, 2024, **90**, 233–243.

338 Q. Sun, W. H. Ren, Y. Zhao and C. Zhao, *Chem. Commun.*, 2021, **57**, 1514–1517.

339 H. Y. Li, L. Z. Fang, T. Wang, R. Bai, J. Zhang, T. Li, Z. Y. Duan, K. J. Chen and F. P. Pan, *Adv. Mater.*, 2024, 2416337.

340 B. T. Chen, B. R. Li, Z. Q. Tian, W. B. Liu, W. P. Liu, W. W. Sun, K. Wang, L. Chen and J. Z. Jiang, *Adv. Energy Mater.*, 2021, **11**, 2102152.

341 Q. R. Wei, J. Y. Qin, G. X. Jia, Y. Zhao, Z. Y. Guo, G. H. Cheng, W. S. Ma, W. F. Yang and Z. H. Zhang, *J. Phys. Chem. Lett.*, 2022, **13**, 9058–9065.

342 Z. Wang, D. Liu, C. Xia, X. Shi, Y. Zhou, Q. Liu, J. Huang, H. Wu, D. Zhu and S. Zhang, *Nat. Commun.*, 2025, **16**, 1754.

343 X. Liu, S. Li, A. Chen, X. Dong, J. Mao, C. Zhu, G. Wu, Y. Wei, J. Xia and H. Zhu, *ACS Catal.*, 2025, **15**, 4259–4269.

344 A. H. Chen, X. Dong, J. N. Mao, W. Chen, C. Zhu, S. J. Li, G. F. Wu, Y. H. Wei, X. H. Liu, G. H. Li, Y. F. Song, Z. Jiang, W. Wei and Y. H. Sun, *Appl. Catal., B*, 2023, **333**, 122768.

345 Y. Wei, Y. Song, C. Zhu, J. Mao, A. Chen, G. Feng, G. Wu, X. Liu, S. Li and G. Li, *The Innovation*, 2025, **6**, 100844.

346 Y. Wei, X. Wang, J. Mao, Y. Song, H. Zhu, X. Liu, C. Luo, S. Li, A. Chen and G. Li, *Angew. Chem., Int. Ed.*, 2025, **137**, e202423370.

347 J. Xia, S. Li, X. Liu, X. Dong, J. Mao, A. Chen, H. Zhu, X. Wang, Z. Xu and Y. Wei, *Appl. Catal., B*, 2025, **371**, 125202.

348 C. Zhu, G. F. Wu, A. H. Chen, G. H. Feng, X. Dong, G. H. Li, S. J. Li, Y. F. Song, W. Wei and W. Chen, *Energy Environ. Sci.*, 2024, **17**, 510–517.

349 C. Zhu, G. F. Wu, J. N. Mao, A. H. Chen, Y. H. Zhao, G. H. Feng, Y. H. Wei, X. H. Liu, S. J. Li, G. H. Li, X. Dong, Y. F. Song, W. Wei and W. Chen, *Chem. Eng. J.*, 2024, **485**, 150040.

350 Y. Xie, P. F. Ou, X. Wang, Z. Y. Xu, Y. C. Li, Z. Y. Wang, J. E. Huang, J. Wicks, C. McCallum, N. Wang, Y. H. Wang,

7012 | *Chem. Soc. Rev.*, 2025, **54**, 6973–7016

This journal is © The Royal Society of Chemistry 2025

T. X. Chen, B. T. W. Lo, D. Sinton, J. C. Yu, Y. Wang and E. H. Sargent, *Nat. Catal.*, 2022, **5**, 564–570.

351 D. H. Nam, O. Shekhah, A. Ozden, C. McCallum, F. Li, X. Wang, Y. Lum, T. Lee, J. Li and J. Wicks, *Adv. Mater.*, 2022, **34**, 2207088.

352 M. Y. Fan, J. E. Huang, R. K. Miao, Y. Mao, P. F. Ou, F. Li, X. Y. Li, Y. F. Cao, Z. S. Zhang, J. Q. Zhang, Y. Yan, A. Ozden, W. Y. Ni, Y. Wang, Y. Zhao, Z. Chen, B. Khatir, C. P. O'Brien, Y. Xu, Y. C. Xiao, G. I. N. Waterhouse, K. Golovin, Z. Y. Wang, E. H. Sargent and D. Sinton, *Nat. Catal.*, 2023, **6**, 763–772.

353 Y. Zhao, L. Hao, A. Ozden, S. J. Liu, R. K. Miao, P. F. Ou, T. Alkayyali, S. Z. Zhang, J. Ning, Y. X. Liang, Y. Xu, M. Y. Fan, Y. J. Chen, J. E. Huang, K. Xie, J. Q. Zhang, C. P. O'Brien, F. W. Li, E. H. Sargent and D. Sinton, *Nat. Synth.*, 2023, **2**, 403–412.

354 Y. Cao, Z. Chen, P. Li, A. Ozden, P. Ou, W. Ni, J. Abed, E. Shirzadi, J. Zhang and D. Sinton, *Nat. Commun.*, 2023, **14**, 2387.

355 F. Li, Y. C. Li, Z. Wang, J. Li, D.-H. Nam, Y. Lum, M. Luo, X. Wang, A. Ozden and S.-F. Hung, *Nat. Catal.*, 2020, **3**, 75–82.

356 M. Luo, Z. Wang, Y. C. Li, J. Li, F. Li, Y. Lum, D.-H. Nam, B. Chen, J. Wicks and A. Xu, *Nat. Commun.*, 2019, **10**, 5814.

357 L. Yuan, Q. Q. Wan, W. X. Jiang, J. B. Hou, X. D. Zhuang, J. L. Zhang and C. C. Ke, *Electrochim. Acta*, 2024, **475**, 143662.

358 T. Shao, K. Yang, S. Chen, M. Zheng, Y. Zhang, Q. Li and J. Duan, *Carbon Energy*, 2024, **6**, e416.

359 X. Zhang, X. Yan, P. Chen, P. Zhang, X. Kang, J. Ma, C. Chen and B. Han, *Angew. Chem., Int. Ed.*, 2024, **136**, e202315822.

360 Y. Lin, T. Wang, L. L. Zhang, G. Zhang, L. L. Li, Q. F. Chang, Z. F. Pang, H. Gao, K. Huang, P. Zhang, Z. J. Zhao, C. L. Pei and J. L. Gong, *Nat. Commun.*, 2023, **14**, 3575.

361 T. H. Pham, J. Zhang, M. Li, T. H. Shen, Y. Ko, V. Tileli, W. Luo and A. Züttel, *Adv. Energy Mater.*, 2022, **12**, 2103663.

362 L. Su, Q. Hua, G. Feng, Y. Yang, H. Mei, Y. Yu, X. Chang and Z. Huang, *Adv. Funct. Mater.*, 2025, 2425636.

363 J. Liu, B. Zhang, D. R. Chen, O. W. Peng, H. B. Ma, S. B. Xi, C. Wu, Q. K. Hu, K. Zhang, J. Y. Feng and K. P. Loh, *Angew. Chem., Int. Ed.*, 2024, **63**, e202412266.

364 W. W. Fu, Y. K. Li, J. Y. Chen, J. Y. Chen, S. B. Xi, J. Zhang and L. Wang, *Angew. Chem., Int. Ed.*, 2024, **63**, e202407992.

365 Y. C. Yao, T. Shi, W. X. Chen, J. H. Wu, Y. Y. Fan, Y. C. Liu, L. Cao and Z. Chen, *Nat. Commun.*, 2024, **15**, 1257.

366 H. L. Wu, J. Li, K. Qi, Y. Zhang, E. Petit, W. S. Wang, V. Flaud, N. Onofrio, B. Rebiere, L. Q. Huang, C. Salameh, L. Lajaunie, P. Miele and D. Voiry, *Nat. Commun.*, 2021, **12**, 7210.

367 Y. Wang, Y. Cheng, S. Liu, Y. Yin, J. Yang, H. Wang, K. Li, M. Zhou, J. Jiao and P. Zhang, *Angew. Chem., Int. Ed.*, 2025, e202420661.

368 J. H. Bi, P. S. Li, J. Y. Liu, S. Q. Jia, Y. Wang, Q. G. Zhu, Z. M. Liu and B. X. Han, *Nat. Commun.*, 2023, **14**, 2823.

369 X. W. Du, P. Zhang, G. Zhang, H. Gao, L. L. Zhang, M. M. Zhang, T. Wang and J. L. Gong, *Natl. Sci. Rev.*, 2024, **11**, nwad149.

370 W. Z. Li, Z. L. Yin, Z. Y. Gao, G. W. Wang, Z. Li, F. Y. Wei, X. Wei, H. Q. Peng, X. T. Hu, L. Xiao, J. T. Lu and L. Zhuang, *Nat. Energy*, 2022, **7**, 835–843.

371 A. Ozden, F. Li, F. P. García de Arquer, A. Rosas-Hernández, A. Thevenon, Y. Wang, S.-F. Hung, X. Wang, B. Chen and J. Li, *ACS Energy Lett.*, 2020, **5**, 2811–2818.

372 P. Papangelakis, R. K. Miao, R. H. Lu, H. Q. Liu, X. Wang, A. Ozden, S. J. Liu, N. Sun, C. P. O'Brien, Y. F. Hu, M. Shakouri, Q. F. Xiao, M. S. Li, B. Khatir, J. E. Huang, Y. K. Wang, Y. C. Xiao, F. Li, A. S. Zeraati, Q. Zhang, P. Y. Liu, K. Golovin, J. Y. Howe, H. Y. Liang, Z. Y. Wang, J. Li, E. H. Sargent and D. Sinton, *Nat. Energy*, 2024, **9**, 1011–1020.

373 T. Möller, W. Ju, A. Bagger, X. L. Wang, F. Luo, T. N. Thanh, A. S. Varela, J. Rossmeisl and P. Strasser, *Energy Environ. Sci.*, 2019, **12**, 640–647.

374 J. Chen, X. Peng, Z. Li, B. Yang, Q. Zhang, J. Lu, L. Lei and Y. Hou, *Adv. Mater.*, 2024, 2409106.

375 G. Díaz-Sainz, M. Alvarez-Guerra and A. Irabien, *J. CO$_2$ Util.*, 2022, **56**, 101822.

376 X. She, L. Zhai, Y. Wang, P. Xiong, M. M. J. Li, T. S. Wu, M. C. Wong, X. Guo, Z. Xu and H. Li, *Nat. Energy*, 2024, **9**, 81–91.

377 C. P. O'Brien, R. K. Miao, A. Shayesteh Zeraati, G. Lee, E. H. Sargent and D. Sinton, *Chem. Rev.*, 2024, **124**, 3648–3693.

378 K. Yang, M. Li, T. Gao, G. Xu, D. Li, Y. Zheng, Q. Li and J. Duan, *Nat. Commun.*, 2024, **15**, 7060.

379 J. Yu, J. Xiao, Y. Ma, J. Zhou, P. Lu, K. Wang, Y. Yan, J. Zeng, Y. Wang and S. Song, *Chem. Catal.*, 2023, **3**, 100670.

380 Z. F. Yan, J. L. Hitt, Z. C. Zeng, M. A. Hickner and T. E. Mallouk, *Nat. Chem.*, 2021, **13**, 33–40.

381 Y. Xu, J. P. Edwards, S. J. Liu, R. K. Miao, J. E. Huang, C. M. Gabardo, C. P. O'Brien, J. Li, E. H. Sargent and D. Sinton, *ACS Energy Lett.*, 2021, **6**, 809–815.

382 Y. Xu, R. K. Miao, J. P. Edwards, S. J. Liu, C. P. O'Brien, C. M. Gabardo, M. Y. Fan, J. E. Huang, A. Robb, E. H. Sargent and D. Sinton, *Joule*, 2022, **6**, 1333–1343.

383 W. H. Ren, A. N. Xu, K. R. Chan and X. L. Hu, *Angew. Chem., Int. Ed.*, 2022, **61**, e202214173.

384 G. H. Lee, A. S. Rasouli, B. H. Lee, J. Q. Zhang, D. H. Won, Y. C. Xiao, J. P. Edwards, M. G. Lee, E. D. Jung, F. Arabyarmohammadi, H. Z. Liu, I. Grigioni, J. Abed, T. Alkayyali, S. J. Liu, K. Xie, R. K. Miao, S. Park, R. Dorakhan, Y. Zhao, C. P. O'Brien, Z. Chen, D. Sinton and E. Sargent, *Joule*, 2023, **7**, 1277–1288.

385 S. Yuan, R. Y. Wang, R. Xue, L. Z. Wu, G. R. Zhang, H. Y. Li, Q. Wang, J. W. Yin, L. X. Luo, S. Y. Shen, L. An, X. H. Yan and J. L. Zhang, *ACS Energy Lett.*, 2024, **9**, 5945–5954.

386 D. U. Lee, B. Joensen, J. Jenny, V. M. Ehlinger, S. W. Lee, K. Abiose, Y. Xu, A. Sarkar, T. Y. Lin, C. Hahn and T. F. Jaramillo, *ACS Sustainable Chem. Eng.*, 2023, **11**, 16661–16668.

387 L. Lin, X. Y. He, X. G. Zhang, W. C. Ma, B. Zhang, D. Y. Wei, S. J. Xie, Q. H. Zhang, X. D. Yi and Y. Wang, *Angew. Chem., Int. Ed.*, 2023, **62**, e202214959.

388 R. K. Miao, Y. Xu, A. Ozden, A. Robb, C. P. O'Brien, C. M. Gabardo, G. Lee, J. P. Edwards, J. E. Huang,

This journal is © The Royal Society of Chemistry 2025

Chem. Soc. Rev., 2025, **54**, 6973–7016 | 7013

M. Y. Fan, X. Wang, S. J. Liu, Y. Yan, E. H. Sargent and D. Sinton, *Joule*, 2021, **5**, 2742–2753.

389 J. Fan, B. B. Pan, J. L. Wu, C. C. Shao, Z. Y. Wen, Y. C. Yan, Y. H. Wang and Y. G. Li, *Angew. Chem., Int. Ed.*, 2024, **63**, e202317828.

390 P. Zhu, C. Xia, C. Y. Liu, K. Jiang, G. H. Gao, X. Zhang, Y. Xia, Y. J. Lei, H. N. Alshareef, T. P. Senftle and H. T. Wang, *Proc. Natl. Acad. Sci. U. S. A.*, 2021, **118**, e2010868118.

391 X. P. Yan, M. L. Zhang, Y. Z. Chen, Y. H. Wu, R. Z. Wu, Q. Wan, C. X. Liu, T. T. Zheng, R. J. Feng, J. Zhang, C. J. Chen, C. Xia, Q. G. Zhu, X. F. Sun, Q. L. Qian and B. X. Han, *Angew. Chem., Int. Ed.*, 2023, **62**, e202301507.

392 C. M. Zhao, G. Luo, X. K. Liu, W. Zhang, Z. J. Li, Q. Xu, Q. H. Zhang, H. J. Wang, D. M. Li, F. Y. Zhou, Y. T. Qu, X. Han, Z. Z. Zhu, G. Wu, J. Wang, J. F. Zhu, T. Yao, Y. F. Li, H. J. M. Bouwmeester and Y. E. Wu, *Adv. Mater.*, 2020, **32**, 2002382.

393 H. L. Zhu, J. R. Huang, M. D. Zhang, C. Yu, P. Q. Liao and X. M. Chen, *J. Am. Chem. Soc.*, 2024, **146**, 1144–1152.

394 G. Wen, B. Ren, X. Wang, D. Luo, H. Dou, Y. Zheng, R. Gao, J. Gostick, A. Yu and Z. Chen, *Nat. Energy*, 2022, **7**, 978–988.

395 C. P. O'Brien, R. K. Miao, S. J. Liu, Y. Xu, G. Lee, A. Robb, J. E. Huang, K. Xie, K. Bertens, C. M. Gabardo, J. P. Edwards, C. T. Dinh, E. H. Sargent and D. Sinton, *ACS Energy Lett.*, 2021, **6**, 2952–2959.

396 B. Endrödi, A. Samu, E. Kecsenovity, T. Halmágyi, D. Sebök and C. Janáky, *Nat. Energy*, 2021, **6**, 439–448.

397 S. X. Ren, D. Joulié, D. Salvatore, K. Torbensen, M. Wang, M. Robert and C. P. Berlinguette, *Science*, 2019, **365**, 367–369.

398 C. P. O'Brien, D. McLaughlin, T. Boehm, Y. C. Xiao, J. P. Edwards, C. M. Gabardo, M. Bierling, J. Wicks, A. S. Rasouli, J. Abed, D. Young, C. T. Dinh, E. H. Sargent, S. Thiele and D. Sinton, *Joule*, 2024, **8**, 2903–2919.

399 H. Zhang, *Matter*, 2024, **7**, 421–429.

400 S. Overa, B. S. Crandall, B. Shrimant, D. Tian, B. H. Ko, H. Shin, C. Bae and F. Jiao, *Nat. Catal.*, 2022, **5**, 738–745.

401 W. Deng, A. Lee, W. Dai, L. Cherniack, B. S. Crandall, H. Li and F. Jiao, *Nat. Rev. Clean Technol.*, 2025, 1–14.

402 Y. S. Zhou, R. Ganganahalli, S. Verma, H. R. Tan and B. S. Yeo, *Angew. Chem., Int. Ed.*, 2022, **61**, e202202859.

403 T. Moeller, M. Filippi, S. Brueckner, W. Ju and P. Strasser, *Nat. Commun.*, 2023, **14**, 5680.

404 A. Ozden, Y. H. Wang, F. W. Li, M. C. Luo, J. Sisler, A. Thevenon, A. Rosas-Hernández, T. Burdyny, Y. W. Lum, H. Yadegari, T. Agapie, J. C. Peters, E. H. Sargent and D. Sinton, *Joule*, 2021, **5**, 706–719.

405 S. Overa, T. G. Feric, A. H. A. Park and F. Jiao, *Joule*, 2021, **5**, 8–13.

406 J. Zhang, X. S. Kang, Y. C. Yan, X. Ding, L. He and Y. G. Li, *Angew. Chem., Int. Ed.*, 2024, **63**, e202315777.

407 M. G. Lee, S. Kandambeth, X. Y. Li, O. Shekhah, A. Ozden, J. Wicks, P. F. Ou, S. S. Wang, R. Dorakhan, S. Park, P. M. Bhatt, V. S. Kale, D. Sinton, M. Eddaoudi and E. H. Sargent, *J. Am. Chem. Soc.*, 2024, **146**, 14267–14277.

408 M. G. Lee, X. Y. Li, A. Ozden, J. Wicks, P. F. Ou, Y. H. Li, R. Dorakhan, J. K. Y. Lee, H. K. Park, J. W. Yang, B. Chen, J. Abed, R. dos Reis, G. H. Lee, J. E. Huang, T. Peng, Y. H. Chin, D. Sinton and E. H. Sargent, *Nat. Catal.*, 2023, **6**, 310–318.

409 L. Fan, Y. L. Zhao, L. Chen, J. Y. Chen, J. M. Chen, H. Z. Yang, Y. K. Xiao, T. Y. Zhang, J. Y. Chen and L. Wang, *Nat. Catal.*, 2023, **6**, 585–595.

410 S. van Bavel, S. Verma, E. Negro and M. Bracht, *ACS Energy Lett.*, 2020, **5**, 2597–2601.

411 Y. Pu, Y. Wang, G. Y. Wu, X. B. Wu, Y. L. Lu, Y. Y. Yu, N. Chu, X. H. He, D. P. Li, R. J. Zeng and Y. Jiang, *Environ. Sci. Technol.*, 2024, **58**, 7445–7456.

412 T. Haas, R. Krause, R. Weber, M. Demler and G. Schmid, *Nat. Catal.*, 2018, **1**, 32–39.

413 S. Fernández, E. A. Assaf, S. Ahmad, B. D. Travis, J. B. Curley, N. Hazari, M. Z. Ertem and A. J. Miller, *Angew. Chem., Int. Ed.*, 2025, **137**, e202416061.

414 B. S. Crandall, M. Naughton, S. Park, J. Yu, C. Y. Zhang, S. Mahtabian, K. Y. Wang, X. H. Liang, K. Fu and F. Jiao, *Nat. Commun.*, 2024, **15**, 1–9.

415 Z. Y. Wen, M. J. Wang, C. L. Liang, B. J. Fan, Y. C. Yan, J. Fan, N. Han, Y. H. Wang and Y. G. Li, *J. Am. Chem. Soc.*, 2024, **146**, 32575–32581.

416 P. P. Wang, X. Wang, S. Chandra, A. Lielpetere, T. Quast, F. Conzuelo and W. Schuhmann, *Angew. Chem., Int. Ed.*, 2025, e202422882.

417 N. R. Cuellar, C. Scherer, B. Kaçkar, W. Eisenreich, C. Huber, K. Wiesner-Fleischer, M. Fleischer and O. Hinrichsen, *J. CO$_2$ Util.*, 2020, **36**, 263–275.

418 G. Wu, Y. Song, Q. Zheng, C. Long, T. Fan, Z. Yang, X. Huang, Q. Li, Y. Sun and L. Zuo, *Adv. Energy Mater.*, 2022, **12**, 2202054.

419 T. Zheng, M. Zhang, L. Wu, S. Guo, X. Liu, J. Zhao, W. Xue, J. Li, C. Liu, X. Li, Q. Jiang, J. Bao, J. Zeng, T. Yu and C. Xia, *Nat. Catal.*, 2022, **5**, 388–396.

420 E. C. Hann, S. Overa, M. Harland-Dunaway, A. F. Narvaez, D. N. Le, M. L. Orozco-Cárdenas, F. Jiao and R. E. Jinkerson, *Nat. Food*, 2022, **3**, 461–471.

421 A. J. Martín, G. O. Larrazábal and J. Pérez-Ramírez, *Green Chem.*, 2015, **17**, 5114–5130.

422 S. S. He, F. L. Ni, Y. J. Ji, L. E. Wang, Y. Z. Wen, H. P. Bai, G. J. Liu, Y. Zhang, Y. Y. Li, B. Zhang and H. S. Peng, *Angew. Chem., Int. Ed.*, 2018, **57**, 16114–16119.

423 R. Xia, J.-J. Lv, X. Ma and F. Jiao, *J. Catal.*, 2021, **398**, 185–191.

424 J. Li, Z. Y. Wang, C. McCallum, Y. Xu, F. W. Li, Y. H. Wang, C. M. Gabardo, C. T. Dinh, T. T. Zhuang, L. Wang, J. Y. Howe, Y. Ren, E. H. Sargent and D. Sinton, *Nat. Catal.*, 2019, **2**, 1124–1131.

425 W. Lai, Y. Qiao, J. Zhang, Z. Lin and H. Huang, *Energy Environ. Sci.*, 2022, **15**, 3603–3629.

426 S. Verma, S. Lu and P. J. Kenis, *Nat. Energy*, 2019, **4**, 466–474.

427 M. Zeng, W. Fang, Y. Cen, X. Zhang, Y. Hu and B. Y. Xia, *Angew. Chem., Int. Ed.*, 2024, **63**, e202404574.

428 W. Lai, Y. Qiao, Y. Wang and H. Huang, *Adv. Mater.*, 2023, **35**, 2306288.

7014 | *Chem. Soc. Rev.*, 2025, **54**, 6973–7016

This journal is © The Royal Society of Chemistry 2025

429 Y. Wen, C. Zhan, J. Liu, X. Zhuang, S. Liu, T. Yang, W. Liu, X. Liu, C. W. Kao, Y. C. Huang, T. S. Chan, Z. Hu, D. Su, J. Han, N. Chen and X. Huang, *Nat. Nanotechnol.*, 2025, 1–8.

430 L. Li, A. Ozden, S. Guo, F. P. García de Arquer, C. Wang, M. Zhang, J. Zhang, H. Jiang, W. Wang and H. Dong, *Nat. Commun.*, 2021, **12**, 5223.

431 S. You, J. Xiao, S. Liang, W. Xie, T. Zhang, M. Li, Z. Zhong, Q. Wang and H. He, *Energy Environ. Sci.*, 2024, **17**, 5795–5818.

432 L. B. Zhang, J. Q. Feng, S. J. Liu, X. X. Tan, L. M. Wu, S. H. Jia, L. Xu, X. D. Ma, X. N. Song, J. Ma, X. F. Sun and B. X. Han, *Adv. Mater.*, 2023, **35**, 2209590.

433 H. L. Zhu, H. Y. Chen, Y. X. Han, Z. H. Zhao, P. Q. Liao and X. M. Chen, *J. Am. Chem. Soc.*, 2022, **144**, 13319–13326.

434 J. M. Heng, H. L. Zhu, Z. H. Zhao, D. S. Huang, J. Y. Li, P. Q. Liao and X. M. Chen, *Research*, 2022, **2022**, 0008.

435 S. H. Chen, X. B. Zheng, P. Zhu, Y. P. Li, Z. C. Zhuang, H. J. Wu, J. X. Zhu, C. H. Xiao, M. Z. Chen, P. S. Wang, D. S. Wang and Y. L. He, *Angew. Chem., Int. Ed.*, 2024, **63**, e202411591.

436 L. Fan, F. Li, T. Liu, J. E. Huang, R. K. Miao, Y. Yan, S. Feng, C.-W. Tai, S.-F. Hung and H.-J. Tsai, *Nat. Synth.*, 2024, **4**, 262–270.

437 Z. J. Min, C. F. Shao, B. Chang, N. Wang, Y. Zhao, S. Q. Gao, X. G. Zhang, M. H. Fan, S. J. Zhang and J. J. Wang, *Chem. Eng. J.*, 2024, **502**, 157813.

438 D. S. Huang, H. L. Zhu, Z. H. Zhao, J. R. Huang, P. Q. Liao and X. M. Chen, *ACS Catal.*, 2022, **12**, 8444–8450.

439 M. Zhang, S. H. Zhou, W. B. Wei, D. D. Ma, S. G. Han, X. F. Li, X. T. Wu, Q. Xu and Q. L. Zhu, *Chem. Catal.*, 2022, **2**, 3528–3545.

440 X. Jiang, L. Lin, Y. Rong, R. Li, Q. Jiang, Y. Yang and D. Gao, *Nano Res.*, 2023, **16**, 12050–12057.

441 M. Zhang, M. Lu, M. Y. Yang, J. P. Liao, Y. F. Liu, H. J. Yan, J. N. Chang, S. L. Li and Y. Q. Lan, *eScience*, 2023, **3**, 100116.

442 X. Cao, S. Ren, X. Zhang, Q. K. Fan, Q. Q. Chen, J. Yang and J. J. Mao, *Chem*, 2024, **10**, 2089–2102.

443 J. Liu, Y. Wen, W. Yan, Z. Huang, X. Liu, X. Huang, C. Zhan, Y. Zhang, W.-H. Huang, C.-W. Pao, Z. Hu, D. Su, S. Xie, Y. Wang, J. Han, H. Xiong, X. Huang and N. Chen, *Energy Environ. Sci.*, 2025, **18**, 4396–4404.

444 N. Ye, K. Wang, Y. Tan, Z. Qian, H. Guo, C. Shang, Z. Lin, Q. Huang, Y. Liu, L. Li, Y. Gu, Y. Han, C. Zhou, M. Luo and S. Guo, *Nat. Synth.*, 2025, 1–9.

445 N. Han, X. Y. Guo, J. L. Cheng, P. Y. Liu, S. G. Zhang, S. P. Huang, M. R. Rowles, J. Fransaer and S. M. Liu, *Matter*, 2021, **4**, 1720–1734.

446 Y. Ma, M. Sun, H. Xu, Q. Zhang, J. Lv, W. Guo, F. Hao, W. Cui, Y. Wang, J. Yin, H. Wen, P. Lu, G. Wang, J. Zhou, J. Yu, C. Ye, L. Gan, D. Zhang, S. Chu, L. Gu, M. Shao, B. Huang and Z. Fan, *Adv. Mater.*, 2024, **36**, 2402979.

447 K. Liu, P. Lin, J. Li, Y. Liu, M. Wang, H. Cui and S. Yi, *Adv. Funct. Mater.*, 2025, 2424357.

448 J. Yu, J. Wang, Y. Ma, J. Zhou, Y. Wang, P. Lu, J. Yin, R. Ye, Z. Zhu and Z. Fan, *Adv. Funct. Mater.*, 2021, **31**, 2102151.

449 J. Ding, Q. Song, L. Xia, L. Ruan, M. Zhang, C. Ban, J. Meng, J. Ma, Y. Feng, Y. Wang, X. Tao, D. Yu, J. Y. Dai, L. Gan and X. Zhou, *Nano Energy*, 2024, **128**, 109945.

450 Z. Guo, T. Wang, H. Liu, X. Jia, D. Zhang, L. Wei, J. Xu and H. Li, *ACS Catal.*, 2025, **15**, 3173–3183.

451 Z. Guo, Y. Yu, C. Li, E. Campos dos Santos, T. Wang, H. Li, J. Xu, C. Liu and H. Li, *Angew. Chem., Int. Ed.*, 2024, **63**, e202319913.

452 Y. Wang, D. Zhang, B. Sun, X. Jia, L. Zhang, H. Cheng, J. Fan and H. Li, *Angew. Chem., Int. Ed.*, 2024, e202418228.

453 Z. L. Song, L. F. Fan, S. H. Lu, C. Y. Ling, Q. H. Zhou and J. L. Wang, *Nat. Commun.*, 2025, **16**, 1053.

454 N. Han and B. L. Su, *Nat. Sci. Rev.*, 2025, nwaf110.

455 Y. Shen, N. Fang, X. Liu, Y. Ling, Y. Su, T. Tan, F. Chen, H. Lin, B. Zhao, J. Wang, D. Si, X. Xie, Y. Wang, D. Zhou, T. Zhang, R. Cao and C. Wang, *Nat. Commun.*, 2025, **16**, 2073.

456 X. Yang, H. Ding, S. Li, S. Zheng, J. F. Li and F. Pan, *J. Am. Chem. Soc.*, 2024, **146**, 5532–5542.

457 H. Ding, S. Zheng, X. Yang, J. Pan, Z. Chen, M. Zhang, S. Li and F. Pan, *ACS Catal.*, 2024, **14**, 14330–14338.

458 C. X. Cui, Y. Shen, J. R. He, Y. Fu, X. Hong, S. Wang, J. Jiang and Y. Luo, *J. Am. Chem. Soc.*, 2024, **146**, 34551–34559.

459 X. Q. Han, X. D. Wang, M. Y. Xu, Z. Feng, B. W. Yao, P. J. Guo, Z. F. Gao and Z. Y. Lu, *Chin. Phys. Lett.*, 2025, **42**, 027403.

460 Y. N. Xu, J. Li, J. C. Wu, W. Li, Y. Yang, H. Wu, H. Q. Fu, M. Zhu, X. L. Wang, S. Dai, C. Lian, P. F. Liu and H. G. Yang, *Adv. Mater.*, 2025, 2500343.

461 T. Alkayyali, A. S. Zeraati, H. Mar, F. Arabyarmohammadi, S. Saber, R. K. Miao, C. P. O'Brien, H. S. Liu, Z. Xie, G. Y. Wang, E. H. Sargent, N. N. Zhao and D. Sinton, *ACS Energy Lett.*, 2023, **8**, 4674–4683.

462 K. Xie, R. K. Miao, A. Ozden, S. J. Liu, Z. Chen, C. T. Dinh, J. E. Huang, Q. C. Xu, C. M. Gabardo, G. Lee, J. P. Edwards, C. P. O'Brien, S. W. Boettcher, D. Sinton and E. H. Sargent, *Nat. Commun.*, 2022, **13**, 3609.

463 J. P. Edwards, Y. Xu, C. M. Gabardo, C. T. Dinh, J. Li, Z. B. Qi, A. Ozden, E. H. Sargent and D. Sinton, *Appl. Energy*, 2020, **261**, 114305.

464 Y. Yang, F. He, X. Z. Lv, Q. Liu, A. J. Wu, Z. F. Qi and H. B. Wu, *Small Methods*, 2025, **9**, 2400786.

465 X. Zhang, H. X. Lu, Y. Miao, Y. S. Zhang and J. Y. Wang, *J. Environ. Chem. Eng.*, 2024, **12**, 112369.

466 J. Shi, F. Shi, N. Song, J. X. Liu, X. K. Yang, Y. J. Jia, Z. W. Xiao and P. Du, *J. Power Sources*, 2014, **259**, 50–53.

467 J. Jin, J. Wicks, Q. H. Min, J. Li, Y. F. Hu, J. Y. Ma, Y. Wang, Z. Jiang, Y. Xu, R. H. Lu, G. Z. Si, P. Papangelakis, M. Shakouri, Q. F. Xiao, P. F. Ou, X. Wang, Z. Chen, W. Zhang, K. S. Yu, J. Y. Song, X. H. Jiang, P. Qiu, Y. H. Lou, D. Wu, Y. Mao, A. Ozden, C. D. Wang, B. Y. Xia, X. B. Hu, V. P. Dravid, Y. M. Yiu, T. K. Sham, Z. Y. Wang, D. Sinton, L. Q. Mai, E. H. Sargent and Y. J. Pang, *Nature*, 2023, **617**, 724–729.

468 A. S. Zeraati, F. Li, T. Alkayyali, R. Dorakhan, E. Shirzadi, F. Arabyarmohammadi, C. P. O'Brien, C. M. Gabardo, J. A. T. Kong, A. Ozden, M. Zargartalebi, Y. Zhao, L. Z. Fan, P. Papangelakis, D. Kim, S. Park, R. K. Miao, J. P. Edwards, D. Young, A. H. Ip, E. H. Sargent and D. Sinton, *Nat. Synth.*, 2025, **4**, 75–83.

This journal is © The Royal Society of Chemistry 2025

Chem. Soc. Rev., 2025, **54**, 6973–7016 | **7015**

469 A. Ozden, J. Li, S. Kandambeth, X. Y. Li, S. J. Liu, O. Shekhah, P. F. Ou, Y. Z. Finfrock, Y. K. Wang, T. Alkayyali, F. P. G. de Arquer, V. S. Kale, P. M. Bhatt, A. H. Ip, M. Eddaoudi, E. H. Sargent and D. Sinton, *Nat. Energy*, 2023, **8**, 179–190.

470 C. Kim, J. C. Bui, X. Y. Luo, J. K. Cooper, A. Kusoglu, A. Z. Weber and A. T. Bell, *Nat. Energy*, 2021, **6**, 1026–1034.

471 M. Y. Fan, R. K. Miao, P. F. Ou, Y. Xu, Z. Y. Lin, T. J. Lee, S. F. Hung, K. Xie, J. E. Huang, W. Y. Ni, J. Li, Y. Zhao, A. Ozden, C. P. O'Brien, Y. J. Chen, Y. C. Xiao, S. J. Liu, J. Wicks, X. Wang, J. Abed, E. Shirzadi, E. H. Sargent and D. Sinton, *Nat. Commun.*, 2023, **14**, 3314.

472 C. L. Rong, S. H. Wang, X. Shen, C. Jia, Q. Sun, Q. Zhang and C. Zhao, *Energy Environ. Sci.*, 2024, **17**, 4196–4204.

473 N. Han, X. Zhang, C. Zhang, S. H. Feng, W. Zhang, W. Guo, R. T. Zheng, R. J. Zheng, P. Y. Liu, Y. Li, J. Fransaer and B. L. Su, *Matter*, 2024, **7**, 1330–1343.

474 C. L. Rong, X. J. Shen, Y. Wang, L. Thomsen, T. W. Zhao, Y. B. Li, X. Y. Lu, R. Amal and C. Zhao, *Adv. Mater.*, 2022, **34**, 2110103.

475 C. L. Rong, K. Dastafkan, Y. Wang and C. Zhao, *Adv. Mater.*, 2023, **35**, 2211884.

476 N. Han, S. H. Feng, Y. Liang, J. Wang, W. Zhang, X. L. Guo, Q. R. Ma, Q. Liu, W. Guo, Z. Y. Zhou, S. J. Xie, K. Wan, Y. Z. Jiang, A. Vlad, Y. Z. Guo, E. M. Gaigneaux, C. Zhang, J. Fransaer and X. Zhang, *Adv. Funct. Mater.*, 2023, **33**, 2208399.

477 N. Han, W. Zhang, W. Guo, H. Pan, B. Jiang, L. B. Xing, H. Tian, G. X. Wang, X. Zhang and J. Fransaer, *Nano-Micro Lett.*, 2023, **15**, 185.

478 X. Li, Q. S. Chen, W. Sun, C. C. He and Z. H. Wen, *Angew. Chem., Int. Ed.*, 2024, **63**, e202412410.

479 H. Yadegari, A. Ozden, T. Alkayyali, V. Soni, A. Thevenon, A. Rosas-Hernández, T. Agapie, J. C. Peters, E. H. Sargent and D. Sinton, *ACS Energy Lett.*, 2021, **6**, 3538–3544.

480 B. van den Bosch, B. Rawls, M. B. Brands, C. Koopman, M. F. Phillips, M. C. Figueiredo and G. J. M. Gruter, *ChemPlusChem*, 2023, **88**, e202300112.

481 X. Y. Tan, C. Yu, Y. W. Ren, S. Cui, W. B. Li and J. S. Qiu, *Energy Environ. Sci.*, 2021, **14**, 765–780.

482 H. Xiong, D. Wu, R. Jiang, H. Li, Q. Hu, X. Lu, B. Xu and Q. Lu, *Angew. Chem., Int. Ed.*, 2025, e202504782.

483 A. N. Biswas, Z. H. Xie, R. Xia, S. Overa, F. Jiao and J. G. Chen, *ACS Energy Lett.*, 2022, **7**, 2904–2910.

484 H. Wu, H. Yu, Y. L. Chow, P. A. Webley and J. Zhang, *Adv. Mater.*, 2024, **36**, 2403217.

485 W. Wu, L. Xu, Q. Lu, J. Sun, Z. Xu, C. Song, J. C. Yu and Y. Wang, *Adv. Mater.*, 2025, **37**, 2312894.

486 X. Lu, C. S. Zhou, R. S. Delima, E. W. Lees, A. Soni, D. J. Dvorak, S. X. Ren, T. X. Ji, A. Bahi, F. Ko and C. P. Berlinguette, *Nat. Chem.*, 2024, **16**, 979–987.

487 Y. H. Qu, K. C. Yang, W. Z. Li, G. Z. Wang, L. Xiao, G. W. Wang and L. Zhuang, *ACS Energy Lett.*, 2024, **9**, 3042–3048.

488 Y. D. Sun, F. H. Bai, J. P. Liu, S. Q. Sun, Y. L. Mao, X. J. Liu, Y. Huang and Y. H. Chen, *J. Phys. Chem. Lett.*, 2024, **15**, 9122–9128.

489 H. Warkentin, C. P. O'Brien, S. Holowka, B. Maxwell, M. Awara, M. Bouman, A. S. Zeraati, R. Nicholas, A. H. Ip, E. S. Elsawhi, C. M. Gabardo and D. Sinton, *ChemSusChem*, 2023, **16**, e202300657.

490 J. Disch, L. Bohn, S. Koch, M. Schulz, Y. Y. Han, A. Tengattini, L. Helfen, M. Breitwieser and S. Vierrath, *Nat. Commun.*, 2022, **13**, 6099.

491 D. Shin, H. Karasu, K. Jang, C. Kim, K. Kim, D. Kim, Y. J. Sa, K. B. Lee, K. H. Chae, I. Moon, D. H. Won, J. Na and U. Lee, *ACS Catal.*, 2025, **15**, 2158–2170.

492 S. Hao, A. Elgazzar, N. Ravi, T.-U. Wi, P. Zhu, Y. Feng, Y. Xia, F.-Y. Chen, X. Shan and H. Wang, *Nat. Energy*, 2025, 1–12.

493 S. Hao and H. Wang, *Nat. Energy*, 2025, **10**, 164–165.

494 J. Biemolt, J. Singh, G. Prats Vergel, H. M. Pelzer and T. Burdyny, *ACS Energy Lett.*, 2025, **10**, 807–814.

495 Y. N. Guan, Y. Z. Li, Z. J. Li, Y. Hou, L. C. Lei and B. Yang, *Adv. Mater.*, 2025, 2417567.

496 L. Yuan, X. Li, G. Li, K. Peng, H. Zhang, S. Zeng, X. Sun and X. Zhang, *Adv. Sci.*, 2025, 2500368.

497 C. M. Gabardo, C. P. O'Brien, J. P. Edwards, C. McCallum, Y. Xu, C. T. Dinh, J. Li, E. H. Sargent and D. Sinton, *Joule*, 2019, **3**, 2777–2791.

498 T. Kose, C. P. O'Brien, J. Wicks, J. Abed, Y. C. Xiao, B. Sutherland, A. Sarkar, S. A. Jaffer, E. H. Sargent and D. Sinton, *Catal. Sci. Technol.*, 2022, **12**, 6239–6245.

499 J. P. Edwards, T. Alerte, C. P. O'Brien, C. M. Gabardo, S. J. Liu, J. Wicks, A. Gaona, J. Abed, Y. C. Xiao, D. Young, A. S. Rasouli, A. Sarkar, S. A. Jaffer, H. L. MacLean, E. H. Sargent and D. Sinton, *ACS Energy Lett.*, 2023, **8**, 2576–2584.

500 V. E. Nelson, C. P. O'Brien, J. P. Edwards, S. J. Liu, C. M. Gabardo, E. H. Sargent and D. Sinton, *ACS Appl. Mater. Interfaces*, 2024, **16**, 50818–50825.

501 M. Wang, B. Q. Wang, J. G. Zhang, S. B. Xi, N. Ling, Z. Y. Mi, Q. Yang, M. S. Zhang, W. R. Leow, J. Zhang and Y. Lum, *Nat. Commun.*, 2024, **15**, 1218.

502 T. Alerte, J. P. Edwards, C. M. Gabardo, C. P. O'Brien, A. Gaona, J. Wicks, A. Obradovi, A. Sarkar, S. A. Jaffer, H. L. MacLean, D. Sinton and E. H. Sargent, *ACS Energy Lett.*, 2021, **6**, 4405–4412.

503 T. Alerte, A. Gaona, J. P. Edwards, C. M. Gabardo, C. P. O'Brien, J. Wicks, L. Bonnenfant, A. S. Rasouli, D. Young, J. Abed, L. Kershaw, Y. C. Xiao, A. Sarkar, S. A. Jaffer, M. W. Schreiber, D. Sinton, H. L. MacLean and E. H. Sargent, *ACS Sustainable Chem. Eng.*, 2023, **11**, 15651–15662.

504 K. Xie, A. Ozden, R. K. Miao, Y. H. Li, D. Sinton and E. H. Sargent, *Nat. Commun.*, 2022, **13**, 3070.

505 M. G. Kibria, J. P. Edwards, C. M. Gabardo, C. T. Dinh, A. Seifitokaldani, D. Sinton and E. H. Sargent, *Adv. Mater.*, 2019, **31**, 1807166.

7016 | *Chem. Soc. Rev.*, 2025, **54**, 6973–7016

This journal is © The Royal Society of Chemistry 2025